School of GeoSciences

Dissertation
for the degree of

MSc in Geographical Information Science

Hamish Morton

August 2018

The long-term decline in surface velocity of Greenland's land-terminating outlet glaciers – an ice-sheet-wide phenomenon?

Statement of originality and length:

I declare that this dissertation represents my own work, and that where the work of others has been used it has been duly accredited. I further declare that the length of the components of this dissertation is 5407 words for the Research Paper and 9279 words for the Technical Report.

Signature: 

Date: 07/08/2018

Acknowledgements:

I would like to thank Dr. Noel Gourmelen and Josh Williams for their expert knowledge regarding the techniques used in this report. Further thanks go to Josh Williams for sharing MATLAB scripts used to present data; all figures produced using these scripts are labelled appropriately. I would also like to thank Prof. Peter Nienow for offering his interpretation of the results that have been collected.

Special thanks also go to Dr. Andrew Tedstone and Dr. Amaury Dehecq for authoring a number of Python scripts used to carry out pre- and post-processing of data. Additionally, thanks to Prof. Aslak Grinsted and Dr. Alexandra Messerli for providing opensource feature tracking software.

I also wish to acknowledge the University of Edinburgh Compute and Data Facility for providing me with access to cluster computing facilities and the USGS and ESA for supplying Landsat imagery.

Finally, I would like to thank Dr. Brice Noël *et al* and Dr. Xavier Fettweis *et al* for their work surrounding the RACMO2.3p2 and MAR regional climate models, respectively.

Research paper

Abstract:

The Greenland Ice Sheet has the potential to contribute ~7 m to global mean sea level (Morlighem et al., 2017). Ice sheet velocities influence rates of ice transport to the ablation zone and therefore impact rates of mass loss and contribution to sea level rise (Zwally et al., 2002). A recent study found that a land-terminating region of the Greenland Ice Sheet experienced a ~12% reduction in velocity between 1985 and 2014 (Tedstone et al., 2015). This was attributed to increasing antecedent runoff production leading to the development of efficient drainage systems, progressively reducing basal water pressure and therefore sliding (Tedstone et al., 2015). Until now, only velocities of a land-terminating region in the southwest have been examined. Furthermore, it has recently been argued that less deceleration has occurred than initially observed (Joughin et al., 2018a). In this paper, the entire Landsat archive from 1985 to 2016 is exploited using feature tracking techniques, to examine velocities of a land-terminating region located on Greenland's central west coast. Prior to and following the feature tracking process, data are manipulated using several different techniques to enhance outputs of final velocity maps, allowing a complete time series to be constructed. A feat that would not otherwise be possible. It is found that although deceleration is less than that observed in the southwest, antecedent runoff production still explains up to 59% of change. In replicating the findings of past studies, it is concluded that measured deceleration is not a product of sampling issues.

1.0 Introduction:

1.1 Motivation:

It is estimated that the Greenland Ice Sheet (GrIS) stores a volume of water sufficient to contribute 7.42 ± 0.05 m to global mean sea level (Morlighem et al., 2017), increasing coastal regions' vulnerability to flooding.

Velocities recorded on the GrIS affect the rate at which it contributes to sea level rise (SLR). High velocities cause accelerated transport of ice to the ablation zone, where mass loss occurs at a higher rate (Zwally et al., 2002). Furthermore, high velocities enhance dynamic thinning, whereby marginal thinning causes steep surface slopes to develop, increasing shear stress and ice velocity until sufficient thinning occurs to reduce this (Parizek and Alley, 2004; Pritchard et al., 2009). This causes affected regions to reside at lower, warmer altitudes.

Hydrological conditions at the ice-bed interface control velocities at land-terminating sectors of the GrIS (e.g. Zwally et al., 2002; Schoof, 2010; Sundal et al., 2011), as opposed to ocean temperatures and fjord topography at marine-terminating sectors (e.g. Howat et al., 2010; Straneo and Heimbach, 2013). As the GrIS retreats inland, the dynamics of land-terminating sectors will govern the rate at which SLR occurs, as the majority of the ice sheet is grounded above sea level (Joughin et al., 2010; Goelzer et al., 2013; Morlighem et al., 2017). Therefore, this study will record velocities of a land-terminating sector on the ice

sheet's central west coast (figure 1) from 1985 to 2016, to better understand how the GrIS may respond to future climatic warming.

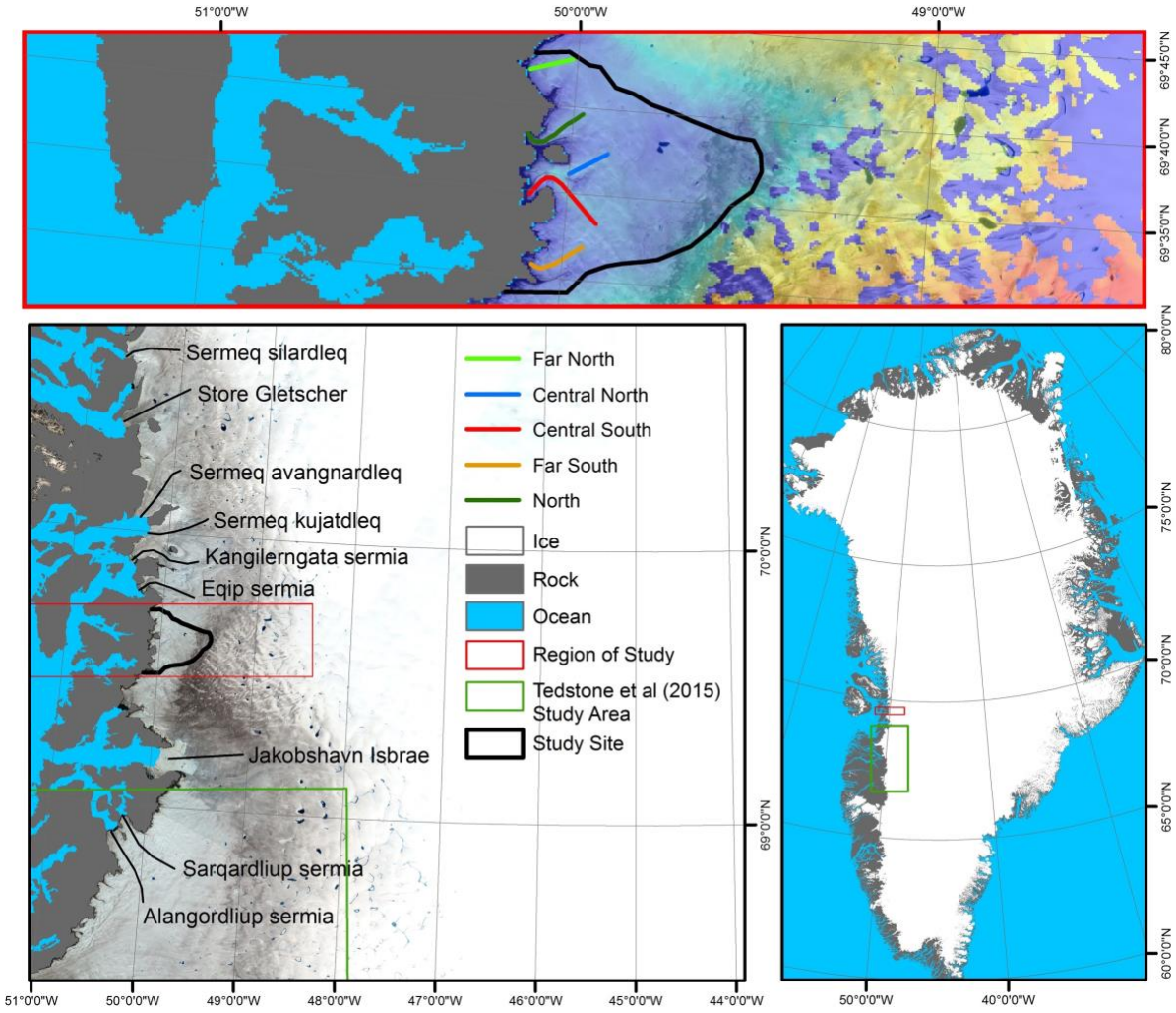

Figure 1: Top – Study region location, overlain by the study site outline, a velocity map (2015-2016) and the locations of transects present in figure 6. Bottom right – location of study region and that of Tedstone et al (2015). Bottom left – detailed view of study region with names of nearby marine-terminating glaciers, overlain on Landsat image mosaic.

1.2 Ice dynamics of land-terminating sectors:

1.2.1 Short-term trends:

It is widely accepted that surface runoff can reach the base of the GrIS (Das et al., 2008). Theoretically, once crevasses become filled with water, they propagate to the ice-bed interface as a result of tensile stress exerted upon them (Das et al., 2008; van der Veen, 2007; Alley et al., 2005). An increase in local velocity and uplift coincident with supraglacial lake drainage events supports this theory as it suggests that meltwater causes decoupling at the ice-bed interface (Das et al., 2008). Furthermore, at glacial margins meltwater is expelled subglacially (Zwally et al., 2002).

Short-term effects of runoff input to the ice-bed interface have been studied extensively (e.g. Zwally et al., 2002; Sundal et al., 2011). Measurements from Swiss Camp between 1996 and 1999 observed high summer velocities coincident with intense runoff production, suggesting that meltwater input reduces friction at the ice-bed interface, facilitating sliding (Zwally et al., 2002).

The theory that increasing meltwater inputs produce higher velocities was used in a thermomechanical flowline model (Parizek and Alley, 2004). This predicted that SLR contribution from the GrIS under a doubling of atmospheric CO_2 could reach 1080 mm by 2500 (Parizek and Alley, 2004), rather than the previously predicted 400 mm (Huybrechts and de Wolde, 1999).

More recently it has been observed that maximum velocities are highest in warmer years, but average annual velocities do not follow this trend as deceleration is observed in the fall and winter (Sundal et al., 2011; van de Wal et al., 2015). In 2012, runoff production was 113% higher than in 2009 (Tedstone et al., 2013; Sole et al., 2013). However, average annual velocity recorded at the Leverett glacier was 6% slower (Tedstone et al., 2013).

Slower average velocities observed in warmer years are likely caused by the evolution of subglacial drainage systems (Schoof, 2010; Sundal et al., 2011). At the melt season onset, drainage systems take the form of poorly-connected cavities formed leeward of topographic protrusions where ice has been forced upward (Schoof, 2005, 2010; Walder, 1986; Kamb, 1987). This means meltwater cannot be efficiently evacuated, reducing basal friction and facilitating sliding (Schoof, 2010; Sundal et al., 2011). However, once discharge exceeds a critical threshold, meltwater is evacuated through fewer laterally-connected cavities which grow into a single channel as a result of wall melting (Schoof, 2010). This is known as a Röthlisberger (R) channel, which forms part of a well-connected and efficient, arterial drainage system (Schoof, 2010; Röthlisberger, 1972). These channels facilitate drainage, causing greater basal friction and deceleration (Schoof, 2010). Therefore, in years exhibiting more melt, velocities will slow down earlier for longer durations (Sundal et al., 2011).

1.2.2 Long-term trends:

Tedstone et al (2015) measured 12% deceleration of a land-terminating region (figure 1) in the southwest of Greenland between 1985 and 2014. Deceleration occurred at a rate of -1.5 m yr^{-1} from 2002, coinciding with a period of high runoff production (Tedstone et al., 2015). However, annual velocities showed no significant relationship with annual runoff production (Tedstone et al., 2015).

Antecedent runoff produced three years prior to the velocity observation year could, however, explain 50% of ice motion (Tedstone et al., 2015). This suggests that a year-on-year increase in drainage efficiency caused by greater runoff production, progressively drains water stored in unchannelised regions, as R-channels remain open for longer (Tedstone et al., 2015). It is thought that, in ensuing years, basal sliding becomes limited as water pressures fail to recover, leading to reduced mass loss (Tedstone et al., 2015).

It has recently been argued that deceleration in the southwest is less acute than first thought (Joughin et al., 2018a). It is believed that because the Tedstone et al (2015) study ends soon after the record melt year of 2012, that measured deceleration is higher than it would be if measurements continued to 2017, as lower runoff production in recent years should cause acceleration (Joughin et al., 2018a). Furthermore, it has been argued that Tedstone et al's (2015) measurements are disproportionately influenced by summer velocities (Joughin et al., 2018b).

1.3 Deriving velocities:

Recently developed feature tracking techniques have enabled the measurement of glacial surface velocities from as early as 1985 (Dehecq et al., 2015; Tedstone et al., 2015). In exploiting the entire Landsat archive and carrying out enhancement procedures prior to and following velocity derivation, these techniques allow complete time series to be constructed using images previously deemed to be of insufficient quality. Therefore, it is now possible to generate time series extending over 30 years for most glaciated areas within Landsat orbit constraints (i.e. within 81° N/S – NASA, 2018).

1.4 Aims and hypotheses:

This report will attempt to use the aforementioned techniques to examine whether a land-terminating region located north of the Tedstone et al (2015) sector exhibits similar behaviour (figure 1). Results will help ratify past findings and aid development of cryospheric remote sensing techniques. The aims of this study are as follows:

1) Derive a velocity map archive from 1985 to 2016 and compare with antecedent runoff production
2) Examine whether trends match the observations of Tedstone et al (2015)
3) Use results to evaluate and inform development of velocity derivation techniques

Because the study site is located just ~60 km north of the Tedstone et al (2015) study site (figure 1), it is unlikely that a latitudinal climatic gradient will be strong enough to influence ice dynamics differently. It has, however, been hypothesised that land-terminating regions neighbouring marine terminating glaciers are influenced by lateral stress transfer (Tedstone et al., 2015). Therefore, the study site may not be influenced by antecedent runoff production or follow a pattern of deceleration.

2.0 Methodology:

2.1 Study site:

The study site is located on Greenland's central west coast at ~69.5°N (figure 1). It extends to ~1000 m.a.s.l and ~20 km inland, with latitudinal boundaries ~30 km apart. The Jakobshavn Isbrae and Eqip sermia marine-terminating glaciers are found immediately to the south and north, respectively.

2.2 Feature tracking:

To derive annual velocity maps, feature tracking is carried out on all tier 1 images extracted from the Landsat archive from 1985 to 2016 (Dehecq et al., 2015). Feature tracking is the process whereby surface pattern displacement is measured between a reference and a search image (Grinsted, 2015). Here, orientation correlation is used, whereby normalised intensity gradients are generated and treated as features to be tracked (Fitch et al., 2002). The multiplicative nature of this technique allows feature tracking to be carried out on Landsat 7 Scan Line Corrector (SLC) off images, as the scan lines present in these images (figure 2) produce zeroed intensity gradients (Fitch et al., 2002; Heid and Kääb, 2012).

Landsat scenes are used because they provide the longest contiguous archive of sufficient scene quality (Dehecq et al., 2015). Furthermore, they have a 16 day repeat cycle (USGS, 2018a), increasing the chances of finding cloud-free imagery.

2.3 Pre-processing:

Images used for feature tracking are subject to procedures designed to enhance feature detectability. Firstly, principle components analysis (PCA) is carried out whereby spectral bands are combined to maximise variance and feature discrimination (Dehecq et al., 2015; Lever et al., 2017). Next, following a Fourier transform, a high-pass Gaussian filter (HPGF) is applied to enhance the appearance of trackable features such as crevasses (e.g. Fahnestock et al., 2016). These techniques reduce saturation caused by insufficient radiometric resolutions and also reduce thin cloud visibility (Ahn and Howat, 2011).

2.4 Post-processing:

Following feature tracking, median coregistration is undertaken, whereby median values of directional velocity components are derived in stable areas. These values are subtracted from the entire corresponding directional component to reduce artificial result production caused by coregistration inaccuracy.

Next, temporally coincident velocity maps are merged using a median based approach. This aims to ensure that velocity maps fairly represent average annual velocities. Furthermore, in combination with pre-processing techniques, merging helps provide sufficient velocity map coverage for time series generation. A feat that would otherwise be unachievable. Median values of each merged velocity map are then used to generate a time series.

To quantify uncertainty, information on the number of points used to derive median cell velocities in stable areas is exploited (Dehecq et al., 2015). The relationship presented here is then extrapolated to on-ice areas.

2.5 Runoff models:

Regressions are carried out between antecedent runoff production and annual velocities to examine the relationship between the two variables. Runoff data is acquired from regional climate models (RCMs), because they can resolve atmospheric and physical surface

conditions at a fine spatiotemporal resolution (Noël et al., 2018; Fettweis et al., 2013). This is important, as the study site comprises of complex topography.

The RCMs used here are: the Modèle Atmosphérique Régional 3.5.2 (MAR), which provides runoff data at 10 km resolution (Fettweis et al., 2013, 2017) and a statistically downscaled version of the Regional Atmospheric Climate Model-2 (RACMO2.3p2), which provides runoff data at 1 km resolution (Noël et al., 2018).

3.0 Results:

3.1 High-pass Gaussian filter application issues:

Prior to processing all available image pairs, feature tracking parameters were experimented with to find those that produce optimum results. During this stage, it was discovered that applying a HPGF to Landsat 7 SLC-off images reduces the spatial extent of velocity observations where scan lines are located, therefore no HPGF was applied to these images (figure 2). This, as of yet, is undocumented in feature tracking literature.

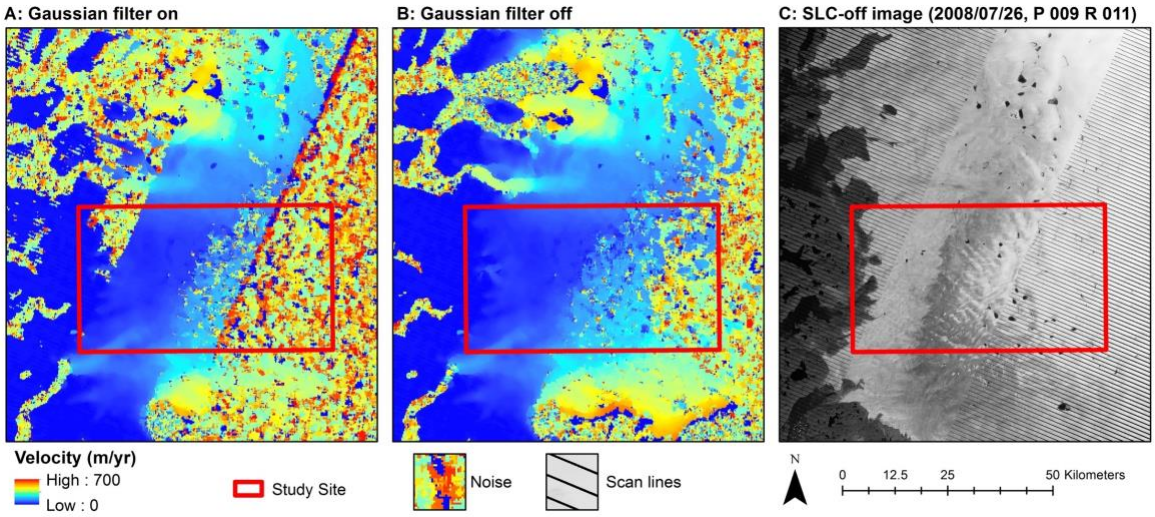

Figure 2: Illustration showing how the use of a high-pass Gaussian filter reduces the extent of coherent velocity map coverage when feature tracking is carried out on SLC-off images. A – HPGF-on leading to poor performance, B – HPGF-off leading to improved performance, C – example of SLC-off image.

3.2 Data availability:

The number of years over which temporally coincident velocity maps are merged to provide average velocities is dependent upon data quality. For Landsat 5 derived scenes (1985-1998), merges occur over periods of two to three years (figure 4). In years where Landsats 7 and 8 data are available (1999-present), merges occur over one- to two-year intervals.

Overall, 3236 common points are found between all scenes (figure 4), all below 1000 m.a.s.l (figure 3).

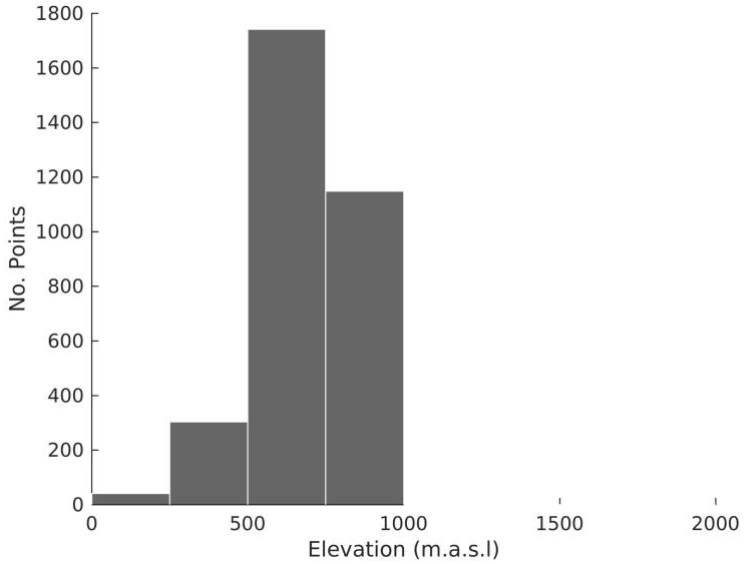

Figure 3: The number of common points observed at different altitudinal intervals between all merges used in the time series (figure 4), excluding points exhibiting error greater than 60 m yr^{-1}. Script for figure production supplied by Josh Williams.

3.3 Overall trends:

3.3.1 Final time series:

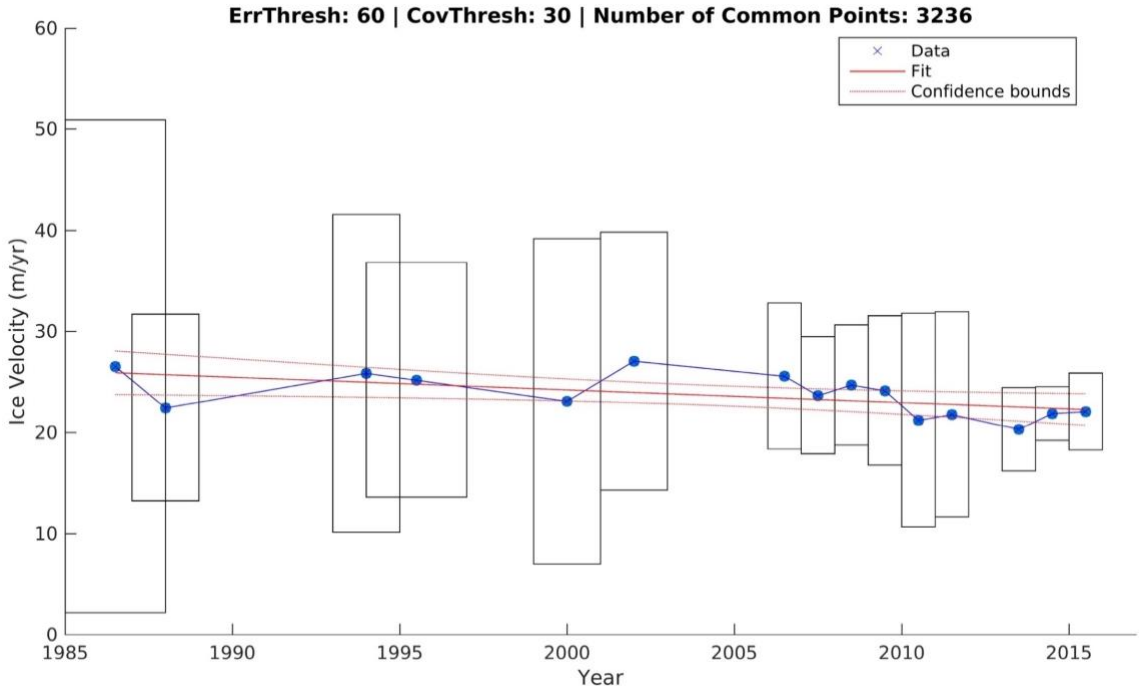

Figure 4: Final time series of median average annual velocities, derived from velocity maps merged over differing temporal periods. Pixels are only used to compute the median if they are spatially coincident across all scenes, have an error threshold of less than 60 m yr^{-1} and are from merges with greater than 30% study area spatial coverage. The rectangles surrounding each observation represent error in the Y direction and temporal coverage in the X direction. Script for figure production supplied by Josh Williams.

To maintain consistency with the processing techniques of Tedstone et al (2015), only pixels exhibiting error of less than 60 m yr^{-1} are used to calculate median annual velocities in the final time series.

From 1985 to 2016, a trend of -0.13 m yr^{-1} is present (R^2 = 0.33, $p < 0.05$) (figure 4). Throughout the final time series there several periods exhibiting no observations.

3.3.2 Erroneous time series:

Prior to derivation of the final time series (figure 4 – used throughout the rest of this study), it was discovered that using spectral bands of inconsistent spatial resolution causes systematically different feature tracking result characteristics (figure 5). When comparing figures 4 and 5 it appears that post-2000 velocities (produced using panchromatic bands of 15 m resolution) have increased relative to pre-2000 velocities (produced using bands two and three of 30 m resolution). For this reason, bands two and three were used to derive the entire final time series (see technical report – section 3.1).

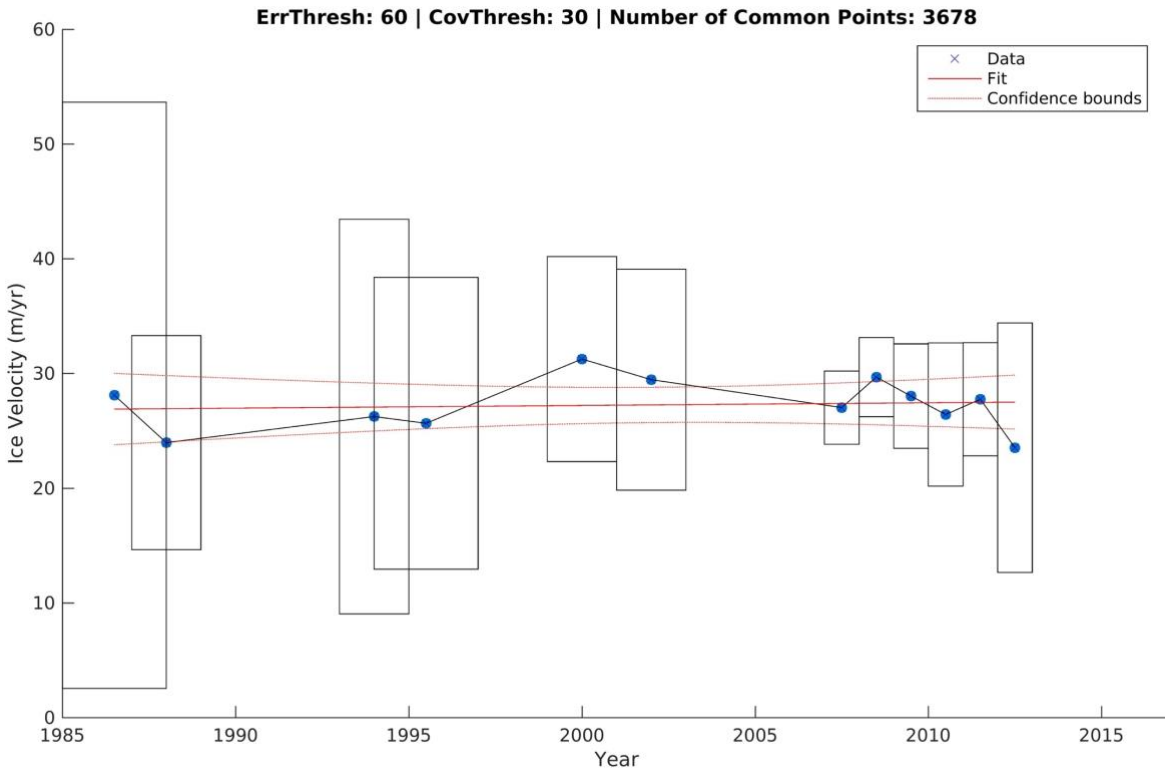

Figure 5: Time series created using feature tracking on bands two and three (30 m resolution) pre-1999 and panchromatic bands (15 m resolution) post-1999. Landsat 8 data is excluded. Error and study site coverage thresholds are 60 m yr^{-1} and 30%, respectively. The rectangles surrounding each observation represent error in the Y direction and temporal coverage in the X direction. Script for figure production supplied by Josh Williams.

3.3.3 Mann-Whitney-Wilcoxon tests:

Mann-Whitney-Wilcoxon (MWW) tests are carried out to understand whether final velocity time series data can be split into temporally distinct periods (LaMorte, 2017). The point at which population samples become statistically distinct is used as an indicator of deceleration onset. In agreement with the findings of Tedstone et al (2015), statistically significant difference is first observed in 2002 ($W = 45$, $p < 0.05$).

3.3.4 Segmented linear regressions:

MWW test results provide motivation to carry out segmented linear regressions, to aid understanding of sample characteristics either side of the predicted deceleration onset date. Segmented linear regressions are carried out using break dates between 1998 and 2009, with a further break applied in 2013 to account for minor acceleration witnessed beyond this point. A break date of 2006 provides the lowest residual standard error (RSE) of 1.40 m yr^{-1} ($R^2 = 0.64$, $p < 0.01$). Using this information in combination with MWW test outputs, it is predicted that deceleration is initiated between 2002 and 2006. Thus, an optimum break date of 2004 is selected.

Prior to 2004, no trend is observed (0.10 m yr^{-1}, $p = 0.29$). Following 2004, however, a decreasing trend of -0.69 m yr^{-1} is measured until 2013 ($p < 0.05$). Finally, no trend (0.83 m yr^{-1}, $p = 0.23$) is observed beyond 2013.

3.4 Transects:

Transects were taken to assess the distribution of velocity change patterns across the study site (figures 1 and 6). All margins from which transects extend are land terminating. The ‘Central north’ and ‘Far south’ transects observe deceleration across the study period (figure 6).

For transects ‘Central south’, ‘Far north’ and ‘North’ the pattern of deceleration is not clear. This is particularly the case at transect origins. For the ‘Far north’ transect, deceleration is witnessed beyond ~1000 m from the origin.

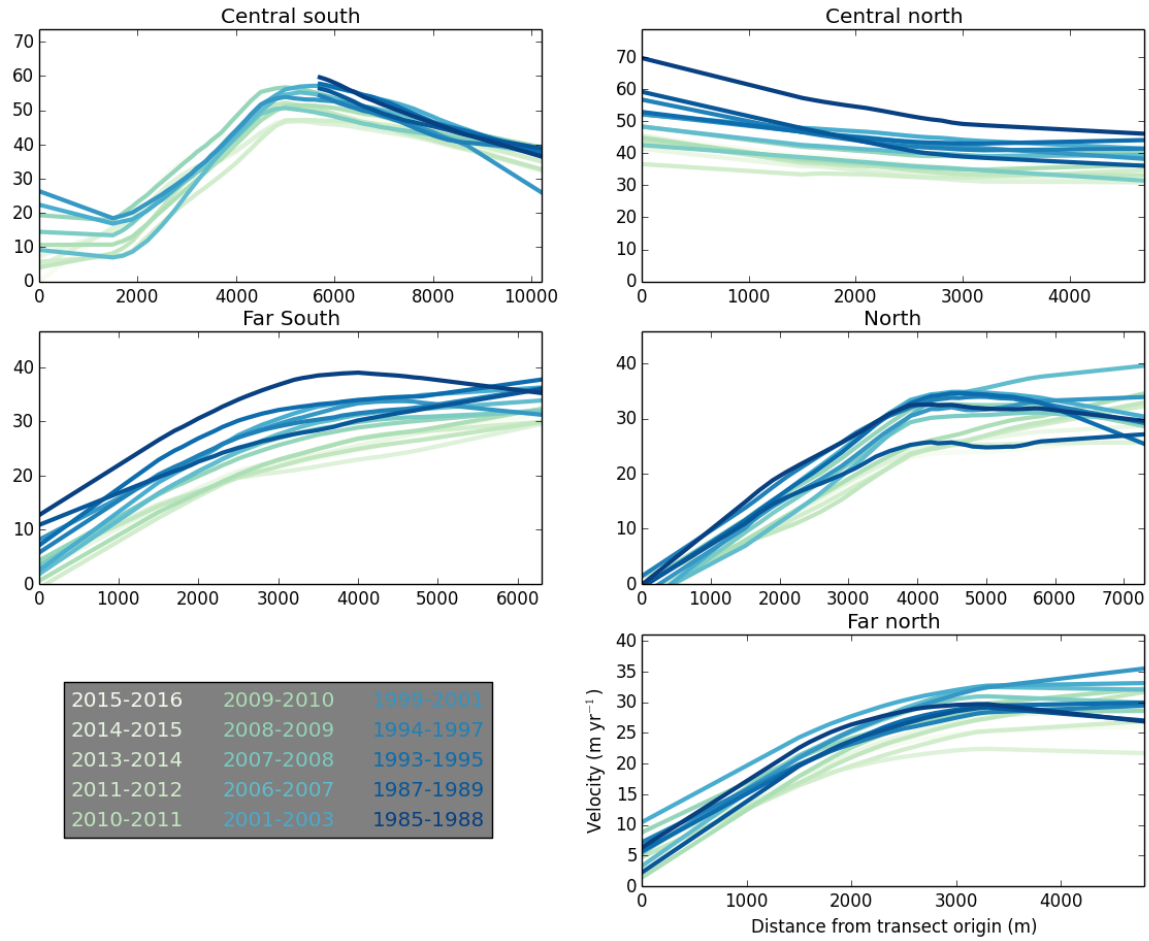

Figure 6: Velocity profiles corresponding to transect locations shown in figure 1. Missing values are not interpolated. Points exhibiting error greater than 60 m yr^{-1} are included, as they are filtered out using a Savitzky-Golay filter (SciPy Cookbook, 2012).

3.5 Baseline velocity comparison:

To further understand velocity change patterns, a comparison is performed whereby annual velocity maps are compared to a baseline derived using all available image pairs.

Prior to 2007-2008 the majority of the study region exhibits a velocity greater than that of the baseline (figure 7). Two exceptions are 1987-1989 and 1999-2001, where recorded velocities lower than the baseline are likely a result of noise.

In 2006-2007 it appears that deceleration is initiated at the ice sheet margin, whereas inland velocities flow above baseline values. In 2007-2008 no pattern of deceleration is observed. However, from 2008-2009 to 2013-2014 it appears that deceleration, by comparison to baseline velocity, extends inland. Finally, an increase in velocity is observed relative to the baseline from 2014-2015 onward.

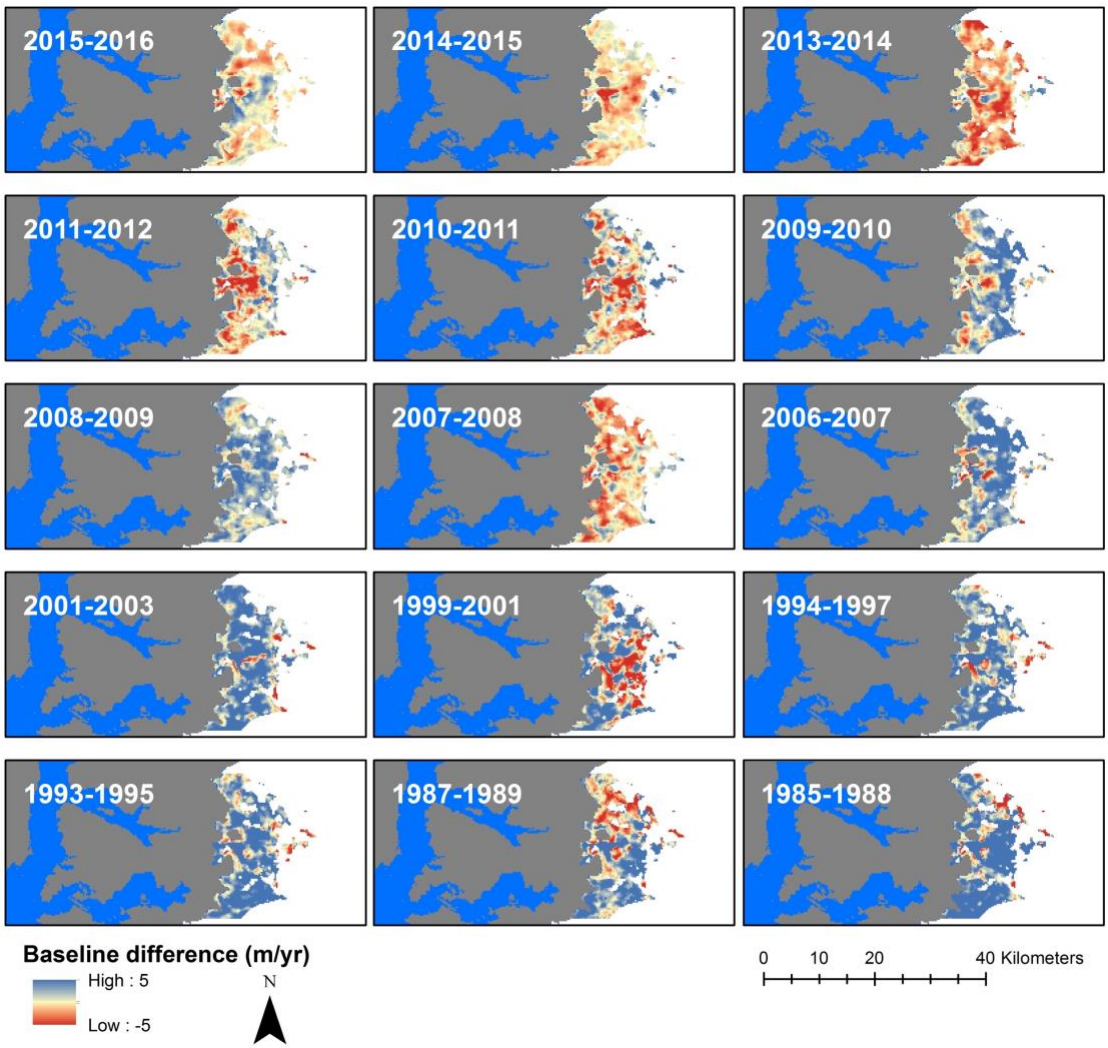

Figure 7: Differences between baseline velocity map (1985-2016) and individual merges. Negative values are below the baseline and positive values are above. Only spatially coincident points are shown. Points with error greater than 60 m yr^{-1} are not excluded.

3.6 Runoff trends:

3.6.1 MAR:

MAR mean annual runoff production (figure 8) increases at a rate of 36.14 w.e. mm yr^{-1} from 1985 to 2014 ($R^2 = 0.32$, $p < 0.01$).

Upon visual inspection it appears that runoff data can be divided into periods of low, increasing and then decreasing production. To test this theory, a series of segmented linear regressions are undertaken, examining all possible break date combinations.

Break dates of 1992 and 2012 provide the lowest RSE of 435.8 w.e. mm yr^{-1} ($R^2 = 0.47$, $p < 0.001$). There is no trend prior to 1992 ($p = 0.14$). However, from 1992 to 2012 an increasing trend of 141.56 w.e. mm yr^{-1} ($p < 0.05$) is observed. Beyond 2012, a decreasing trend of -401.46 w.e. mm yr^{-1} ($p < 0.1$) is observed.

As a further line of investigation, MWW tests are carried out between population samples covered by each regression line. Statistically significant difference is found between samples derived from 1985 to 1992 and 1993 to 2012 ($W = 38$, $p < 0.05$). No significant difference, however, is present when these sample periods are compared to a population sample of 2013 to 2014, owing to the size of the most recent sample (Forero, 2013).

Using these results, it is predicted that MAR simulated runoff production starts to increase circa 1992, and then decrease circa 2012.

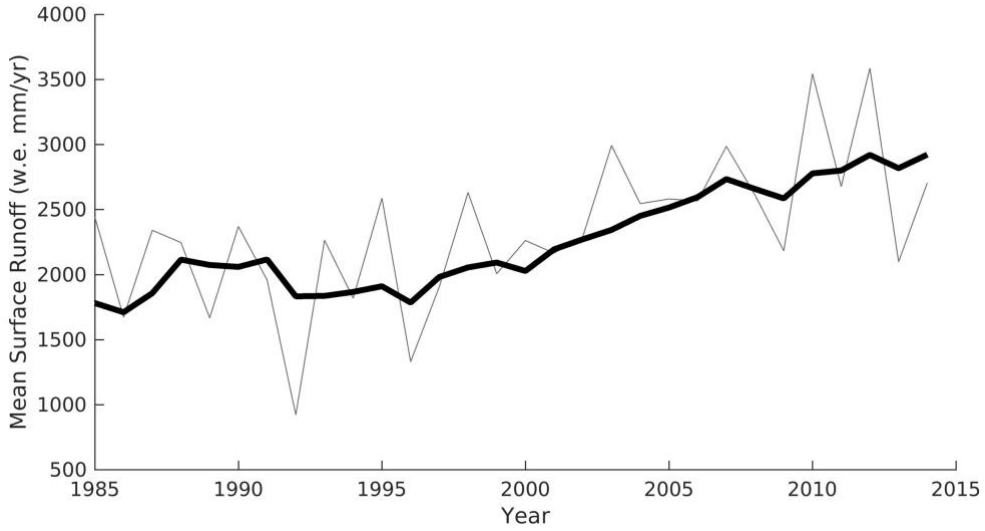

Figure 8: Mean annual runoff simulations provided by MAR for 'Ice Sheet Mass Balance Inter-comparison Exercise' (IMBIE) basins 7.1 and 7.2, below 1000 m.a.s.l (Zwally et al., 2012; IMBIE, 2016). Simulations cover the period 1985 to 2014, overlain by a five-year moving average. Script for figure production supplied by Josh Williams.

3.6.2 RACMO2.3p2:

RACMO2.3p2 mean annual runoff production (figure 9) increases at a rate of 20.88 w.e. mm yr^{-1} from 1985 to 2016 ($R^2 = 0.19$, $p < 0.05$).

Segmented linear regressions are also applied to RACMO2.3p2 data, testing all break date combinations. The lowest RSE (385.6 w.e. mm yr^{-1}) is achieved with break dates in 1996 and 2011 ($R^2 = 0.32$, $p < 0.05$). Prior to 1996, no trend is observed ($p = 0.36$). However, from 1996 to 2011 runoff production increases at a rate of 79.75 w.e. mm yr^{-1} ($p < 0.05$). From 2011 to 2016, a decreasing trend of -146.74 w.e. mm yr^{-1} ($p < 0.1$) is observed.

When applying MWW tests to population samples provided by the segmented linear regression with the lowest RSE, statistically insignificant results are returned. Statistically significant difference is, however, found between population samples from 1985 to 1997 and 1998 to 2012 ($W = 53$, $p < 0.05$). No statistically significant difference is found between population samples when compared with the most recent sample, owing to its size (Forero, 2013).

Based on statistical test results, it is predicted that RACMO2.3p2 simulated runoff begins to increase circa 1996, before decreasing beyond 2011.

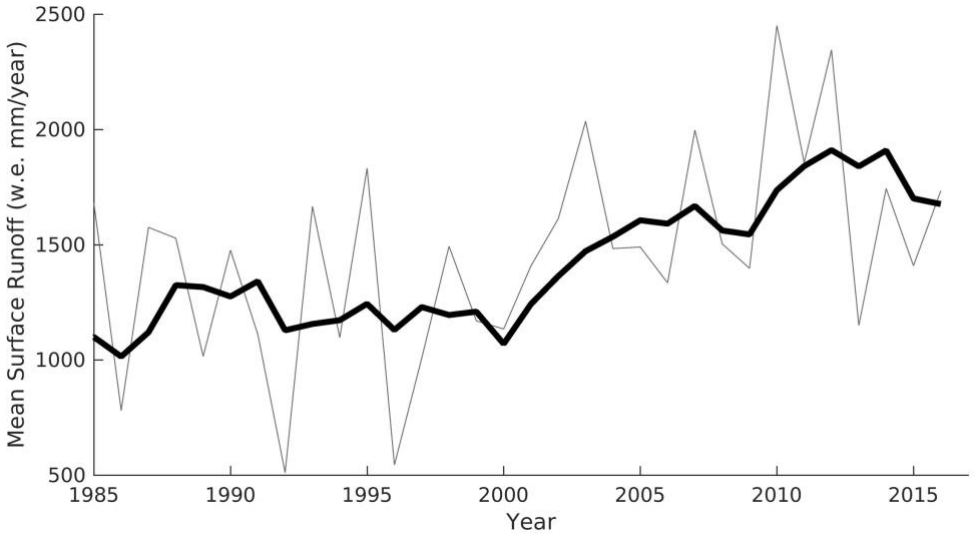

Figure 9: Mean annual runoff simulations provided by RACMO2.3p2 for IMBIE basins 7.1 and 7.2, below 1000 m.a.s.l (Zwally et al., 2012; IMBIE, 2016). Simulations cover the period 1985 to 2016, overlain by a five-year moving average. Script for figure production supplied by Josh Williams.

3.7 Antecedent runoff regressions:

Regressions were carried out between median annual velocities and antecedent runoff production extending five years prior to annual velocity observations, both including and excluding the velocity observation year.

No significant relationship is present on an annual timescale. RACMO2.3p2 and MAR data only explain 13% ($p = 0.18$) and 19% ($p = 0.12$) of velocity change to a statistically insignificant level, respectively.

For both RCMs, antecedent runoff produced three years prior to and including the year of velocity observation best explains velocity change. RACMO2.3p2 can explain up to 59% of change ($p < 0.001$). Up to 48% of change is explained by MAR ($p < 0.01$).

3.8 Effects of changing ice sheet geometry:

To understand whether changing ice sheet geometries are likely to have caused deceleration through alteration of basal shear stress and therefore deformation (Davies, 2017; Paterson, 1994), a series of analysis of covariance (ANCOVA) tests have been undertaken.

3.8.1 Surface slope:

Upon inspection of surface slopes corresponding to 1985 (aeroDEM – Korsgaard et al et., 2016) and 2007 (GIMP DEM – Howat et al., 2014), gradients appear similar (figure 10). When carrying out an ANCOVA test, no statistically significant difference between regression line gradients is found ($F = 2.097$, $p = 0.15$).

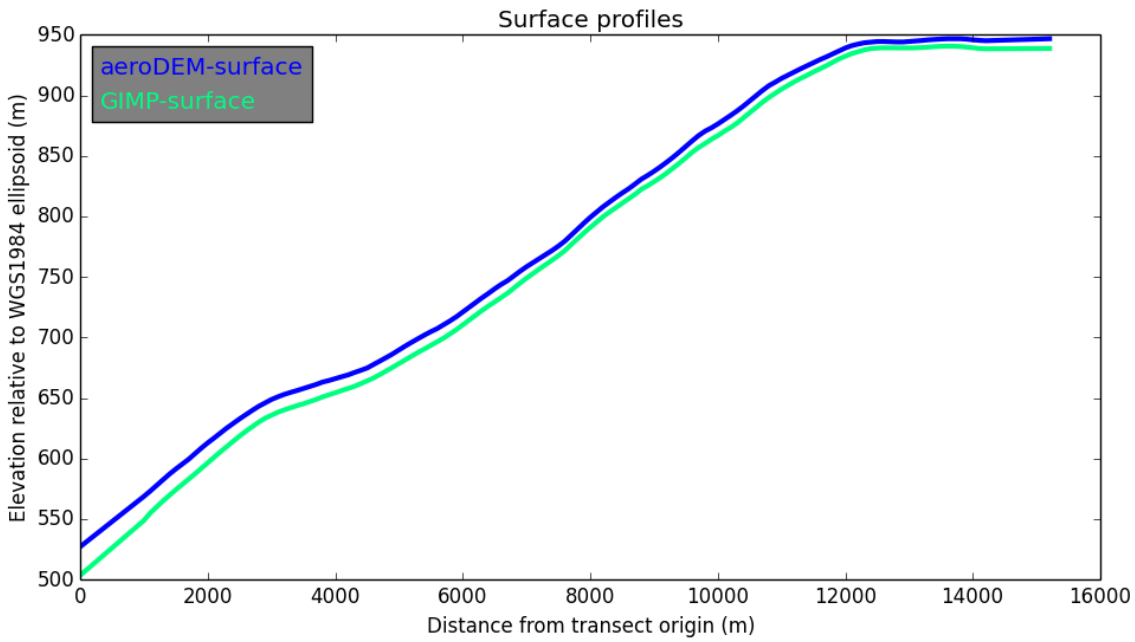

Figure 10: Surface elevation profiles of the GIMP DEM (2007) and aeroDEM (1985) taken along an extended version of the 'Far south' transect shown in figure 1 (also see technical report – section 2.11.2). Both are measured in metres relative to the WGS1984 ellipsoid.

3.8.2 Thickness:

When comparing ice thickness profiles, it appears that ~25 m difference is observed near the transect origin (figure 11). However, when carrying out an ANCOVA test, no statistically significant difference is found between regression line gradients (F = 0.164, p = 0.69), or Y intercepts (F = 0.976, p = 0.32).

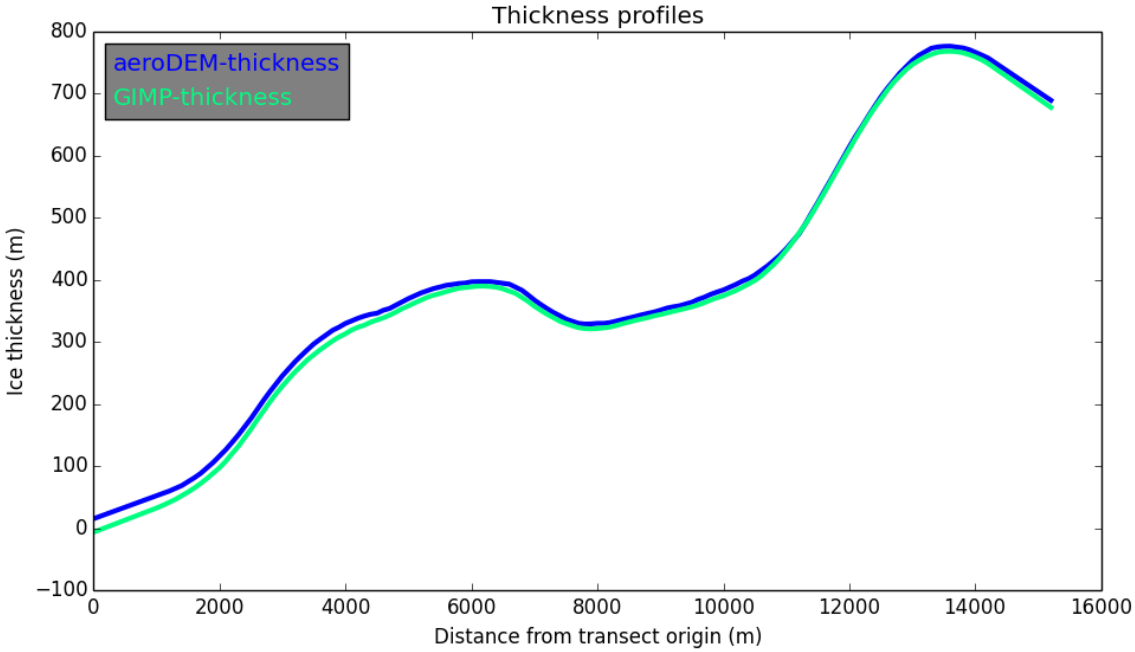

Figure 11: Ice thickness profiles of the GIMP DEM (2007) and aeroDEM (1985) taken along an extended version of the 'Far south' transect shown in figure 1 (also see technical report – section 2.11.2).

4.0 Discussion:

4.1 Effects of changing geometry:

Despite the lack of statistically significant difference between both the surface slope and ice thickness of the aeroDEM and GIMP DEM, ice thickness change of up to ~25 m is still observed, suggesting thinning has occurred at a rate of ~1 m yr^{-1}. Tedstone et al (2015) find that such thinning cannot be ruled out as a cause of velocity change in their study area. Therefore, results presented here should be addressed with caution as further work is required to determine the effects of changing driving stresses.

4.2 Uncertainty relative to past studies:

In this study, error measurements for individual velocity observations are consistent in magnitude with those obtained by Tedstone et al (2015). This suggests that techniques used here have been successful, as they could be used to resolve changes observed in Tedstone et al's (2015) study region. Error observed here does, however, mean that results should be viewed with caution as error bars show large amounts of overlap with each other.

4.3 Observed trends:

4.3.1 Annual trends:

Results presented here support past studies which observe that on annual timescales, runoff production shows no statistically significant relationship with velocity. For example, Sole et al (2013) recorded a series of velocity observations on the Leverett glacier. They observed significant correlation between summer runoff production and summer velocity ($r = 0.79$, $p < 0.05$) and late summer runoff production and winter velocity ($r = -0.55$, $p < 0.05$), leading to no significant annual correlation (Sole et al., 2013). These findings are corroborated by van de Wal et al (2015) who recorded sub-annual variations in basal water pressure on the K-Transect. They found that following a 'spring event' of high basal water pressure coinciding with high velocities, water pressure drops suggesting that the basal drainage system has become efficient (van de Wal et al., 2015). Following this, water pressure starts to recover. However, with an efficient drainage system and a gradual reduction in the amount of runoff produced throughout the year, velocities slow to below the baseline average in the winter due to enhanced basal friction (van de Wal et al., 2015).

4.3.2 Cause of deceleration:

Although deceleration witnessed in this study is less than that observed by Tedstone et al (2015), the suggested cause is the same. This is initially suggested by the fact that deceleration initiation is observed between 2002 and 2006, coinciding with an increase in runoff production not long prior to this. Additionally, up to 59% of velocity variation is explained by antecedent runoff produced three years prior to, and including, the year of velocity observation.

The relationship between velocity and antecedent runoff production supports the hypothesis that increasing runoff input to the ice-bed interface causes the basal drainage system to become efficient (Schoof, 2010; Sundal et al., 2011; Tedstone et al., 2013). The drainage system can then evacuate water stored at the base of the ice sheet for a longer period of time each year (Sole et al., 2013; Tedstone et al., 2013). This is likely to cause progressive year-on-year dewatering of unchannelised regions, leading to greater basal friction and deceleration on decadal timescales (Tedstone et al., 2015).

The fact that runoff production simulated by both RCMs explains high amounts of velocity change, increases the confidence in findings.

4.3.3 Low magnitude of deceleration:

Overall, Tedstone et al (2015) observe average deceleration of 12% between 1985-1994 and 2007-2014, at a rate of -1.5 m yr^{-1} after 2002. Contrastingly, a more modest 5.1% deceleration is observed here between 1985-1997 and 2006-2016, at a rate of -0.69 m yr^{-1} from 2004 to 2013. A period of statistically insignificant behaviour beyond 2013 is then observed and interpreted as the initiation of acceleration.

The overall level of deceleration may be partially limited by acceleration initiation in 2013. Both RCMs simulate a rapid drop in runoff production from circa 2011 onward. This could cause the basal drainage system to revert to an inefficient state, leading to a year-on-year reduction in dewatering and a recovery of basal water pressures and ice sheet velocities, consistent with the theory that larger volumes of antecedent runoff input to the ice-bed interface cause deceleration in subsequent years (Tedstone et al., 2015).

The lower rate of deceleration observed in this study from 2004 to 2013 shows that the overall reduction in velocity would remain minor, regardless of acceleration initiation circa 2013. This could be attributed to the theory that velocity in this sector of the ice sheet is not heavily influenced by changes in the efficiency of the basal drainage system. Perhaps due to differing basal substrates and therefore roughness characteristics by comparison to the study site of Tedstone et al (2015) (Paterson, 1994). Furthermore, the extent of deceleration witnessed here may be partially hampered by the overall increase in runoff production of ~41% from 1985-1994 to 2007-2014, as Tedstone et al (2015) observe a larger increase of 49.8% over the same period.

4.3.4 Spatial pattern of deceleration:

Deceleration observed near the ice sheet margin likely occurs prior to that observed inland as a result of an earlier switch to an efficient drainage system (Sole et al., 2013), causing progressive year-on-year dewatering at the ice-bed interface to occur sooner. Adiabatic lapse rates explain this, as they suggest that lower elevations would be subject to greater levels of warming and therefore runoff production. Greater deceleration (~15-20%) witnessed at lower elevations (<800 m.a.s.l) by Tedstone et al (2015) supports this hypothesis, as it suggests deceleration has been occurring for a longer period of time.

The slow velocities recorded relative to the baseline in 2007-2008 could be the result of a surge in runoff production in 2007 (figures 8 and 9), causing drainage systems to become more efficient, temporarily reducing basal water pressure in the subsequent year (Tedstone et al., 2015).

Transects do not extend far enough inland to provide information regarding deceleration onset information, as flowlines could not be reliably delineated to this extent. Information regarding latitudinal variation of deceleration is, however, provided. The inconsistent pattern of deceleration between transects is indicative of variations in basal drainage system connectivity. Andrews et al (2014) suggest that velocities of areas coupled to hydrologically isolated regions of the bed resist ice motion onset in well-connected regions due to greater basal friction. Therefore, areas that do not show clear deceleration patterns may correspond to hydrologically isolated regions of the bed. This could also help explain the minor level of deceleration witnessed, relative to Tedstone et al (2015).

4.4 Contribution to literature in wider context:

In agreement with Joughin et al (2018a), minor deceleration is witnessed relative to Tedstone et al (2015). This can partially be attributed to a longer study period length than Tedstone et al (2015). The observation of relatively minor deceleration does not conflict with the findings of Tedstone et al (2015), as recent acceleration is explained by changes in antecedent runoff production.

Results presented here help disprove the suggestion that the findings of Tedstone et al (2015) suffer from sample bias (Joughin et al., 2018b), as a sensitivity analysis (see technical report – section 2.4.1) finds the effects of this bias to cause velocity variation of less than 0.9 m yr^{-1}. Furthermore, the trend of deceleration presented by Tedstone et al (2015) holds in this study under different image pair temporal separation characteristics.

4.5 Methodological assessment and future developments:

Despite the use of enhancement techniques, the incomplete time series and scale of error witnessed in this study show that further progress can be made to improve feature tracking results. For archived imagery, improved processing methods offer feature tracking performance gain and time series completeness improvement opportunities. Feature tracking performance on archived imagery of poor radiometric and spatial resolutions could be enhanced by utilising more spectral bands for PCA and re-gridding data to a 15 m resolution (Fahnestock et al., 2016). Past studies have witnessed improvement proportional to the number of bands used, multiplied by image radiometric quantisation (Fahnestock et al., 2016). This is of highest importance for studies aiming to utilise imagery from radiometrically inferior sensors, which limit common points available for time series generation.

HPGF application likely reduces the spatial coverage of SLC-off derived velocity maps by altering values of zeroed intensity gradients at scan lines (e.g. Fitch et al., 2002). This will generate false trackable features that yield noise as a result of low maximum correlation coefficients (Grinsted, 2015). Landsat 7's ETM+ sensor is radiometrically inferior relative to

newer sensors (USGS, 2018b), therefore the HPGF issue also needs addressing to allow more complete time series generation.

Time series could also be made more complete if archived tier 2 imagery exhibiting poor geolocational accuracies was used for feature tracking. This imagery is common over ice sheets, due to a lack of stable ground visible for georeferencing (USGS, 2018c). To utilise these images, accurate coregistration to a master image must be achieved. Past studies have used cross-correlation of quasi-stationary ice sheet surface features for coregistration (e.g. Scambos et al., 1992; Berthier et al., 2003). However, the success of this technique is limited due to radiometric constraints of older sensors (Fahnestock et al., 2016). Therefore, this method would only perform better than median coregistration if a best-case scenario of 1-2 pixel misalignment was obtained between images of annual separation (Fahnestock et al., 2016; Berthier et al., 2003). It could, however, still be useful in areas where median coregistration is not possible, given that image pairs exhibiting poor coregistration performance are filtered out.

Alignment of areas flowing at less than 10 m yr^{-1} (delineated using synthetic aperture radar imagery) could also be used for coregistration (Fahnestock et al., 2016). This would, however, be unsuitable for images partially covered by cloud and would require temporally consistent velocity patterns to be visible, making median coregistration more suitable in this study.

Future advances in image geolocational accuracy will reduce coregistration error and could allow use of images containing less stable ground. For example, the geolocational accuracy of Landsat 8 scenes is superior to previous missions, due the use of a pushbroom sensor and improved onboard GPS system (Roy et al., 2014).

Future feature tracking studies will also benefit from increasing image acquisition rates. For example, ESA's Sentinel-2 satellites provide repeat acquisitions over five-day periods at the equator (ESA, 2017). This presents an opportunity to collect vast quantities of imagery, increasing the likelihood that data will be unaffected by cloud cover.

Finally, feature tracking studies using current and future sensors will also benefit from enhanced radiometric resolutions. For example, the Landsat 8 OLI sensor offers 12-bit quantisation, making it more suitable for deriving velocities of ice sheet interiors (USGS, 2018b). This is important as the response of GrIS velocities to runoff production in interior regions could be the opposite to that observed nearer the coast (Doyle et al., 2014; Sole et al., 2013; Joughin et al., 2018a; Nienow, 2017). Doyle et al (2014) observed that annual speed-up correlates positively with melt season intensity at 1840 m.a.s.l, ~140 km inland on the K-transect, likely because insufficient runoff production occurs to cause drainage system organisation (Pimental and Flowers, 2010; Schoof, 2010; Doyle et al., 2014). Furthermore, ice is significantly thicker than in coastal regions, meaning overburden pressure causes faster creep closure of channels (Nye, 1953; Doyle et al, 2014).

4.6 Implications of band choice discovery:

Band resolution likely causes velocity changes by altering the location where maximum similarity is observed between reference and search image feature patterns (see technical report – section 3.1). This discovery is important as it means future studies will have to utilise images of coarser resolution if they are to create a time series extending earlier than 1999. Although not a problem here, for regions containing trackable patterns of a finer scale, time series completeness could be compromised.

5.0 Conclusion:

This study successfully uses a series of enhancement techniques to enable the creation of a multidecadal velocity time series using feature tracking methods. The time series exhibits gaps and some observations show large error constraints. Therefore, several processing techniques and technological advances are suggested that may improve feature tracking results from past, present and future data products.

Perhaps the most important finding in this study, concerning velocity derivation techniques, is that the use of inconsistent band choices produces erroneous time series. This has implications for studies wishing to utilise the pre-1999 Landsat archive.

From a glaciological perspective, the findings of this study support the past observation that multidecadal deceleration of a land-terminating region has occurred and that this is likely controlled by antecedent runoff production (Tedstone et al., 2015). Significantly, deceleration was still observed on a small sector located amongst fast flowing marine-terminating glaciers. This conflicts with the theory that lateral stress transfer would eliminate this signal.

The deceleration signal observed here is weaker than that observed by Tedstone et al (2015). This could be the result of sporadic basal hydrologic isolation (Andrews et al., 2014), differing basal substrate (Paterson, 1994), or a lesser increase in runoff production relative to Tedstone et al (2015). To accurately force ice sheet models, these theories should be addressed.

By extending the study period of Tedstone et al (2015), a minor recovery of velocities is observed, consistent with Joughin et al (2018a). However, this does not contradict previous findings, as the theory explaining deceleration also explains acceleration. In the future, velocities of other land terminating sectors of the GrIS should be examined, as Joughin et al (2018a) suggest observed trends may be a result of water piracy by the Jakobshavn Isbrae glacier.

6.0 References:

Ahn, Y. and Howat, I. (2011). Efficient Automated Glacier Surface Velocity Measurement From Repeat Images Using Multi-Image/Multichip and Null Exclusion Feature Tracking. *IEEE Transactions on Geoscience and Remote Sensing*, 49(8), pp.2838-2846.

Alley, R., Dupont, T., Parizek, B. and Anandakrishnan, S. (2005). Access of surface meltwater to beds of sub-freezing glaciers: preliminary insights. *Annals of Glaciology*, 40, pp.8-14.

Andrews, L., Catania, G., Hoffman, M., Gulley, J., Lüthi, M., Ryser, C., Hawley, R. and Neumann, T. (2014). Direct observations of evolving subglacial drainage beneath the Greenland Ice Sheet. *Nature*, 514(7520), pp.80-83.

Berthier, E., Raup, B. and Scambos, T. (2003). New velocity map and mass-balance estimate of Mertz Glacier, East Antarctica, derived from Landsat sequential imagery. Journal of Glaciology, 49(167), pp.503-511.

Das, S., Joughin, I., Behn, M., Howat, I., King, M., Lizarralde, D. and Bhatia, M. (2008). Fracture Propagation to the Base of the Greenland Ice Sheet During Supraglacial Lake Drainage. *Science*, 320(5877), pp.778-781.

Davies, B. (2017). *Stress and Strain*. [online] AntarcticGlaciers.org. Available at: http://www.antarcticglaciers.org/modern-glaciers/glacier-flow-2/glacier-flow-ii-stress-and-strain/ [Accessed 5 Jul. 2018].

Dehecq, A., Gourmelen, N. and Trouve, E. (2015). Deriving large-scale glacier velocities from a complete satellite archive: Application to the Pamir–Karakoram–Himalaya. *Remote Sensing of Environment*, 162, pp.55-66.

Doyle, S., Hubbard, A., Fitzpatrick, A., van As, D., Mikkelsen, A., Pettersson, R. and Hubbard, B. (2014). Persistent flow acceleration within the interior of the Greenland ice sheet. *Geophysical Research Letters*, 41(3), pp.899-905.

ESA (2017). *Sentinel-2*. [online] Sentinel.esa.int. Available at: https://sentinel.esa.int/web/sentinel/missions/sentinel-2 [Accessed 2 Aug. 2018].

Fahnestock, M., Scambos, T., Moon, T., Gardner, A., Haran, T. and Klinger, M. (2016). Rapid large-area mapping of ice flow using Landsat 8. *Remote Sensing of Environment*, 185, pp.84-94.

Fettweis, X., Box, J., Agosta, C., Amory, C., Kittel, C., Lang, C., van As, D., Machguth, H. and Gallée, H. (2017). Reconstructions of the 1900–2015 Greenland ice sheet surface mass balance using the regional climate MAR model. *The Cryosphere*, 11(2), pp.1015-1033.

Fettweis, X., Franco, B., Tedesco, M., van Angelen, J., Lenaerts, J., van den Broeke, M. and Gallée, H. (2013). Estimating the Greenland ice sheet surface mass balance contribution to future sea level rise using the regional atmospheric climate model MAR. *The Cryosphere*, 7(2), pp.469-489.

Fitch, A., Kadyrov, A., Christmas, W. and Kittler, J. (2002). Orientation Correlation. *Proceedings of the British Machine Vision Conference 2002*.

Forero, L. (2013). *Wilcoxon-Mann-Whitney test and a small sample size | Oxford Protein Informatics Group*. [online] Blopig.com. Available at: http://www.blopig.com/blog/2013/10/wilcoxon-mann-whitney-test-and-a-small-sample-size/ [Accessed 9 May 2018].

Goelzer, H., Huybrechts, P., Fürst, J., Nick, F., Andersen, M., Edwards, T., Fettweis, X., Payne, A. and Shannon, S. (2013). Sensitivity of Greenland Ice Sheet Projections to Model Formulations. *Journal of Glaciology*, 59(216), pp.733-749.

Grinsted, A. (2015). *templatematch.m - ImGRAFT*. [online] Imgraft.glaciology.net. Available at: http://imgraft.glaciology.net/documentation/functions/templatematchm [Accessed 16 Jul. 2018].

Heid, T. and Kääb, A. (2012). Evaluation of existing image matching methods for deriving glacier surface displacements globally from optical satellite imagery. *Remote Sensing of Environment*, 118, pp.339-355.

Howat, I., Box, J., Ahn, Y., Herrington, A. and McFadden, E. (2010). Seasonal variability in the dynamics of marine-terminating outlet glaciers in Greenland. *Journal of Glaciology*, 56(198), pp.601-613.

Howat, I., Negrete, A. and Smith, B. (2014). The Greenland Ice Mapping Project (GIMP) land classification and surface elevation data sets. *The Cryosphere*, 8(4), pp.1509-1518.

Huybrechts, P. and de Wolde, J. (1999). The Dynamic Response of the Greenland and Antarctic Ice Sheets to Multiple-Century Climatic Warming. Journal of Climate, 12, pp.2169-2188.

IMBIE (2016). *Drainage Basins*. [online] Imbie.org. Available at: http://imbie.org/imbie-2016/drainage-basins/ [Accessed 9 May 2018].

Joughin, I., Smith, B. and Howat, I. (2018a). Greenland Ice Mapping Project: ice flow velocity variation at sub-monthly to decadal timescales. *The Cryosphere*, 12(7), pp.2211-2227.

Joughin, I., Smith, B. and Howat, I. (2018b). Greenland Ice Mapping Project: Ice Flow Velocity Variation at sub-monthly to decadal time scales. *The Cryosphere Discussions*, pp.1-30.

Joughin, I., Smith, B., Howat, I., Scambos, T. and Moon, T. (2010). Greenland flow variability from ice-sheet-wide velocity mapping. *Journal of Glaciology*, 56(197), pp.415-430.

Kamb, B. (1987). Glacier surge mechanism based on linked cavity configuration of the basal water conduit system. *Journal of Geophysical Research*, 92(B9), pp.9083-9100.

Korsgaard, N., Nuth, C., Khan, S., Kjeldsen, K., Bjørk, A., Schomacker, A. and Kjær, K. (2016). Digital elevation model and orthophotographs of Greenland based on aerial photographs from 1978–1987. *Scientific Data*, 3.

LaMorte, W. (2017). *Mann Whitney U Test (Wilcoxon Rank Sum Test)*. [online] Sphweb.bumc.bu.edu. Available at: http://sphweb.bumc.bu.edu/otlt/mph-modules/bs/bs704_nonparametric/BS704_Nonparametric4.html [Accessed 28 Feb. 2018].

Lever, J., Krzywinski, M. and Altman, N. (2017). Points of Significance: Principal component analysis. *Nature Methods*, 14(7), pp.641-642.

Morlighem, M., Williams, C., Rignot, E., An, L., Arndt, J., Bamber, J., Catania, G., Chauché, N., Dowdeswell, J., Dorschel, B., Fenty, I., Hogan, K., Howat, I., Hubbard, A., Jakobsson, M., Jordan, T., Kjeldsen, K., Millan, R., Mayer, L., Mouginot, J., Noël, B., O'Cofaigh, C., Palmer, S., Rysgaard, S., Seroussi, H., Siegert, M., Slabon, P., Straneo, F., van den Broeke, M., Weinrebe, W., Wood, M. and Zinglersen, K. (2017). BedMachine v3: Complete Bed Topography and Ocean Bathymetry Mapping of Greenland From Multibeam Echo Sounding Combined With Mass Conservation. *Geophysical Research Letters*, 44(21), pp.11051-11061.

NASA (2018). *Landsat Spacecraft Orbit*. [online] Landsat.gsfc.nasa.gov. Available at: https://landsat.gsfc.nasa.gov/landsat-spacecraft-orbit/ [Accessed 2 Aug. 2018].

Nienow, P., Sole, A., Slater, D. and Cowton, T. (2017). Recent Advances in Our Understanding of the Role of Meltwater in the Greenland Ice Sheet System. *Current Climate Change Reports*, 3(4), pp.330-344.

Noël, B., van de Berg, W., van Wessem, J., van Meijgaard, E., van As, D., Lenaerts, J., Lhermitte, S., Kuipers Munneke, P., Smeets, C., van Ulft, L., van de Wal, R. and van den Broeke, M. (2018). Modelling the climate and surface mass balance of polar ice sheets using RACMO2 – Part 1: Greenland (1958–2016). *The Cryosphere*, 12(3), pp.811-831.

Nye, J. (1953). The Flow Law of Ice from Measurements in Glacier Tunnels, Laboratory Experiments and the Jungfraufirn Borehole Experiment. *Proceedings of the Royal Society A: Mathematical, Physical and Engineering Sciences*, 219(1139), pp.477-489.

Parizek, B. and Alley, R. (2004). Implications of increased Greenland surface melt under global-warming scenarios: ice-sheet simulations. *Quaternary Science Reviews*, 23(9-10), pp.1013-1027.

Paterson, W. (1994). *The Physics of Glaciers*. 3rd ed. Oxford: Elsevier Science.

Pimentel, S. and Flowers, G. (2010). A numerical study of hydrologically driven glacier dynamics and subglacial flooding. *Proceedings of the Royal Society A: Mathematical, Physical and Engineering Sciences*, 467, pp.537-558.

Pritchard, H., Arthern, R., Vaughan, D. and Edwards, L. (2009). Extensive dynamic thinning on the margins of the Greenland and Antarctic ice sheets. *Nature*, 461(7266), pp.971-975.

Röthlisberger, H. (1972). Water Pressure in Intra- and Subglacial Channels. *Journal of Glaciology*, 11(62), pp.177-203.

Roy, D., Wulder, M., Loveland, T., Woodcock, C., Allen, R., Anderson, M., Helder, D., Irons, J., Johnson, D., Kennedy, R., Scambos, T., Schaaf, C., Schott, J., Sheng, Y., Vermote, E., Belward, A., Bindschadler, R., Cohen, W., Gao, F., Hipple, J., Hostert, P., Huntington, J., Justice, C., Kilic, A., Kovalskyy, V., Lee, Z., Lymburner, L., Masek, J., McCorkel, J., Shuai, Y., Trezza, R., Vogelmann, J., Wynne, R. and Zhu, Z. (2014). Landsat-8: Science and product vision for terrestrial global change research. *Remote Sensing of Environment*, 145, pp.154-172.

Scambos, T., Dutkiewicz, M., Wilson, J. and Bindschadler, R. (1992). Application of image cross-correlation to the measurement of glacier velocity using satellite image data. *Remote Sensing of Environment*, 42(3), pp.177-186.

Schoof, C. (2005). The effect of cavitation on glacier sliding. *Proceedings of the Royal Society A: Mathematical, Physical and Engineering Sciences*, 461(2055), pp.609-627.

Schoof, C. (2010). Ice-sheet acceleration driven by melt supply variability. *Nature*, 468(7325), pp.803-806.

SciPy Cookbook (2012). *Savitzky Golay Filtering — SciPy Cookbook documentation*. [online] Scipy-cookbook.readthedocs.io. Available at: http://scipy-cookbook.readthedocs.io/items/SavitzkyGolay.html [Accessed 14 Jul. 2018].

Sole, A., Nienow, P., Bartholomew, I., Mair, D., Cowton, T., Tedstone, A. and King, M. (2013). Winter motion mediates dynamic response of the Greenland Ice Sheet to warmer summers. *Geophysical Research Letters*, 40(15), pp.3940-3944.

Straneo, F. and Heimbach, P. (2013). North Atlantic warming and the retreat of Greenland's outlet glaciers. *Nature*, 504, pp.36-43.

Sundal, A., Shepherd, A., Nienow, P., Hanna, E., Palmer, S. and Huybrechts, P. (2011). Melt-induced speed-up of Greenland ice sheet offset by efficient subglacial drainage. *Nature*, 469(7331), pp.521-524.

Tedstone, A., Nienow, P., Gourmelen, N., Dehecq, A., Goldberg, D. and Hanna, E. (2015). Decadal slowdown of a land-terminating sector of the Greenland Ice Sheet despite warming. *Nature*, 526(7575), pp.692-695.

Tedstone, A., Nienow, P., Sole, A., Mair, D., Cowton, T., Bartholomew, I. and King, M. (2013). Greenland ice sheet motion insensitive to exceptional meltwater forcing. *Proceedings of the National Academy of Sciences*, 110(49), pp.19719-19724.

USGS (2018a). *Landsat 8 Data Users Handbook - Section 2*. [online] Landsat.usgs.gov. Available at: https://landsat.usgs.gov/landsat-8-l8-data-users-handbook-section-2 [Accessed 29 Apr. 2018].

USGS (2018b). *How does Landsat 8 differ from previous Landsat satellites?*. [online] Landsat.usgs.gov. Available at: https://landsat.usgs.gov/how-does-landsat-8-differ-previous-landsat-satellites [Accessed 2 Aug. 2018].

USGS (2018c). *Landsat Processing Details*. [online] Landsat.usgs.gov. Available at: https://landsat.usgs.gov/landsat-processing-details [Accessed 29 Apr. 2018].

van de Wal, R., Smeets, C., Boot, W., Stoffelen, M., van Kampen, R., Doyle, S., Wilhelms, F., van den Broeke, M., Reijmer, C., Oerlemans, J. and Hubbard, A. (2015). Self-regulation of ice flow varies across the ablation area in south-west Greenland. *The Cryosphere*, 9(2), pp.603-611.

van der Veen, C. (2007). Fracture propagation as means of rapidly transferring surface meltwater to the base of glaciers. *Geophysical Research Letters*, 34(L01501).

Walder, J. (1986). Hydraulics of Subglacial Cavities. *Journal of Glaciology*, 32(112), pp.439-445.

Zwally, H., Abdalati, W., Herring, T., Larson, K., Saba, J. and Steffen, K. (2002). Surface Melt-Induced Acceleration of Greenland Ice-Sheet Flow. *Science*, 297(5579), pp.218-222.

Zwally, J., Giovinetto, M., Beckley, M. and Saba, J. (2012). *Antarctic and Greenland Drainage Systems*. [online] GSFC Cryospheric Sciences Laboratory. Available at: https://icesat4.gsfc.nasa.gov/cryo_data/ant_grn_drainage_systems.php [Accessed 9 May 2018].

Technical Report

Table of Contents

Table of Figures

Table of Tables

1. Introduction:

1.1. Aims of technical report:

The purpose of this technical report is to provide in-depth detail on the methods used in the associated research paper, such that they may be reproduced. This report also contains raw data outputs that aid understanding of final results but that are beyond the scope of the research paper.

Throughout this study, a series of well-established techniques are reproduced and developed. Table 1 distinguishes between previously established techniques, those that were further developed as part of this study and those that were created specifically for this study. Furthermore, table 1 advises on the studies from which techniques have been reproduced.

Table 1: Origins of processing techniques used in this study. Green = developed here, blue = developed past technique, orange = replicated past technique.

Stage	Technique(s)	Technique origin(s)
Image downloads	All	Multitude of studies
Sensitivity analysis	All	Tedstone et al (2015)
Pre-processing	L0DIR, template files and pair lists	Dehecq et al (2015) and Tedstone et al (2015)
	Principle components analysis	Dehecq et al (2015) and Tedstone et al (2015)
	High-pass Gaussian filter	Multitude of studies
Feature tracking	Eddie 3	Dehecq et al (2015) and Tedstone et al (2015)
	Orientation correlation	Fitch et al (2002)
Parameter setting	Parameter setting technique	Dehecq et al (2015)
	Gaussian filter Scan Line Corrector-off test	Developed here
	Incorrect band discovery	Developed here
	Band choices	Tedstone et al (2015)
Post-processing	Median coregistration	Tedstone et al (2015)
	Fusion	Dehecq et al (2015) and Tedstone et al (2015)
	Uncertainty quantification	Dehecq et al (2015)
	Study area delineation	Developed here
	Point extraction rules	Tedstone et al (2015)
Performance indicators	All maps	Dehecq et al (2015)
	MeASUREs comparison	Developed by Josh Williams (personal communication)
Data analysis	All	Tedstone et al (2015)
Impact of changing geometries	All	Developed here

2. Detailed methodology:

2.1. Section outline:

The following section builds upon the methodological information presented in the research paper. First the process of feature tracking is outlined to ensure familiarity with key terminology. Following this, image acquisition, pre- and post-processing techniques are explained. Finally, information regarding the use of regional climate models and statistical tests is presented.

2.2. Feature tracking:

Feature tracking is the process whereby the distances that features have moved between a reference image and a more recently acquired search image are measured (Dehecq et al., 2015). With knowledge of image pair temporal separation, displacement can be converted to velocity.

Here, the Image Georectification and Feature Tracking (ImGRAFT) toolbox is used, which uses the 'templatematch.m' function to measure displacement (Messerli and Grinsted, 2015; Grinsted, 2015).

In a reference image, a reference window is defined, containing feature patterns to be tracked (Grinsted, 2015). The size of the reference window is dependent upon the size of features that the user wishes to track and the desired resolution of the final velocity map (Grinsted, 2015). The reference window is translated across the reference image separated by a user defined number of pixels (the step) to ensure that all trackable feature patterns are accounted for (figure 1).

Finally, search windows are defined in the search image, each paired to a reference window. Their size corresponds to the level of displacement that is expected to have taken place between image acquisitions (Grinsted, 2015). Patterns found within the reference and corresponding search windows are compared using a function of similarity. If similarity is high, displacement can be measured (Dehecq et al., 2015).

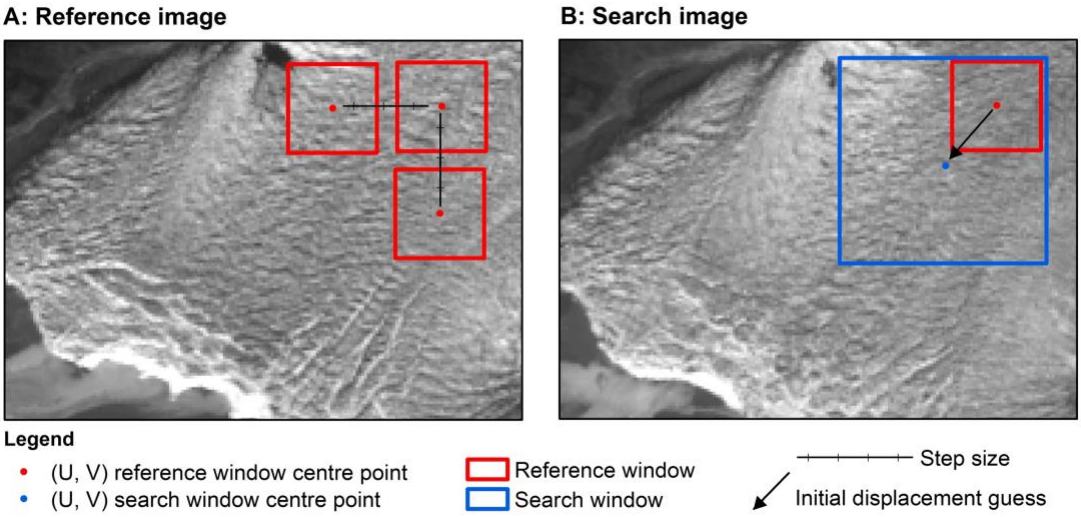

Figure 1: Illustration of how feature tracking is carried out on optical images using the ImGRAFT 'templatematch.m' function (Grinsted, 2015). For visual purposes, 'step size' has been exaggerated. Reference windows should overlap one another to ensure all trackable features are discovered.

2.3. Image downloads:

Feature tracking is carried out on Landsat images acquired from the USGS and ESA. Each Landsat mission required a different technique to download the imagery. The bands of each scene are stored in GeoTIFF format.

2.3.1. Data acquisition reasoning:

All available imagery in each archive is downloaded, as manually sorting images through subjective filtering is time consuming and increases the chances of potentially useful images being disregarded (Dehecq et al., 2015). This leads to increased time spent processing image pairs. The processing can, however, be carried out overnight effectively reducing the number of working hours consumed. Poor quality images are eventually filtered out in the fusion process (section 2.8.2).

2.3.2. Path/row selection:

Scenes are only downloaded if they cover a sufficient amount of the region of interest. The Worldwide Reference System-2 (WRS2) is a navigation system used for Landsat data (NASA, 2018a). It allows product users to navigate to specific scenes, sorted by path and row (NASA, 2018a). To locate the useful WRS2 path/row combinations, a polygon shapefile of the study region was created using the 'click2shape' browser based shapefile creation tool (UCLA, 2018). A Python script (author – Josh Williams) was then used to extract all path/row combinations that intersect the shapefile (figure 2).

The scenes used initially were from paths 007 to 011, row 011. However, upon inspection of image quality, path 007 was excluded from feature tracking for all Landsat missions and

path 008 was excluded from feature tracking for Landsats 5 and 7 missions. This is because scenes from these paths contained insufficient stable ground for median coregistration (section 2.8.1) and had a poor geolocational accuracy (section 2.3.3).

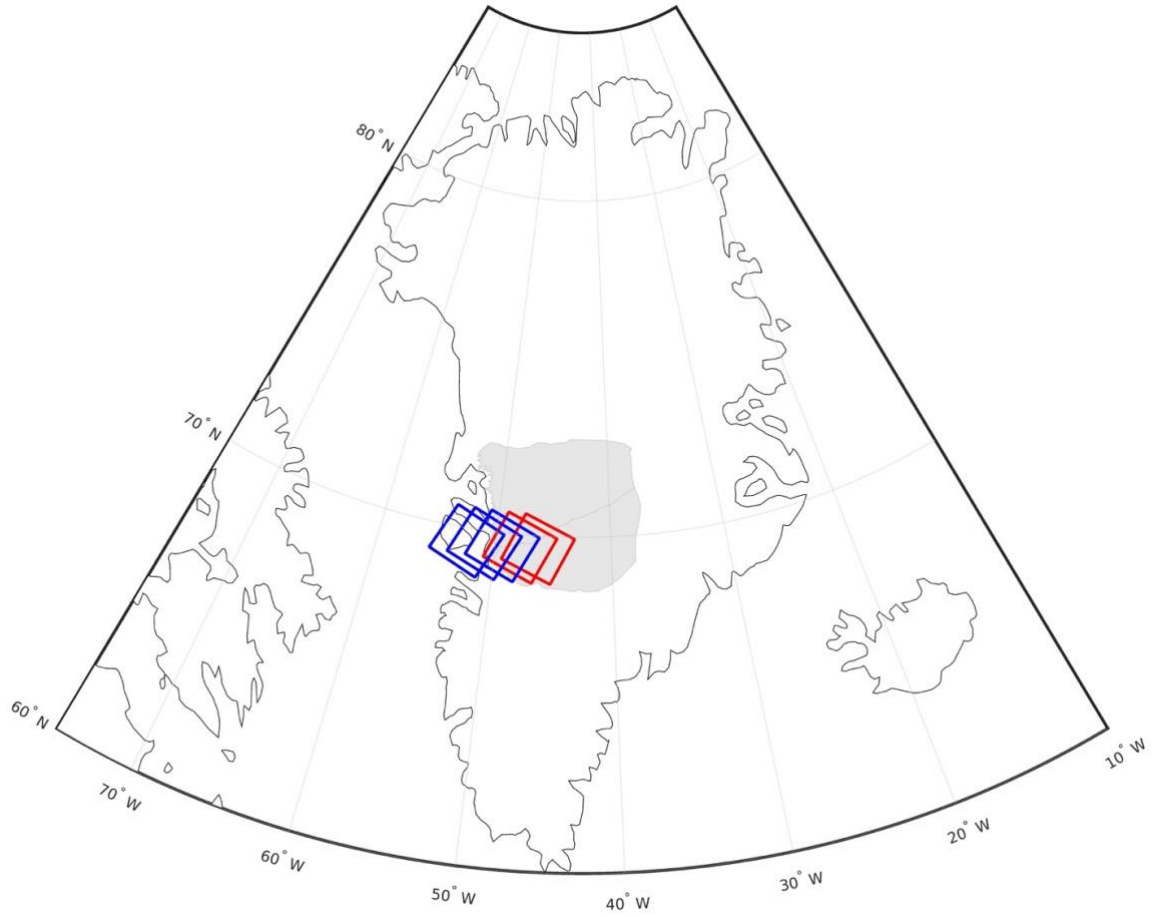

Figure 2: WRS2 path/row combinations used in this study. Blue boxes show paths 009-011, row 011. Red boxes show paths 007-008, row 011. Script for figure production supplied by Josh Williams.

2.3.3. Image quality requirements:

All scenes are required to be of tier 1 (T1) quality. T1 scenes are radiometrically corrected, orthorectified and have a geolocational accuracy of better than 12 m (USGS, 2018a, 2018b).

Tier 2 (T2) images have a geolocational accuracy worse than 12 m (USGS, 2018b). These were initially downloaded for use. They are not, however, included in final velocity products, due to the fact that they generate line-type artefacts (figure 3) on velocity maps and have an insufficient geolocational accuracy. Their insufficient geolocational accuracy is caused by the fact that they contain no visible stable ground, therefore ground control points used for georeferencing cannot be identified (USGS, 2018b).

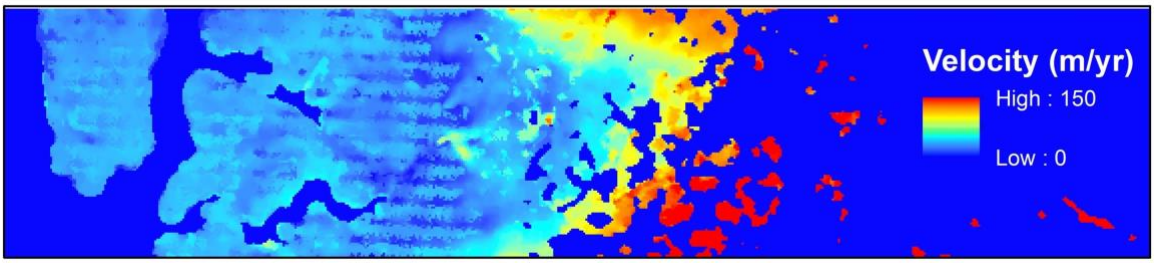

Figure 3: Example of 'line-type' artefacts generated when using T2 derived velocity maps in the fusion process. Velocity maps were derived using the panchromatic band of Landsat 8 for the period 2016-2017.

2.3.4. Image temporal separation:

Scenes used for feature tracking were collected between April and October from 1985 to 2016, with a temporal baseline of 352 to 400 days (22-25 repeat cycles) (Tedstone et al., 2015). The ~1-year temporal baseline allows for the derivation of average annual velocities while reducing sample bias caused by seasonal flow variability (Tedstone et al., 2015; Dehecq et al., 2015).

2.3.5. Download techniques:

2.3.5.1. Landsat 8 (2013 – 2016):

Landsat 8 OLI data were downloaded using the USGS Bulk Download Application (BDA) (USGS, 2018c). Here, the USGS EarthExplorer portal is used to select all available imagery of path/row combinations that are deemed to be useful. The BDA can be used to download these data in one sitting in '.tar.gz' compressed format.

2.3.5.2. Landsat 5 (1985 – 1999):

Landsat 5 TM data were downloaded from the 'ESA Online Dissemination' webpage (ESA, 2018). This webpage stores all T1 imagery covering Europe and Greenland in '.zip' compressed format. To efficiently download these images the user must navigate manually to each path/row combination. Following this the 'DownThemAll' (dTa) Mozilla Firefox extension is used (Maier et al., 2018). Here, the user specifies '.zip' as the file format and dTa proceeds to download all files with this extension.

2.3.5.3. Landsat 7 Scan Line Corrector-on (1999 – 2003) and Scan Line Corrector-off (2003 – onward):

In 2003 the Scan Line Corrector (SLC) instrument onboard Landsat 7 failed, consequently a black striping pattern is observed on all Landsat 7 scenes from 31/03/2003 onward (USGS, 2018d). Landsat 7 ETM+ SLC-off data are not stored on the ESA Online Dissemination webpage. Similarly, the ESA Online Dissemination webpage only provides a small amount of SLC-on data. Therefore, these data were downloaded using the BDA.

2.4. Data availability:

Excluding paths 008 (except for Landsat 8 OLI) and 007 (section 2.3.2), 599 images were downloaded, generating 1117 image pairs. In total 450 images and 786 image pairs were utilised in the final velocity time series. This study utilises 311 more image pairs than Tedstone et al (2015). This is likely partially due to the longer duration of the study period and the greater availability of T1 processed imagery. Pair numbers are consistently higher than the number of images used, because single images can make up parts of multiple pairs (appendix 5.4.1).

Landsat 5 TM pair availability is roughly consistent over its operational period, whereas Landsat 7 ETM+ pair availability increased throughout (figure 4). Landsat 8 OLI showed greatest pair availability in 2014-2015. The difference in image pair availability for each sensor provides motivation to carry out a sensitivity analysis to understand whether temporal separation characteristics have an effect on derived velocities (section 2.4.1).

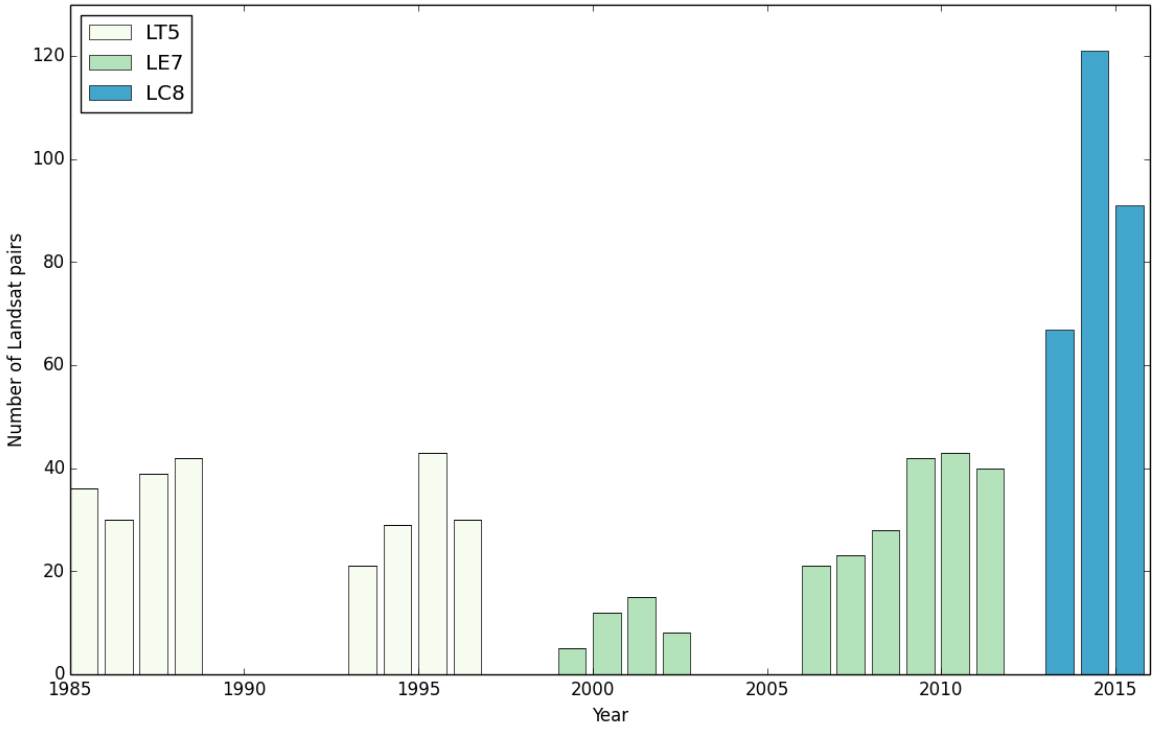

Figure 4: Graph showing the distribution of image pair availability for feature tracking from 1985 to 2016, excluding pairs not utilised in the final velocity time series. Script for figure production supplied by Dr. Amaury Dehecq.

2.4.1. Impact of image pair temporal characteristics on velocity derivation – sensitivity analysis:

It should be noted that following the launch of Landsat 7 in 1999, a ~15 day increase in average baseline duration was observed by Tedstone et al (2015). This caused a ~2% increase the proportion of baseline velocities attributable to the effects of summer ice-flow

and therefore ~2 m yr^{-1} of velocity change was deemed attributable to image pair temporal separation characteristics (Tedstone et al., 2015).

Here, the same sensitivity analysis (appendix 5.5.1.2) as Tedstone et al (2015) is carried out. Average winter (81.6 m yr^{-1}) and summer (127.6m yr^{-1}) velocities measured on the Leveret glacier (located ~260 km south of the study area) are used to predict the change in velocity that image pair temporal characteristics could cause (Sole et al., 2013; Tedstone et al., 2013, 2015). Image pair temporal characteristics cause a maximum predicted velocity variation of less than 0.9 m yr^{-1} as a result of an increase in attribution to summer velocities of less than 2% (figure 5). Because, the pattern of attribution to summer velocities does not match the trend presented in the final velocity time series (research paper – figure 4), it is likely that image pair temporal characteristics have a negligible effect.

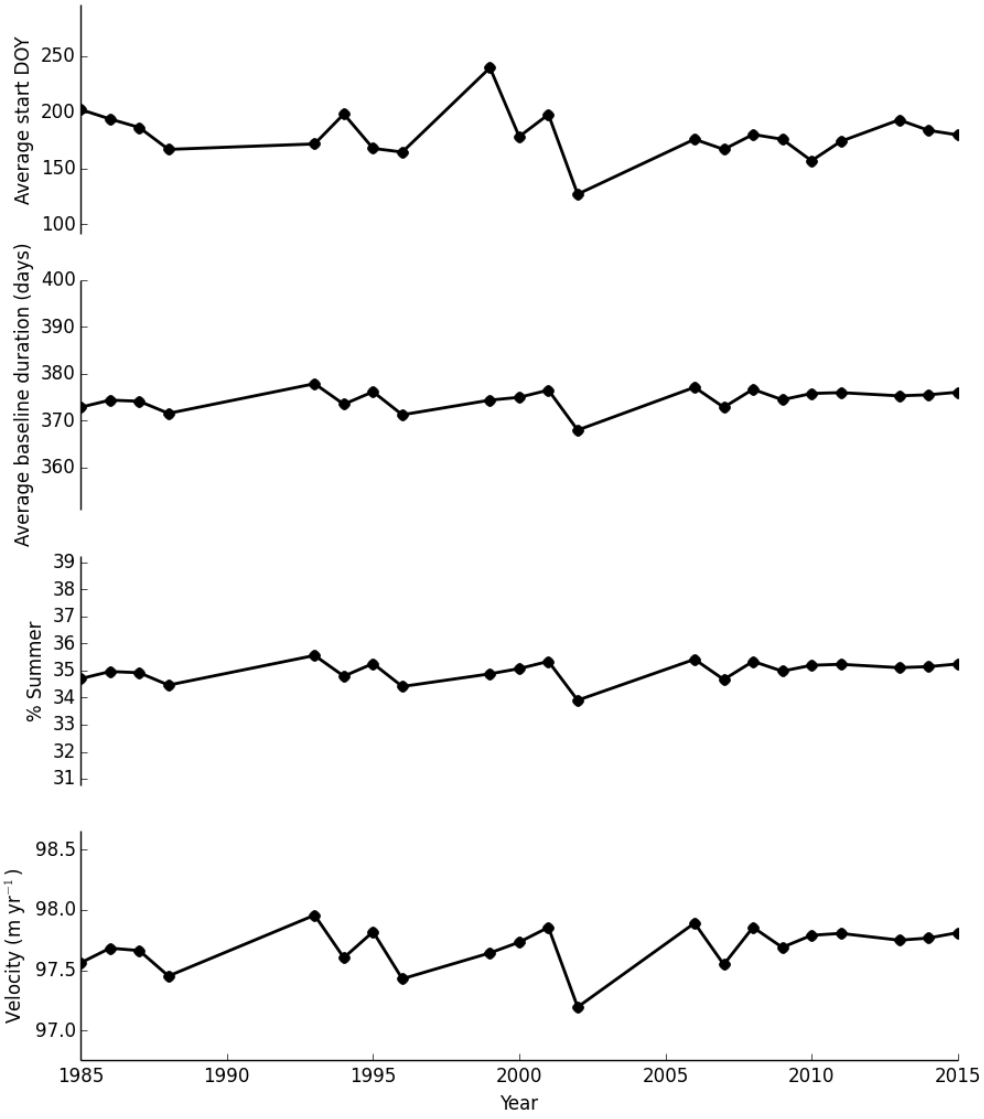

Figure 5: In descending order – average start day of image pairs, average baseline duration of image pairs, average percentage velocity attributable to summer motion and predicted velocities based on pair temporal characteristics using average winter and summer velocity measurements from the Leveret glacier (Tedstone et al., 2013; Sole et al., 2013). Measurements correspond to each year of velocity observation used in this study.

2.5. Pre-processing:

2.5.1. The L0DIR:

Due to large disk space requirements and the automated processing technique used to generate velocity maps, all images were stored in a directory called 'L0DIR' on the University of Edinburgh Earth Observation datastore, sorted by /mission/path/row. Python scripts (authors – Dr. Amaury Dehecq and Josh Williams) were used to unpack and move user specified bands from the '.tar.gz' and '.zip' downloaded formats to the L0DIR directory.

2.5.2. Template files:

A template file was created in a specific format for each Landsat mission; this file is utilised by various Python scripts throughout the pre- and post-processing stages. This contained information on:

- The time period over which image pairs should be searched for
- The path/row combinations that should be utilised (section 2.3.2)
- The temporal baseline of image pairs (in Landsat cycles – section 2.3.4)
- The bands to use for feature tracking (section 2.7.4)
- The principle component to be used for feature tracking (section 2.5.4)
- The size of high-pass gaussian filter to be used (in metres – section 2.7.3)
- The search window size (in pixels – section 2.7.2)
- The reference window size (in pixels – section 2.7.2)
- The step size (in pixels – section 2.7.2)
- The expected maximum velocity (in metres per year – section 2.7.2)

2.5.3. Pair lists:

Using template files, pair lists are created which list the image pairs that feature tracking is to be carried out on. A Python script (author – Dr. Amaury Dehecq) searches the L0DIR for potential pairs based upon temporal and locational parameters outlined in the template file. Images are excluded from pair lists if their metadata reveals that they are too cloudy.

2.5.4. Principle components analysis:

Principle components analysis (PCA) was used to enhance the provided signal from all sensors (Dehecq et al., 2015). PCA projects variables (information from different image spectral bands) into fewer orthogonal dimensions, known as principle components (PCs) (Lever et al., 2017). This aims to maximise the variance of the dataset while retaining useful information (Lever et al., 2017; Dehecq et al., 2015; Scambos et al., 1992). As outlined in the research paper (see research paper – section 2.3), this is particularly useful for applications on the GrIS as it reduces saturation caused by high surface albedo values (a problem associated with Landsats 5 and 7 data) and reduces the visibility of thin clouds, improving feature tracking results (Ahn and Howat, 2011). PCA is carried out on both the reference and search image before feature tracking is undertaken.

2.5.5. Gaussian filter:

Finally, prior to feature tracking a high-pass gaussian filter (HPGF) is applied. The aim here is to allow unity gain for features of a high frequency and zero gain at low frequencies following a Fourier transform to the frequency domain (Thompson and Emery, 2014; Gonzalez and Woods, 2002).

High frequency components of images usually correspond to sharp changes in grey level, in this context caused by trackable features (Gonzalez and Woods, 2002). Therefore, this method enhances the visibility of small trackable features such as crevasses, sastrugi and debris (figure 6) while reducing the visibility of large, stationary features caused by topographic variability at the base of the ice sheet (Fahnestock et al., 2016; Scambos et al., 1992; Berthier et al., 2003; Ahn and Howat, 2011). This allows velocities to be mapped further into the ice sheet interior (Fahnestock et al., 2016).

The HPGF of the frequency domain follows the transfer function:

$$H(u,v) = 1 - e^{-D^2(u,v)/2{D_0}^2}$$ *Equation 1. (Gonzalez and Woods, 2002)*

where D_0 is the cut-off frequency whereby a distinction is made between unity and zero gain and $D(u,v)$ is the distance from the point (u,v) to the frequency rectangle centre, around which filters are symmetrical (Gonzalez and Woods, 2002).

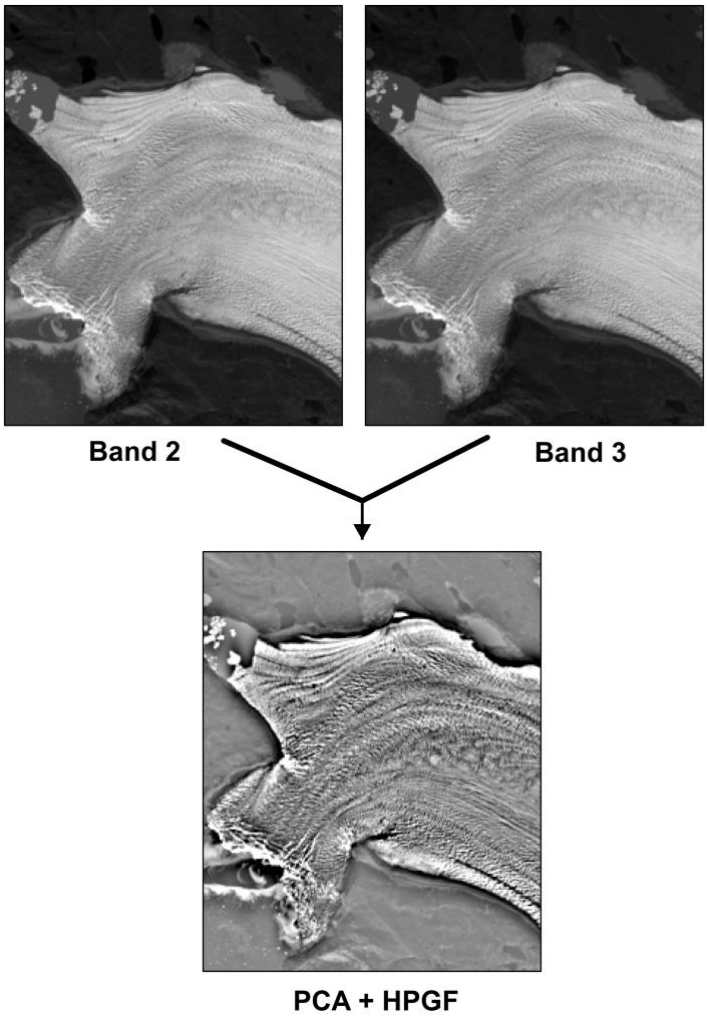

Figure 6: Example of image produced following application of HPGF and PCA on bands two and three of a Landsat 8 OLI scene.

2.6. Feature tracking - continued:

2.6.1. Eddie3:

Feature tracking, PCA and HPGF application were carried out on the University of Edinburgh Eddie3 computing cluster, due to extensive memory requirements and parallel processing capabilities (University of Edinburgh, 2017). Processing time is dependent upon the number of available nodes.

2.6.2. Orientation correlation:

Orientation correlation (OC) is used as the feature tracking method. As outlined in the research paper (see research paper – section 2.2), it is important to use OC because it allows tracking on post-2003 Landsat 7 SLC-off scenes (Dehecq et al., 2015; Heid and Kääb, 2012). This is because uniform areas (where scan lines are located) have an intensity gradient of

zero, therefore due to the multiplicative nature of the correlation, these areas will have no effect (Fitch et al., 2002; Heid and Kääb, 2012).

The tracking of normalised intensity gradients also means that this method is illumination invariant (Fitch et al., 2002), which reduces errors caused by shadowing.

The orientation image creation algorithm follows the equation:

$$f_d(x,y) = sgn(\frac{\partial f(x,y)}{\partial x} + i\frac{\partial f(x,y)}{\partial y}) \qquad \textit{Equation 2. (Fitch et al., 2002)}$$

where x and y are the integer coordinates to which images are indexed, f is a discrete image, f_d is an orientation image, i represents an imaginary number (a rotation) and $sgn(x)$ is the sign function which extracts the sign of x. Following this, using a function of similarity, features from f_d can be tracked on a more recently acquired search image which has been subjected to the same pre-processing (Dehecq et al., 2015).

2.7. Parameter setting:

2.7.1. Parameter setting technique:

Parameters in the template file (section 2.5.2) were experimented with to find the combination which produced the best quality feature tracking results. In the interests of time, a single cloud free pair was experimented with for each sensor to derive optimum parameter choices (table 3 – section 2.7.4.2).

2.7.2. Window sizes:

The reference window size was set to 50 pixels, due to the fact that this provided the least noise at an acceptable resolution. This also meant that image pairs were processed in an acceptable time. Although choosing a reference window at a power of two reduces computation time (Dehecq et al., 2015), this produced poor quality feature tracking results which demonstrated either an excessive amount of noise or a poor spatial resolution.

The search window size was set to automatic and hence calculated as function of the temporal separation between each image pair, image resolution and the estimated maximum velocity parameter.

The expected maximum velocity parameter was set to 1000 m yr^{-1}, due to the fact that past velocity maps show neighbouring marine terminating glaciers heavily influence velocities in peripheral parts of the study region (ENVEO, 2017). Setting this parameter to 1000 m yr^{-1} also meant that processing time was not excessive (Dehecq et al., 2015).

2.7.3. Gaussian filter:

The HPGF size was set equal for all Landsat missions to ensure that it did not cause artificial patterns to present themselves. 2500 m was thought to be the optimum size, based upon inspection of test images.

2.7.3.1. Gaussian filtering on SLC-off images:

Gaussian filtering was not applied to Landsat 7 SLC-off images, as its application reduced the quality of velocity maps where scan lines are located (see research paper – figure 2). As mentioned in the research paper, a likely cause of this is that the HPGF causes zeroed intensity gradients at scan lines to be assigned values (e.g. Fitch et al., 2002).

When carrying out feature tracking on Landsat 7 ETM+ SLC-off images, it was not immediately obvious that the HPGF was the cause of signal loss in areas containing scan lines. Therefore an experiment was derived to diagnose the cause of the problem. This went as follows:

1) Carry out feature tracking using a reference window size increasing in 10 pixel increments from 20 to 100, while holding all other parameters constant
2) Define the reference window size at which best feature tracking results are produced
3) Using the optimum reference window size, carry out feature tracking using a HPGF size increasing in 500 m increments from 500 to 5000

Above a size of 1500 m the application of the HPGF failed. Coincidentally, feature tracking performance vastly improved, leading to the conclusion that the HPGF was the cause of the problem.

2.7.4. Band choices:

2.7.4.1. Initial band choices:

Initially, the panchromatic spectral band of the Landsat 7 ETM+ and Landsat 8 OLI sensors was used (table 2), due to the fact that it provides data at a 15 m spatial resolution (half that of the other available bands) (USGS, 2018e). This allows smaller features and therefore more detailed patterns to be tracked, leading to more complete velocity map coverage for each image pair and a greater confidence in results. For Landsat 5 TM data, the first PC of bands two and three was used, consistent with Tedstone et al (2015) who found these bands to be optimal.

To ensure that the resolution of final velocity maps was consistent, the reference window and step sizes were halved for feature tracking on Landsat 5 TM scenes, as the spatial resolution of the bands used (30 m) was double that of the panchromatic bands of Landsats 7 and 8.

Table 2: Initial parameters used for feature tracking process prior to discovery of inconsistent time series data.

Sensor	Reference window size (pixels)	Search window size (pixels)	Step size (pixels)	Gaussian filter size (m)	Spectral bands	Estimated maximum velocity (m yr^{-1})
OLI (LC8)	100	Automatic	16	2500	8	1000
ETM+ (LE7)	100	Automatic	16	2500 (NA for SLC-off)	8	1000
TM (LT5)	50	Automatic	8	2500	2&3	1000

These band choices were not employed for the final velocity outputs presented in this study, due to the fact that band choice has an effect on the measured velocity (section 3.1). This meant that inconsistent and incomparable time series results were produced.

2.7.4.2. Final band choices:

The final band choices used are shown in table 3. The first PC of bands two and three of each sensor were found to be optimum by Tedstone et al (2015) and are therefore used here due to close study region proximity.

All parameters are consistent across each Landsat mission as images are of the same spatial resolution. Altering parameters for just one mission would reduce comparability and the confidence that any temporal patterns were genuine.

Table 3: Corrected parameters used for feature tracking process following discovery of inconsistent time series data.

Sensor	Reference window size (pixels)	Search window size (pixels)	Step size (pixels)	Gaussian filter size (m)	Spectral bands	Estimated maximum velocity (m yr^{-1})
OLI (LC8)	50	Automatic	8	2500	2&3	1000
ETM+ (LE7)	50	Automatic	8	2500 (NA for SLC-off)	2&3	1000
TM (LT5)	50	Automatic	8	2500	2&3	1000

2.8. Post-processing:

2.8.1. Median coregistration:

Coregistration is the process whereby reference and search images are spatially aligned to ensure that artificial results are not generated. Previously, image coregistration has been carried out prior to feature tracking using a Global Land Survey (GLS) reference dataset, whereby images are resampled to a GLS derived grid using ground control points (e.g.

Dehecq et al., 2015). Coregistration has also been carried out using low-pass filters, whereby a filter is used to enhance the appearance of quasi-stationary surface features associated with topographic protrusions at the ice sheet bed (Fahnestock et al., 2016; Scambos et al., 1992; Berthier et al., 2003). These features are then coregistered using normalised cross correlation (Fahnestock et al., 2016).

Using quasi-stationary features for coregistration would allow the use of scenes from paths 008 and 007. However, performance on Landsat 5 TM derived images is temperamental (Fahnestock et al., 2016). Furthermore, for coregistration to be performed well using the GLS reference dataset, sufficient stable ground must be visible and well distributed within each scene USGS, 2018f). Therefore an alternative, computationally simple method known as median coregistration is used following the feature tracking process.

As outlined in the research paper methodology (see research paper – section 2.4), median coregistration (script author – Dr. Andrew Tedstone) computes the median X and Y velocity components of stable areas. To ensure that the correction accounts for the direction of flow, the respective median value is then subtracted from the entire directional velocity component before derivation of the final velocity map. This eliminates the signal caused by coregistration inaccuracy.

2.8.2. Fusion:

Following the feature tracking process and median coregistration, fusion is carried out whereby velocity maps covering specified coincident time periods are merged. Velocity maps are merged using a median based approach to reduce the effects of outliers (Dehecq et al., 2015; Tedstone et al., 2015). This is a robust method, as the causes of outliers (e.g. clouding and orthorectification errors) are unlikely to be present in the same place in multiple image pairs (Dehecq et al., 2015).

Prior to fusion, each pixel is assigned the median value of all pixels within a 240 m radius, further reducing the effects of outliers (Dehecq et al., 2015). Furthermore, a subjective judgement is made regarding the signal to noise ratio (SNR) that is permissible in final fused images. Pixels exhibiting a value below this threshold are removed. Additionally, the median value obtained through fusion is only retained if it has been derived using five or more spatially coincident pixels, to increase the reliability of results (Dehecq et al., 2015).

During the fusion process a Python script (author – Dr. Amaury Dehecq) accesses a pair list and parameters within a template file to learn which image pairs require merging. To produce final fused velocity maps, directional components are combined using the following equation:

$$V = \sqrt{{V_x}^2 + {V_y}^2} \qquad \textit{Equation 3.}$$

where V is the final velocity product and V_x and V_y are the directional components of velocity.

2.8.3. Uncertainty quantification:

The uncertainties associated with final fused velocities are known to decrease as greater numbers of individual observations are used in the fusion process (Dehecq et al., 2015). Therefore, uncertainty is quantified using the measured fused velocities of stationary areas and their relationships with the number of points used to derive them (Dehecq et al., 2015).

Using equation 4, the 95% confidence interval (t_{95}) of each fused pixel located in off-ice areas (where velocity is known to be zero) can be calculated:

$$t_{95} = k\frac{\sigma}{N^a} \qquad \textit{Equation 4. (Dehecq et al., 2015)}$$

where N is the number of velocity observations used to compute the median absolute deviation (MAD – a measure of dispersion of observations) (σ) (section 2.8.5.1) at each point and k and a are parameters to be resolved (Dehecq et al., 2015).

A logarithm is then applied to equation 4 to extract a linear relationship between the confidence of velocity measurements and the associated number of input points:

$$log\left(\frac{t_{95}}{\sigma}\right) = p_0 + p_1 log(N) \qquad \textit{Equation 5. (Dehecq et al., 2015)}$$

This linear relationship can be used to extrapolate the initial relationship to on-ice areas, providing a confidence estimate for each pixel.

Uncertainty is calculated using an automated Python script (author – Dr. Amaury Dehecq) where an ice mask is used to locate stable areas (Howat et al., 2014; Dehecq et al., 2015).

2.8.4. Extraction of common velocity points:

2.8.4.1. Study area delineation:

To aid comparison with Tedstone et al (2015), velocities were only extracted from areas deemed to be primarily affected by the dynamics of land-terminating ice. Thus, a vector field was generated using ESRI's ArcGIS 'vector field renderer function'. This uses X and Y velocity components to calculate flow direction.

Following this, a shapefile was manually derived (figure 7), excluding areas where flow was deemed to be affected by neighbouring marine-terminating glaciers (i.e. not flowing perpendicular to the margin). This shapefile is used as the basis for creating a study area.

The vector field and therefore the shapefile are based upon a 2015-2016 velocity map. To ensure that study area delineation remained applicable for all other velocity observations, a 2 km interior buffer (figure 7) was added to mitigate the effects of changing velocity patterns over the study period. This also reduces the risk of human error associated with shapefile creation.

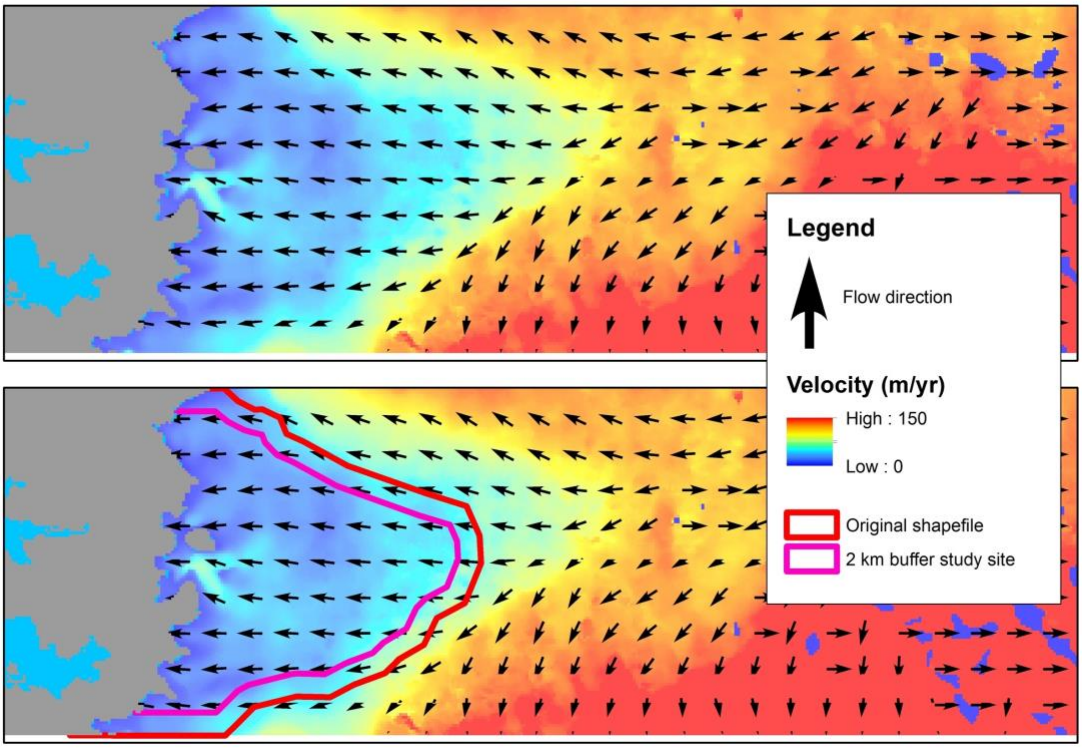

Figure 7: Top – vector field map showing flow direction, overlain on a 2015-2016 velocity map. Bottom – also shows the locations of the originally derived study area (red) and the interior 2 km buffer used as the final study area (pink) from which common points are extracted.

2.8.4.2. Point extraction rules:

To create a velocity time series, it is important that only overlapping points are extracted from each velocity map. This was achieved using a MATLAB script (author – Josh Williams). Here, individual pixels exhibiting less than 60 m yr^{-1} error, found in fused scenes with greater than 30% study area spatial coverage (figure 7) are used to generate a time series, given that they are present in all scenes across the study period. The 30% spatial coverage threshold was chosen as a compromise between having a sufficient number of common points and annual velocity observations. The error threshold applied here adds an extra dimension of integrity to median velocity observations.

2.8.5. Performance indicators:

As part of the fusion process, a number of indicators are created which provide information on the final quality of fused velocity maps. Performance is also tested by comparing results with those derived using different techniques.

2.8.5.1. Median absolute deviation:

The MAD is a measure of dispersion of the values used to create each median value in final fused velocity maps, carried out on a pixelwise basis. It is used as an alternative to the standard deviation, as outliers tend to stretch distributions of velocity observations, reducing their normality (Burgess et al., 2013; Dehecq et al., 2015).

The pixelwise MAD (σ) is calculated using the following equation:

$$\sigma(i,j) = 1.483 \times med_{t \epsilon T}(|V(i,j,t) - \bar{V}(i,j)|)$$ *Equation 6. (Dehecq et al., 2015)*

where (i,j) is a pixel location and T is the set of velocity measurements ($V(i,j,t)$), which are fused to produce the median velocity ($\bar{V}$) (Dehecq et al., 2015). The lower the MAD, the more likely it is that the final fused velocity in a robust estimator for the specified time period.

2.8.5.2. Coherence:

The coherence measures the degree to which the direction of velocities used to generate a median value at each pixel agree with one another (Dehecq et al., 2015). It is measured on a scale of 0 to 1, where 1 shows the highest uniformity and 0 shows that directions are random.

Coherence (VVC) is calculated using the following equation:

$$VVC(i,j) = \frac{||\sum_{t \epsilon T} \vec{V}(i,j,t)||}{\sum_{t \epsilon T} ||(\vec{V}(i,j,t)||}$$ *Equation 7. (Dehecq et al., 2015)*

2.8.5.3. Number of points:

A further measure of performance is the number of points used to generate each median velocity value. This gives an additional indication as to how robust the pixelwise result is as areas that exhibit a higher number of input points are likely to more accurately represent the average.

2.8.5.4. Comparison with Making Earth System Data Records for use in Research Environments (MeASUREs) observations:

As a final performance indicator, annual velocity data is compared with MeASUREs observations from 2001 to 2016 (script author – Josh Williams). MeASUREs observations over this period are derived using synthetic aperture radar (SAR), and in later years are supplemented with Landsat 8 data (Joughin, 2017; Joughin et al., 2010). SAR data are acquired over 6 or 12 day repeat cycles and then converted to annual velocities by averaging all observations at individual points (Joughin, 2002).

For the period 2001 to 2013, 500 m spatial resolution MeASUREs data is oversampled to the same resolution as measurements (240 m) from this study, to allow comparison. This stops the creation of artificial observations, which would occur if undersampling of data derived in this study was carried out. For the same reason, when comparing observations over the period 2014 to 2016, data from this study is oversampled, rather than MeASUREs data. This is due to the fact that MeASUREs data for this period has a spatial resolution of 200 m.

Comparison with a different velocity derivation technique will help ratify, or renounce, the results presented in this study.

2.9. Regional climate models:

This study utilises runoff data from the Regional Atmospheric Climate Model-2 (RACMO2.3p2) and the Modèle Atmosphérique Régional (MAR). Both RACMO2.3p2 and MAR are forced every six hours at their lateral boundaries with ERA-Interim reanalysis data from 1979 to 2016 (Noël et al., 2016, 2018) and 1979 to 2015 (Fettweis et al., 2017), respectively. Therefore, the extent to which this study can assess the effects of antecedent runoff is limited to 2016, as forcing does not extend beyond this period (Fettweis et al., 2017; Noël et al., 2016, 2018).

2.9.1. Data manipulation:

Runoff data for the entire GrIS was downloaded in '.nc' format. Following this, MATLAB scripts (author – Josh Williams) were used to read the data. To define the area over which runoff data were utilised a GeoTIFF was created of all drainage basins that intersect the study region. Drainage basins 7.1 and 7.2 were downloaded from the 'Ice Sheet Mass Balance Inter-comparison Exercise' (IMBIE) website in text format (Zwally et al., 2012; IMBIE, 2016). These data were then converted to GeoTIFF format.

An elevation threshold of 1000 m was also used to ensure that runoff data was only utilised for areas of similar elevation to velocity observations, improving the authenticity of comparison. The elevation threshold was implemented using the 90 m GIMP DEM (Howat et al., 2014).

2.9.2. Modèle Atmosphérique Régional:

2.9.2.1. Model description:

MAR 3.5.2 is coupled to the 1D Surface Vegetation Atmosphere Transfer Scheme (SISVAT) (Gallée and Schayes, 1994). SISVAT models energy exchanges between sea-ice, the GrIS, tundra and the atmosphere (Gallée and Schayes, 1994; Fettweis et al., 2013). SISVAT also accounts for the rate of snow metamorphosis and changes in surface albedo using Centre d'Etudes de la Neige (CROCUS) formulas (Brun et al., 1992; Gallée et al., 2001; Fettweis et al., 2013).

A known issue with MAR when coupled with SISVAT is its neglection of the effects of feedbacks caused by ice sheet thinning over extended timescales (Fettweis et al., 2013). For example, when ice thins and resides at lower elevations it becomes more susceptible to melting (Helsen et al., 2012). Fortunately, this feedback is known to have limited effects over time periods of less than 100 years (Fettweis et al., 2013).

2.9.2.2. MAR validation:

Surface mass balance (SMB) and melt extent validations provide an idea of how well MAR predicts surface runoff. In order to validate SMB a comparison of model outputs has been made with 246 ice core accumulation measurements from the accumulation zone from 1999, 2001 and 2009 (Bales et al., 2001, 2009; Ohmura et al., 1999). MAR validation values are taken from the average of the four nearest grid cells to each observation (Fettweis et al., 2017).

A comparison is also made with the MACHGUTH16 GrIS SMB database (Machguth et al., 2016), which comprises of 1616 records and is derived using a multitude of in-situ measurements (Fettweis et al., 2017). MAR simulations are corrected for as a function of elevation difference and only MACHGUTH16 measurements within 500 m elevation difference of the MAR gridded output are used for validation (Fettweis et al., 2017).

Model validation results are also compared with the BOX13 model (Box, 2013a, 2013b), which also models changes in SMB (Fettweis et al., 2017).

Finally, melt extent simulations have been validated using brightness temperatures from horizontal polarisation K-band measurements from the Scanning Multi-channel Microwave Radiometer (SMMR, 1979-1987) and the Special Sensor Microwave/Imager (SMM/I, 1988-2010) (Fettweis et al., 2017).

Validation proves that MAR is suitable for providing runoff data. Ice core accumulation measurements show a positive correlation of 0.91 with simulations and an RMSE of just 8% (Fettweis et al., 2017). A strong positive correlation of 0.93 is also shown with the MACHGUTH16 database, however the RMSE here is 46% (Fettweis et al., 2017). Finally, MAR shows a strong positive correlation of 0.93 with satellite-derived melt data and an RMSE of just 2.8% (Fettweis et al., 2017).

MAR also shows better validation results than the BOX13 model, further enhancing its suitability (Fettweis et al., 2017). The BOX13 SMB model shows a correlation of 0.84 with the MACHGUTH16 database and an RMSE of 68%, whereas it shows a correlation of 0.92 with ice core accumulation measurements and an RMSE of 8% (Fettweis et al., 2017).

2.9.3. Regional Atmospheric Climate Model-2:

2.9.3.1. Model description:

The polar version of RACMO used here has ice sheet specific adaptations (Noël et al., 2018). The model uses a dynamical core acquired from the High Resolution Limited Area Model (HIRLAM) (Unden et al., 2002) and acquires its physics package from the CY33rl produced by the European Centre for Medium-Range Weather Forecasts Integrated Forecast System (ECMWF, 2008).

To accurately predict runoff volumes the model simulates water percolation, retention, melt and refreezing using a multilayer snow module (Ettema et al., 2010; Noël et al., 2018).

Surface albedo is predicted using the average lowest 5% albedo values acquired from the MODIS albedo product from 2000 to 2015 (Noël et al., 2016). Finally, the model also accounts for sublimation and snow drift (Lenaerts et al., 2012).

Here, an adaptation of RACMO2.3p2 is used, whereby it has been statistically downscaled from 11 km to 1 km resolution (Noël et al., 2016, 2018). The process of downscaling is as follows (Noël et al., 2016):

- The Greenland Ice Mapping Project (GIMP) DEM (90m resolution) (Howat et al., 2014) is aggregated to 1km grid cell size
- Using a local regression of SMB components with elevation, an elevation correction is applied on a 1 km scale
- The elevation correction is only applied to components that correlate strongly with elevation. These include: melt, runoff and sublimation

2.9.3.2. RACMO2.3p2 validation:

The validation of RACMO2.3p2 regarding meteorological records is beyond the scope of this report. Further information on this can be found in Noël et al (2018). Here, validation of SMB simulations are focused on. In order to validate SMB, a comparison is made between model outputs and in-situ measurements. 1073 in-situ SMB measurements are made at 213 stake sites in the ablation zone (Machguth et al., 2016) and 182 measurements are made using a combination of snow pits and airborne radar in the accumulation zone (Bales et al., 2001, 2009; Overly et al., 2016).

In the accumulation zone, the grid cell closest to that of the in-situ observation location is used for comparison (Noël et al., 2018). In the ablation zone, however, a neighbourhood of nine grid cells is examined and the cell with the altitude nearest that of the in-situ measurement is used for comparison to reduce altitudinal bias (Noël et al., 2018). Any in-situ measurements with an altitudinal difference greater than 100 m by comparison to the model output are disregarded (Noël et al., 2018).

The 11 km model produces an ice sheet wide SMB bias and RMSE of -22 and 72 mm w.e. yr^{-1}, respectively (Noël et al., 2018). However, this is primarily caused by incorrectly modelled precipitation in the southeast (Noël et al., 2018). When validation in the southeast is excluded bias and RMSE fall to -7 and 49 mm w.e. yr^{-1}, respectively (Noël et al., 2018).

Ablation zone 11 km SMB simulations show a large bias and RMSE of 1.33 and 0.60 m w.e. yr^{-1}, respectively (Noël et al., 2018). Furthermore, just 42% of observed variance is explained by the model output (Noël et al., 2018). This is likely due to the complex topography and small scale turbulent fluxes in this region (Noël et al., 2018), suggesting that further downscaling is required for the model to be useful for predicting runoff in peripheral regions such as the one studied here.

The 11 km simulated SMB of the accumulation zone shows slightly better agreement with in-situ measurements producing a bias, RMSE and R^2 value of -21.8 mm w.e. yr^{-1}, 71.1 mm w.e. yr^{-1} and 0.85, respectively (Noël et al., 2018).

Finally, 1 km statistically downscaled simulations show much better agreement with in-situ measurements in the ablation zone where bias and RMSE are reduced by 480 and 460 mm w.e. yr^{-1}, respectively (Noël et al., 2018). This suggests that the 1 km product is more suitable for modelling runoff in this study, as the region of interest is located on the periphery of the GrIS.

2.10. Data analysis:

2.10.1. Simple linear regression:

Velocity and runoff data used here are exported from MATLAB in '.csv' format. All simple linear regressions (velocity with time and velocity with antecedent runoff) are carried out using the 'lm' function of the R programming language (appendix 5.5.2.1 – R Project, 2017a). The significance of the observed relationships is also calculated.

For regressions between velocity and antecedent runoff production (appendix 5.5.2.1 – script section 3), the number of years over which runoff data is aggregated prior to the velocity year extends from 1 to 5 (both including and excluding the year of the velocity observation) to test whether the number of antecedent runoff years has an effect on the amount of ice motion that can be explained (e.g. Tedstone et al., 2015). For the regression of antecedent runoff production with average annual velocities, the null and alternative hypotheses are as follows:

- H_0: There is no statistically significant relationship between antecedent runoff and average annual velocity
- H_1: There is a statistically significant relationship between antecedent runoff and average annual velocity

In order to carry out the regression between antecedent runoff production and average annual velocities, the years in which velocities are recorded are rounded to their nearest integer values for comparison with corresponding runoff observations, whose associated measure of time is integer years.

2.10.2. Mann-Whitney-Wilcoxon tests and segmented linear regressions:

The purpose of a Mann-Whitney-Wilcoxon (MWW) test is to understand whether samples are derived from the same underlying population (LaMorte, 2017). This is useful for highlighting time periods over which both ice sheet velocities and runoff production may show differing temporal characteristics. Here, the method of Tedstone et al (2015) is roughly followed, whereby MWW tests are carried out in partnership with segmented linear regressions (appendices 5.1 – 5.3) to predict the year in which deceleration and runoff production increase are initiated. The MWW test is used rather than a t-test, due to the fact

that ice sheet velocities tend not to follow a normal distribution due to the presence of outliers (Tedstone et al., 2015; Burgess et al., 2013; Dehecq et al., 2015).

2.10.2.1. Velocity data:

For velocity time series data, a number of MWW tests are carried out to find the year in which population samples begin to show a statistically significant difference (appendix 5.5.2.1 – script section 2). This is assumed to be indicative of deceleration onset. Following this, a series of segmented linear regressions are carried out, with predicted break dates spread either side of the predicted deceleration onset year (Tedstone et al., 2015). A further break date is applied in 2013 to account for the visibly different trend witnessed beyond this point. The break date of the segmented linear regression with the lowest residual standard error is then used in combination with the predicted year of deceleration onset from the MWW tests to estimate the year in which deceleration begins.

A limitation here is that the final velocity time series has a number of missing values, making it difficult to pinpoint the exact point at which deceleration begins.

2.10.2.2. Runoff data:

To understand patterns in runoff data, segmented linear regressions are carried out prior to MWW tests (appendix 5.5.2.1 – script section 4). Here, it is predicted that runoff data can be divided into three periods of distinctive behaviour. Therefore, all possible break point combinations are cycled through, to find that which provides the lowest residual standard error. Following this, a series of MWW tests are carried out that roughly use each regression line as a population sample, consistent with Tedstone et al (2015). Finally, break dates are predicted based upon the location of those that provide the lowest residual standard error in the segmented linear regressions and that satisfy MWW tests to a significant level.

A limitation here is that significant difference is unlikely to be found between population samples using a MWW test if at least one of the samples being tested is small in size (Forero, 2013).

2.10.2.3. Carrying out a Mann-Whitney-Wilcoxon test:

In order to carry out a MWW test, separate population samples are combined while information is retained on their initial sample membership (LaMorte, 2017). Following this, the population members are ranked from lowest to highest (LaMorte, 2017). These data are then used to calculate the test statistic in the following equations:

$$U_1 = n_1 n_2 + \frac{n_1(n_1+1)}{2} - R_1$$ *Equation 8. (LaMorte, 2017)*

$$U_2 = n_1 n_2 + \frac{n_2(n_2+1)}{2} - R_2$$ *Equation 9. (LaMorte, 2017)*

where the lower of U_1 and U_2 is the test statistic, n is the number of observations in each population sample and R is the sum of ranks of each sample. Because the MWW is carried out in the R programming language using the 'wilcox.test' function (appendix 5.5.2.1), the test statistic is then used to provide a significance level rather than having to compare with critical values in lookup tables (LaMorte, 2017; R Project, 2017b).

The hypotheses of MWW tests are as follows:

- H_0: Population samples show no difference to a statistically significant level and are therefore considered equal
- H_1: Population samples show difference to a statistically significant level and are therefore considered not equal

2.10.2.4. Carrying out a segmented linear regression:

Segmented linear regressions were carried out using the 'segmented' function of the segmented package of the R programming language (appendix 5.5.2.1 – Muggeo, 2017). The arguments taken here are: the initial linear regression model, the variable upon which breaks are being tested for and the estimated locations of break points (Muggeo, 2017).

This function outputs: the R^2 value associated with the segmented linear regression, the residual standard error, the equations and significance associated with each part of the segmented regression and the overall significance of the regression.

2.11. Impact of changing ice thickness and surface slope:

2.11.1. Reason for analysis:

Ice sheet geometries are continually modified as a result of dynamic change and mass wastage, leading to changes in driving stresses (Tedstone et al., 2015). For example, changes in basal shear stress (τ_b) can be predicted using measurements of ice thickness and surface slope (Davies, 2017). This is shown in the following equation:

$$\tau_b = \rho_i g h \sin \alpha_s \qquad \textit{Equation 10. (Davies, 2017)}$$

where ρ_i is ice density (~917 kg m^{-3}), g is gravitational acceleration of ice (9.81 m s^{-1}), h is ice thickness and α_s is the surface slope (in degrees) (Davies, 2017). This shows that (with all other parameters held constant) as ice thickness or surface slope increase in value, so does basal shear stress.

Strain is the term used to describe the change in object shape, resulting from an applied stress (Davies, 2017). Strain rates (ε) experienced by glacial ice increase in unison with basal shear stress, therefore as basal shear stress increases, so does deformation and flow (Davies, 2017). This is shown by Glen's Flow Law:

$$\varepsilon = AT^n \qquad \textit{Equation 11. (Glen, 1958)}$$

where A is a constant dependent on crystal orientation, the temperature of ice and ice debris content; $n = 3$ and T is basal shear stress (Glen, 1958).

Tedstone et al (2015) test whether observed velocity patterns are likely to result from changing ice sheet geometries using a model-based approach. The model predicts that from 0 to 5 km inland up to 100% of deceleration can be explained by geometric changes, however between 10 and 50 km inland a maximum of 33% of deceleration can be explained (Tedstone et al., 2015).

Here, due to time constraints, a much more basic assessment is carried out whereby tests for significant difference in ice sheet surface slope and ice sheet thickness over the period 1985 to 2007 are undertaken. The results from this assessment are used to infer whether future work may be required to account for the effects of geometric changes.

2.11.2. Ice sheet surface and bed topography data:

Ice sheet surface elevation data is obtained from the 1985 aeroDEM (Korsgaard et al et., 2016) and the 2007 GIMP DEM (Howat et al., 2014). Both these datasets were primarily derived using photogrammetric techniques, therefore no correction was required to account for different acquisition methods (e.g. subsurface returns from radar acquired data). To derive ice sheet thickness, recently derived BedmachineV3 bed topography data is subtracted from the ice sheet surface elevation data (Morlighem et al., 2017). All elevation and bed data used are relative to the WGS1984 ellipsoid to ensure consistent results are produced.

The aeroDEM has a horizontal accuracy of 10 m and vertical accuracy of 6 m at the 1σ confidence interval (Korsgaard et al., 2016), whereas the GIMP DEM has a quoted on-ice vertical root mean square difference of ±8.5 m relative to ICESat data (Howat et al., 2014).

As in Tedstone et al (2015), analysis is carried out using data extracted along a transect (figure 8). Here an extended version of the transect 'Far south' is used, due to the fact that it shows a clear and consistent pattern of deceleration (research paper – figure 6). Data are plotted using a less complex version of the 'transect plotter' script (section 5.5.1.1).

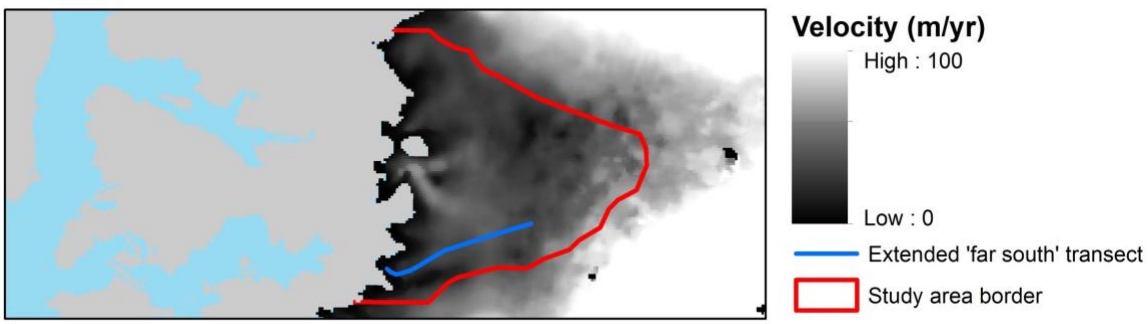

Figure 8: Map showing location of extended 'far south' transect, along which ice thickness and surface elevation profiles are extracted.

2.11.3. Statistical tests:

2.11.3.1. Surface slope differences:

To test for significant differences in surface slope, an analysis of covariance (ANCOVA) test is carried out in the R programming language (appendix 5.5.2.2). This compares the gradients of regression lines (i.e. average slopes) from each transect (McDonald, 2014). When undertaking this test, 'elevation' is used as the dependent variable, 'distance' as the independent variable and 'DEM source' as the factor used to split observations into categorical groups. It is assumed that observations are independent of one another and that standardised residuals are approximately normally distributed, however ANCOVA is robust against deviations from the normal distribution under large sample sizes (Laerd Statistics, 2017, Minitab, 2015).

The hypotheses for the ANCOVA test carried out here are as follows:

- H_0: The regression line gradients for surface elevation data obtained in 1985 and 2007 show no statistically significant difference
- H_1: The regression line gradients for surface elevation data obtained in 1985 and 2007 show statistically significant difference

2.11.3.2. Ice thickness differences:

To test for significant differences in ice thickness, an extension of the ANCOVA test is used. First, the previously described test for statistically significant difference in regression line gradients is undertaken (McDonald, 2014). Following this, if there is insufficient evidence to reject the null hypothesis, a further test is carried out to see whether there is a statistically significant difference in the Y intercepts of regression lines, and therefore magnitude of observations in each DEM acquisition year (McDonald, 2014).

The hypotheses for this extension of the ANCOVA test are as follows:

- H_0: The Y intercept of the aeroDEM transect regression line shows no statistically significant difference to that of the GIMP DEM
- H_1: The Y intercept of the aeroDEM transect regression line shows statistically significant difference to that of the GIMP DEM

A limitation associated with using ANCOVA tests to understand geometric change, is that geometric changes sufficient to alter driving stresses and therefore velocities may be considered statistically insignificant if they are small, relative to the magnitude of data being compared. Therefore, these tests are not seen as conclusive if visual examination of profiles suggests geometric change sufficient to alter driving stresses has occurred.

It should also be considered that the GIMP DEM is not ideal for this analysis due to its 2007 acquisition date. Given a further 10-years of change, the ANCOVA test outcomes may change.

2.12. Transects:

Flowline transects are used in this study to understand how velocity change patterns may be distributed across the study region. They are derived by examining velocity patterns presented in velocity maps and aerial imagery of the study area.

To create each transect, velocity GeoTIFF files were imported into ESRI's ArcGIS. Following this, velocity profiles were extracted using the 'Extract Multi Values to Points' tool, whereby pixel values for each GeoTIFF were extracted to points that had been generated every 100 metres along transects. These points were created using the 'Generate Points Along Lines' tool. Finally, attribute tables were exported and converted to '.csv' format to be plotted using a Python script (appendix 5.5.1.1).

The Python script applies a Savitzky-Golay polynomial filter to annual data for each transect to reduce noise and highlight genuine fluctuations in velocity profiles (SciPy Cookbook, 2012). This technique is useful as it preserves the initial shape of the profiles.

3. Extended results:

As mentioned in section 2.7.4, the initial decision to use different bands for different Landsat missions led to inconsistent time series results. This section will outline how this conclusion was reached, before presenting performance indicator results to add validity to trends presented in the research paper.

3.1. Results under initial parameters:

Upon initial inspection of a time series produced using a variety of initial image resolutions, Landsat 7 ETM+ and Landsat 8 OLI data seemed to match the trend observed by Tedstone et al (2015), whereby deceleration occurred beyond 2002. However, an increasing trend was shown from 1985 to 2001 and Landsat 5 TM derived velocities were slower than those recorded from 1999 to 2003 (figure 9).

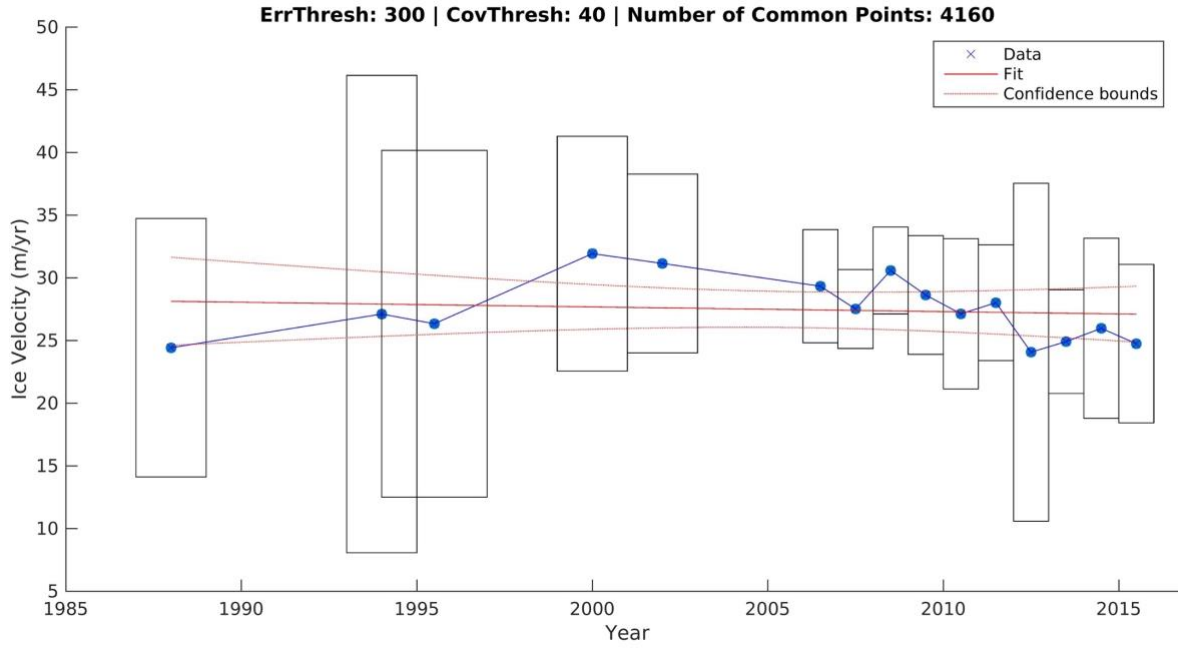

Figure 9: Graph showing how velocities increased from 1985 to ~2001 when PCA is carried out on bands two and three for Landsat 5 TM data whilst the panchromatic band is used to derive Landsat 7 ETM+ and Landsat 8 OLI velocities. The error threshold is set to 300 m yr^{-1} to maximise the number of common points. Study site coverage threshold is 40%. Script for figure production supplied by Josh Williams.

3.1.1. Coregistration accuracy:

Coregistration accuracies of periods exhibiting visibly different velocity trends were tested to ensure that the observed trends were not a result of inaccuracy. Here, fusion was carried out over the periods 1987 to 1997, 1999 to 2003 and 2006 to 2016. Next, the median velocities measured in stable areas for each period were differenced. Figure 10 shows that that there is minimal difference between the coregistration accuracy. For example, coregistration accuracy shows a maximum median difference of -0.982 m yr^{-1} and a maximum mean difference of -1.218 m yr^{-1} when velocities from the period 1987 to 1997 and 2006 to 2016 are compared.

To ensure that coregistration could not be further improved, median coregistration was also carried out on X and Y component planes of final fused velocity products. This yielded a maximum improvement of ~0.02 m yr^{-1} for the 1987 to 1997 product and therefore was not deemed necessary. Finally, when converting velocity values of stable areas to integers and using the modal value of component planes for coregistration, no improvement was found as modal integer values were 0 m yr^{-1} in both X and Y directions. This helped prove that accurate coregistration had been achieved.

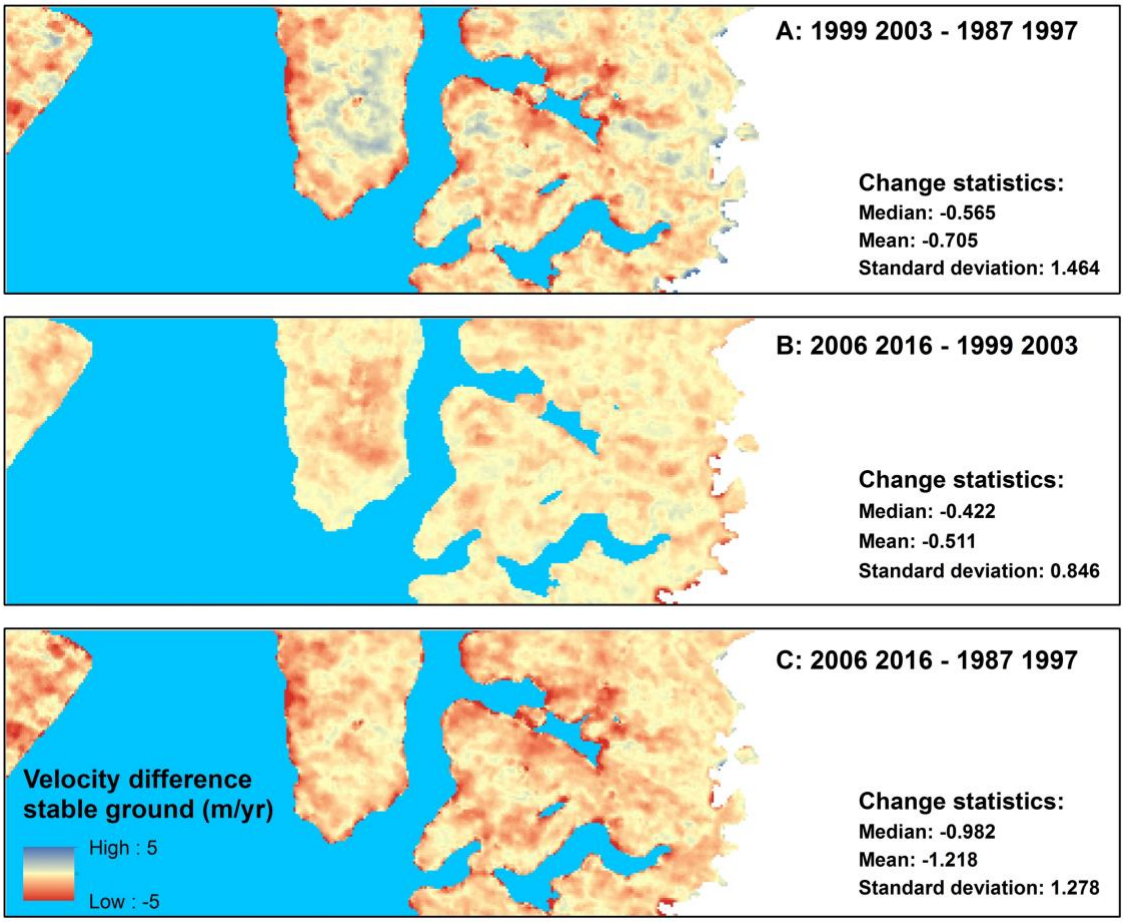

Figure 10: Maps showing velocity differences between stable areas, illustrating coregistration accuracy under initial parameter choices. A – difference between 1987-1997 and 1999-2003, B – difference between 1999-2003 and 2006-2016, C – difference between 1987-1997 and 2006-2016. Change statistics show median, mean and standard deviation of difference. In the creation of these maps, older velocities were subtracted from the most recent.

3.1.2. Baseline comparison:

The first indication that the use of different spectral band combinations for different Landsat missions may be causing the observed trend to stray from that observed by Tedstone et al (2015) was provided by a comparison of yearly derived velocities with a baseline velocity derived by merging all available feature tracking results together (figure 11).

Figure 11 illustrates that Landsat 5 TM derived difference maps show an inconsistent difference pattern, relative to other Landsat missions, when compared to baseline values. This is attributed to that fact that the baseline is primarily influenced by Landsat 7 ETM+ and Landsat 8 OLI data. Therefore, it is feasible that the different patterns observed in Landsat 5 TM derived maps are caused by different reference and search image characteristics, i.e. coarser spatial resolutions.

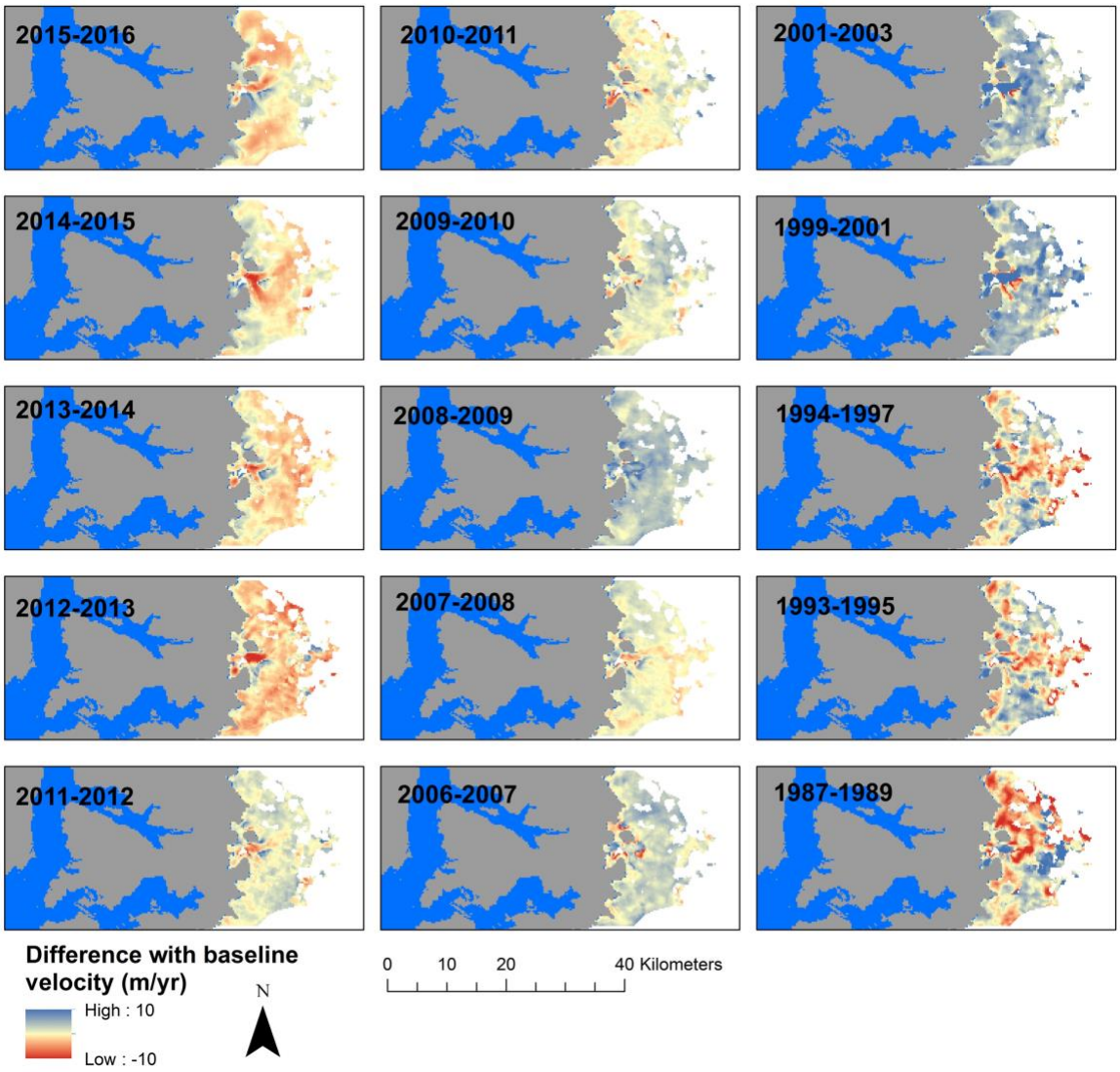

Figure 11: Comparison of yearly derived velocities with median baseline derived over the period 1985 to 2016, under initial parameter choices. Negative values are below the baseline and positive values are above. Velocity maps are clipped to common areas, but do not exclude pixels above the error threshold of 60 m yr^{-1}.

3.1.3. Transect pattern examination:

As a further line of enquiry, a transect was produced using panchromatic band data for Landsats 7 and 8 and bands two and three PCA data for Landsat 5, on the 'Central north' profile (figure 12). Here, there is a clear mismatch between velocity profile patterns beyond ~1000 m from the transect origin. This is likely because the location of maximum similarity within the search window changes for data of different resolutions, due to the fact that a less detailed pattern is observed in the reference window under a coarser resolution.

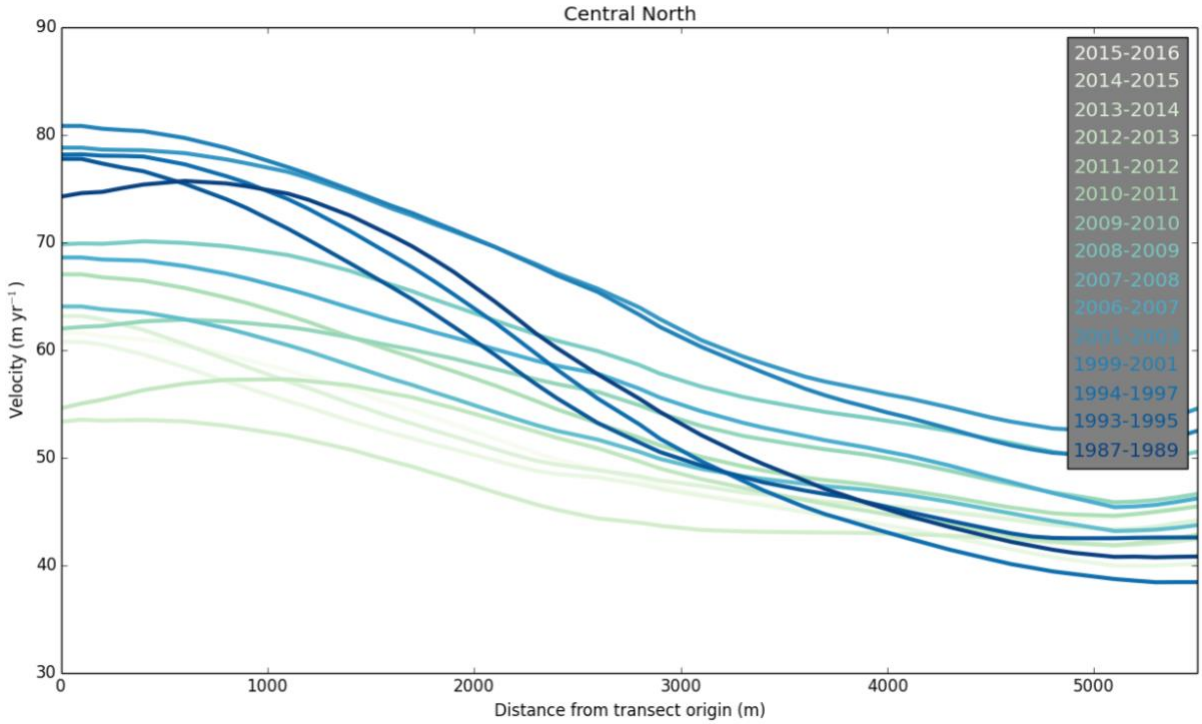

Figure 12: Velocity profiles taken from transect 'Central North' (research paper – figure 1) under initial feature tracking parameters (section 2.7.4.1 – table 2). No error threshold is applied but a Savitzky-Golay filter is applied to all profiles (SciPy Cookbook, 2012). *Used to help understand erroneous time series produced by initial parameter choices.*

3.2. Final parameter choices:

As a final test, to help understand whether velocities produced using Landsat 5 TM data were systematically different, feature tracking was carried out on the first PC of bands two and three of Landsat 7 ETM+ SLC-on imagery.

This lowered measured velocities and started to show a trend more consistent with that of Tedstone et al (2015), i.e. no increase in velocity from 1985 to 2003 (figure 13). Therefore, feature tracking as well as all associated pre- and post-processing was re-run to derive a time series where velocities were measured using the first PC of bands two and three (section 2.7.4.2 – table 3), consistent with Tedstone et al (2015).

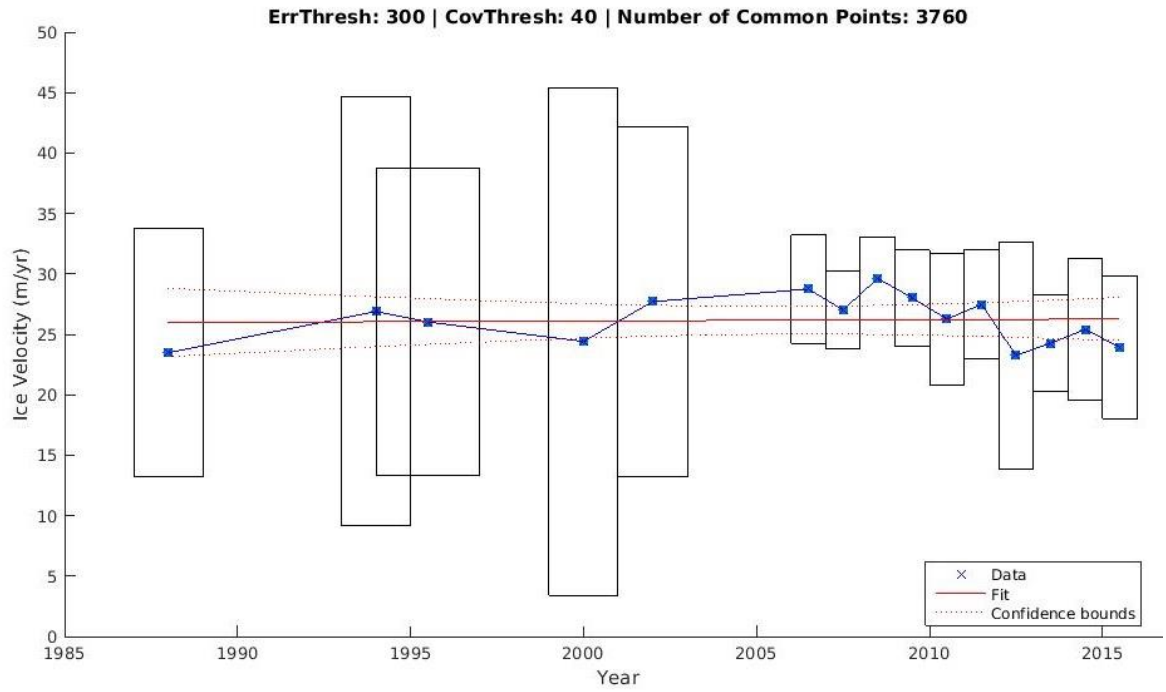

Figure 13: Time series showing the experimental outcome of performing PCA based feature tracking with bands two and three for Landsat 5 TM and Landsat 7 ETM+ SLC-on data. The panchromatic band is used for Landsat 7 ETM+ SLC-off and Landsat 8 OLI data. The error threshold is set to 300 m yr^{-1} to maximise the number of common points. Study site coverage threshold is 40%. Script for figure production supplied by Josh Williams.

3.2.1. Coregistration accuracy:

As with the incorrect parameter choices, median velocities measured in stable areas were differenced. Here, merges created for the periods 1985 to 1997, 1999 to 2003 and 2006 to 2016 were differenced to ensure that changing coregistration accuracies did not significantly affect the trend presented.

When comparing 1999 to 2003 with 1985 to 1997 (figure 14), a maximum mean reduction in coregistration accuracy of 0.407 m yr^{-1} is observed in 1999 to 2003. This is of an insufficient magnitude to generate artificial trends.

When comparing 1985 to 1997 with 2006 to 2016, it is found that the mean maximum difference in coregistration accuracy of -0.994 m yr^{-1} (i.e. a reduction in the velocity of stable ground) is sufficient to weaken the final measured trend (an overall reduction in velocity of -1.4 m yr^{-1}). The median difference value of -0.770 m yr^{-1}, however, is less influenced by the presence of outliers and is therefore more likely to accurately represent the difference in coregistration accuracy. Therefore, coregistration accuracy may weaken, but not eliminate the trends presented in this study.

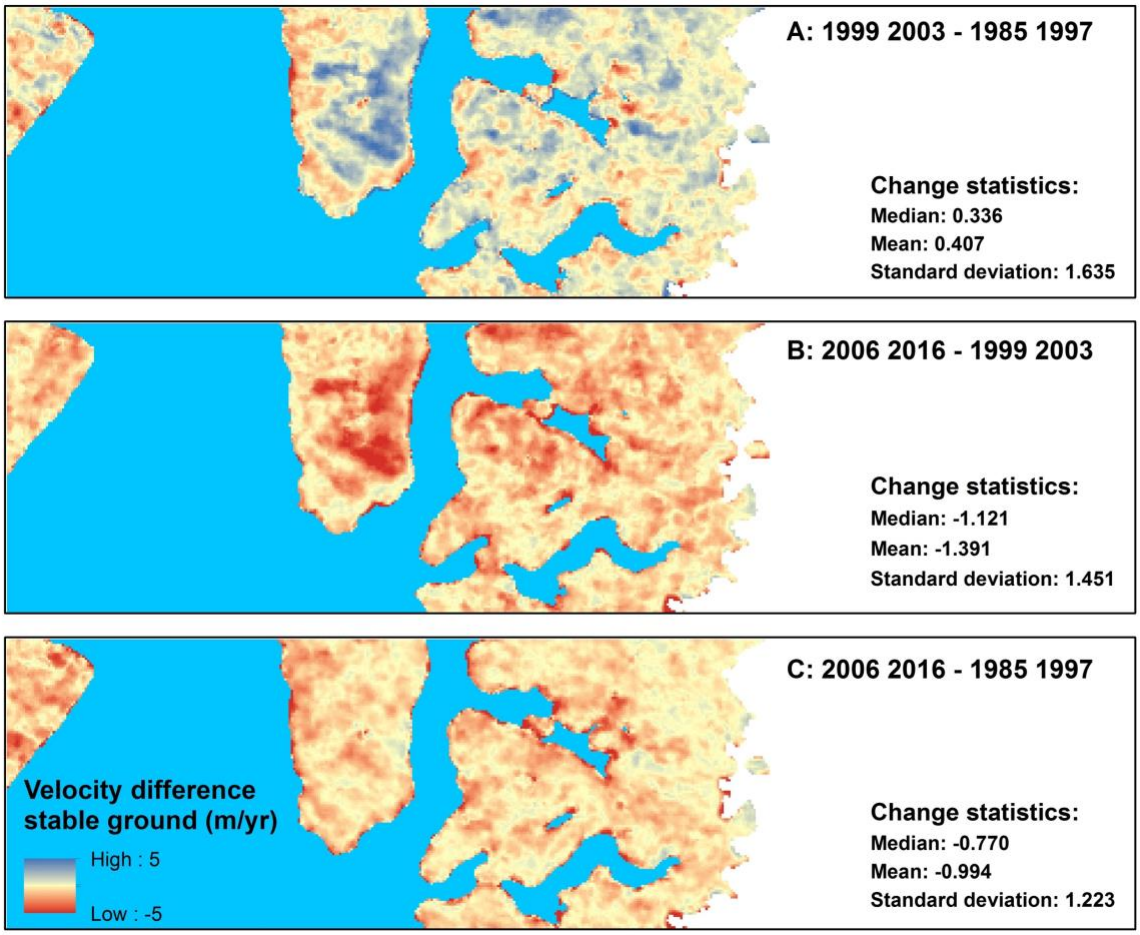

Figure 14: Maps showing velocity differences between stable areas, illustrating coregistration accuracy under final parameter choices. A – difference between 1985-1997 and 1999-2003, B – difference between 1999-2003 and 2006-2016, C – difference between 1985-1997 and 2006-2016. Change statistics show median, mean and standard deviation of difference. In the creation of these maps, older velocities were subtracted from the most recent.

3.3. Performance indicators of final results:

3.3.1. Velocity maps:

Figure 15 indicates that Landsat 8 OLI data performed best when feature tracking was carried out, as velocity maps derived using these data have the most comprehensive spatial coverage. This is a result of 12-bit radiometric resolution, as opposed to 8-bit employed by the other sensors (NASA, 2018b), and due to the greater availability of image pairs. The advent of 12-bit radiometric resolution increases the coverage of velocity maps as it extends the grey-scale range that can be measured, reducing saturation of trackable features.

Figure 15 also provides a rough idea as to the quality of coregistration undertaken on each velocity map. For example, Landsat 8 OLI data coregistration is proven to be of excellent quality, due to the fact that velocity observations of stable ground are scarcely visible. Velocity maps exhibiting particularly poor coregistration accuracy include those of: 2010-2011, 1993-1995 and 1987-1989.

Finally, figure 15 also shows that Landsat 5 is limiting in terms of common points.

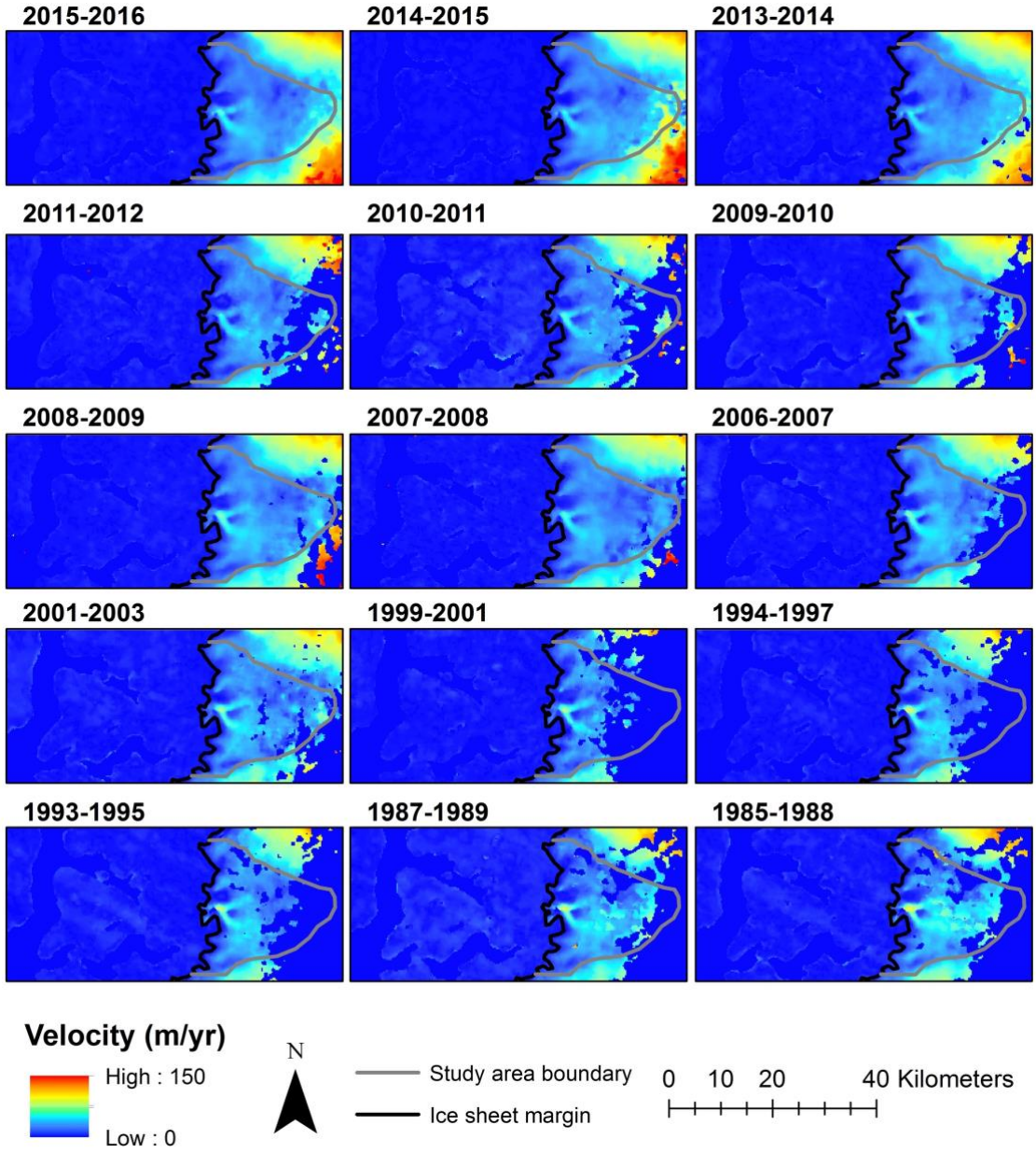

Figure 15: Velocity maps corresponding to each median measurement presented in the final time series (research paper – figure 4). No error threshold is employed. Extent is not limited to common points.

3.3.2. Median absolute deviation:

Upon inspection, the MAD of most scenes appears roughly consistent, with some deviations from this pattern (figure 16). For Landsat 8 OLI derived maps, MAD increases inland in 2015-2016 and 2014-2015. This may be a result of short-term behavioural change of neighbouring marine terminating glaciers, or due to the large volume of data used to derive these maps.

Landsat 5 TM data shows high MAD values across fused maps. Particularly in 1987-1989 and 1985-1988. The high MAD values follow a horizontal banding pattern. These banding patterns are likely a result of known artefacts present in Landsat 5 TM data (USGS, 2018g).

Finally, unsurprisingly, in most scenes a high MAD appears to be associated with areas where high flow variability would be expected, i.e. areas exhibiting highest velocities.

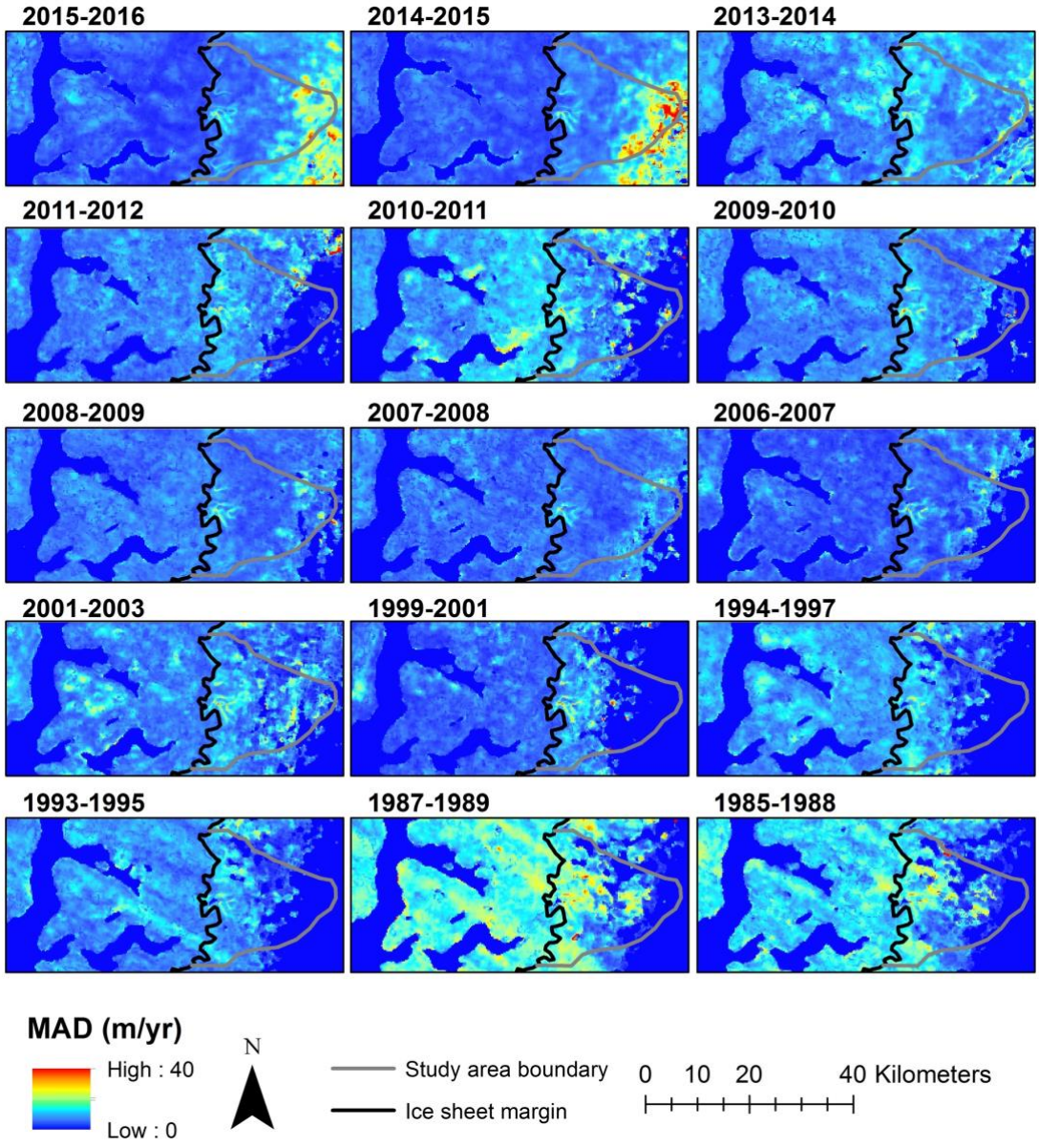

Figure 16: MAD maps corresponding to each median measurement presented in the final time series (research paper – figure 4). No error threshold is employed. Extent is not limited to common points.

3.3.3. Number of points:

Velocity maps exhibiting the highest number of points are closely associated with the number of image pairs used to derive them (figure 17). Landsat 8 OLI derived maps also exhibit a greater number of points inland, due to the superior radiometric resolution of the OLI sensor (NASA, 2018b).

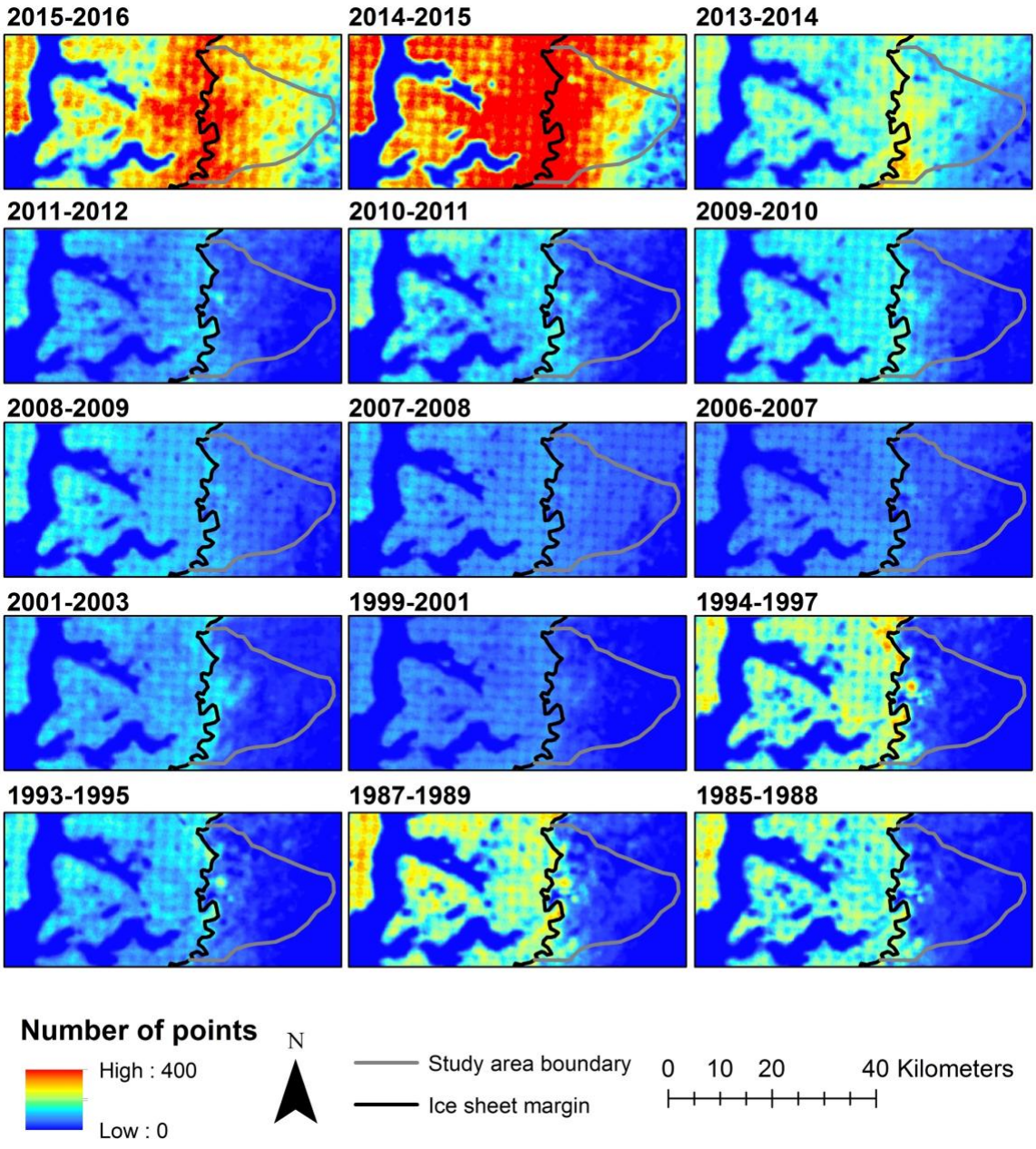

Figure 17: Number of points maps corresponding to each median measurement presented in the final time series (research paper – figure 4). No error threshold is employed. Extent is not limited to common points.

3.3.4. Coherence:

Poor coherence associated with Landsat 8 OLI data is likely a result of the number of image pairs used to derive fused scenes, relative to other sensors (figure 18), as this offers greater opportunity for directional flow variability to be witnessed.

Coherence measurements also allude to velocity maps which have been derived using poor quality data. 1987-1989 is a particularly good example of this.

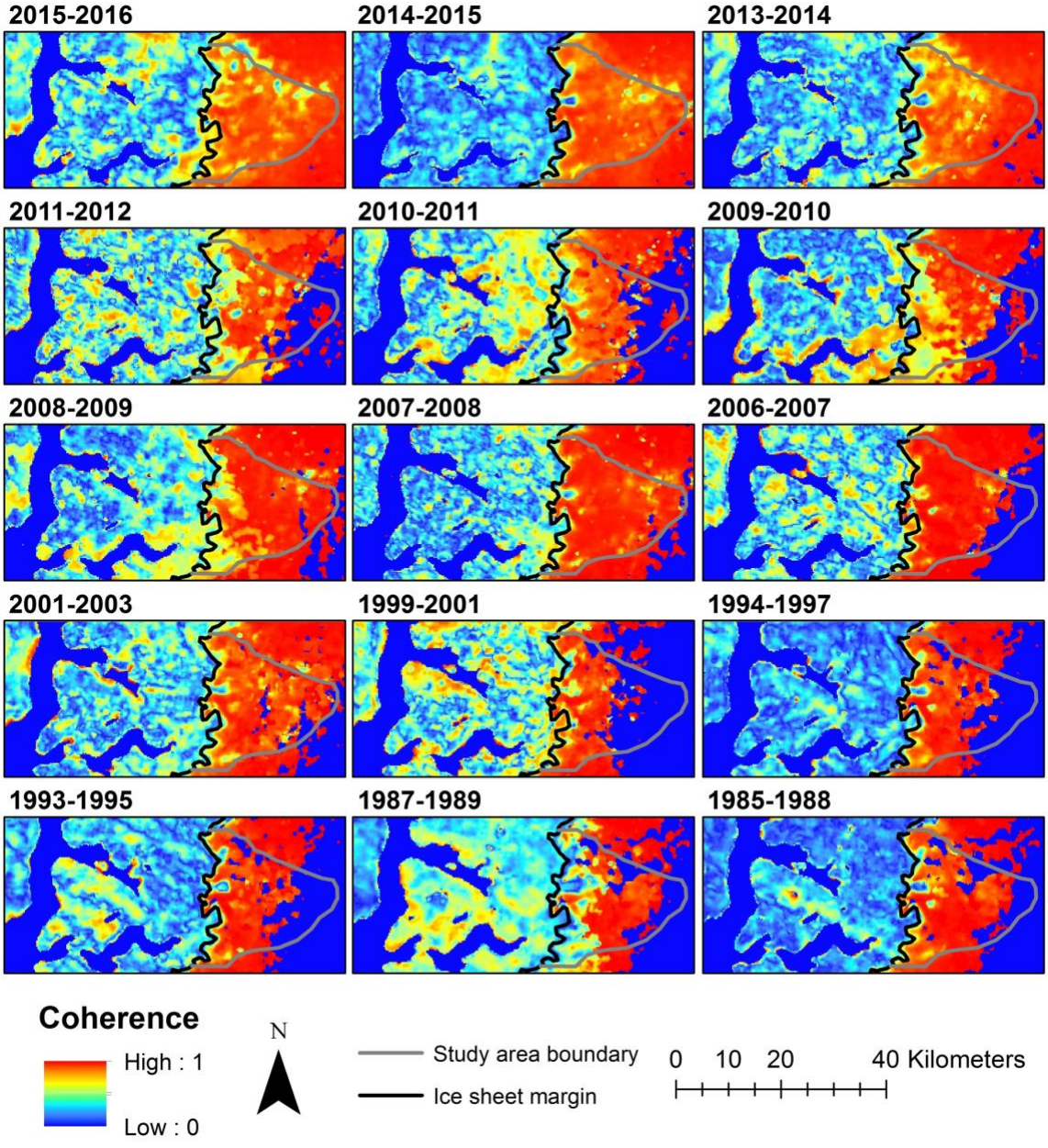

Figure 18: Coherence maps corresponding to each median measurement presented in the final time series (research paper – figure 4). No error threshold is employed. Extent is not limited to common points.

3.3.5. MeASUREs comparison:

When comparing data derived in this study with that of MeASUREs over the period 2001 to 2013 (figure 19) it is found that although velocity magnitudes differ, the general pattern is similar. For example, both datasets observe high velocities circa 2001, followed by a decrease up until 2008. Following this, both datasets observe two years of velocity increase followed by low velocities circa 2013. In summary, this helps to ratify observations presented in the associated research paper and increases confidence that observed patterns are genuine.

MeASUREs data show no significant trend from 2001 to 2013 (-0.40 m yr^{-1}, R^2 = 0.35, p = 0.16).

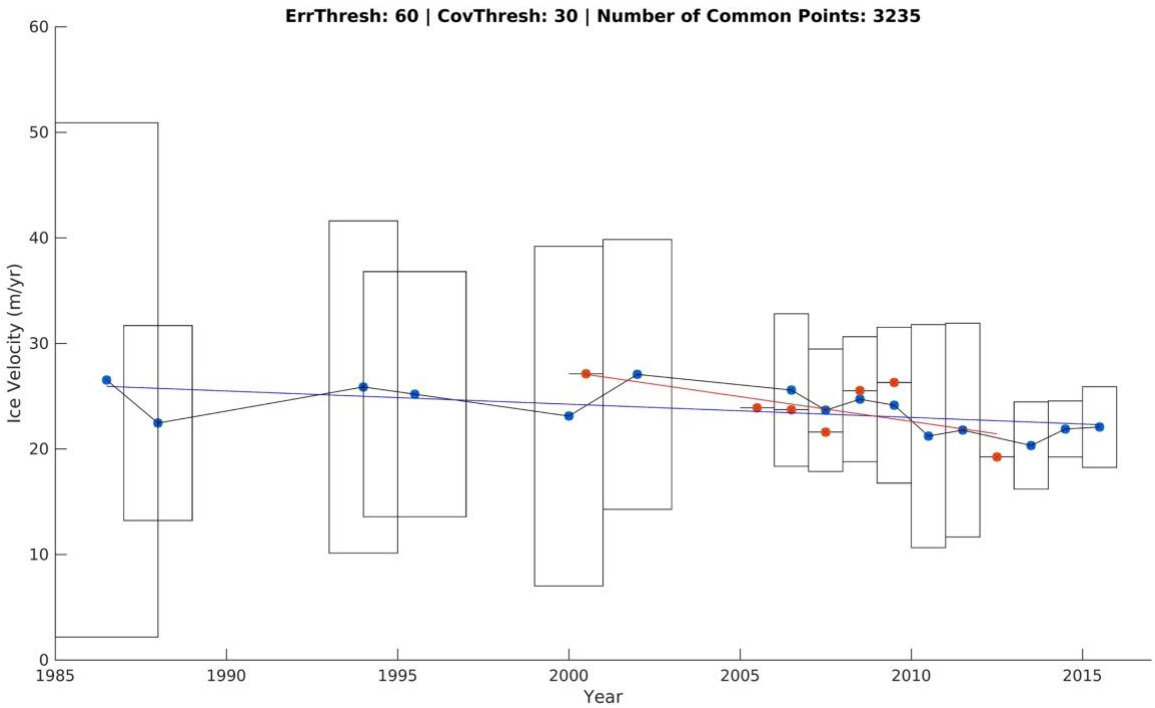

Figure 19: Final time series created using data collected in this study (blue data points and regression line) and time series created using MeASUREs data for the period 2001 to 2013 (Joughin, 2010, 2017) (orange data points and regression line). All error bars correspond to data collected in this study. Error and study site coverage thresholds are 60 m yr^{-1} and 30%, respectively. The rectangles surrounding each observation represent error in the Y direction and temporal coverage in the X direction. Script for figure production supplied by Josh Williams.

Finally, when comparing data derived in this study with that of MeASUREs over the period 2014 to 2016, similar increasing patterns of different magnitudes are observed (figure 20). Again, this helps to ratify findings.

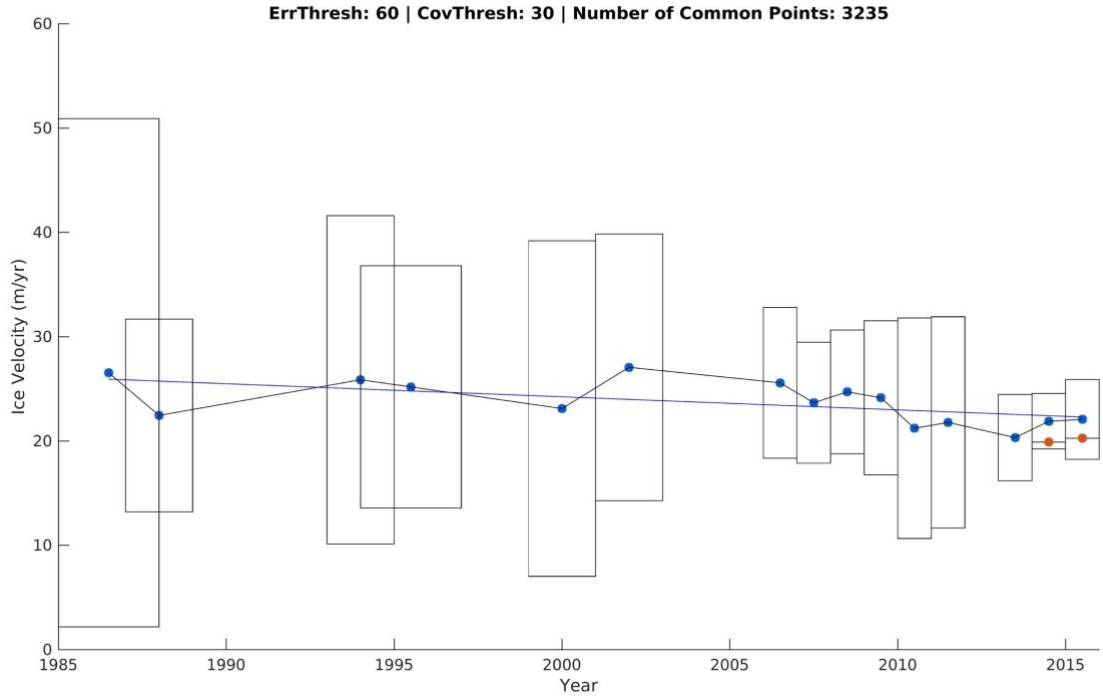

Figure 20: Final time series created using data collected in this study (blue data points and regression line) and time series created using MeASUREs data for the period 2014 to 2016 (Joughin, 2010, 2017) (orange data points). All error bars correspond to data collected in this study. Error and study site coverage thresholds are 60 m yr^{-1} and 30%, respectively. The rectangles surrounding each observation represent error in the Y direction and temporal coverage in the X direction. Script for figure production supplied by Josh Williams.

4. References:

Ahn, Y. and Howat, I. (2011). Efficient Automated Glacier Surface Velocity Measurement From Repeat Images Using Multi-Image/Multichip and Null Exclusion Feature Tracking. IEEE Transactions on Geoscience and Remote Sensing, 49(8), pp.2838-2846.

Bales, R., Guo, Q., Shen, D., McConnell, J., Du, G., Burkhart, J., Spikes, V., Hanna, E. and Cappelen, J. (2009). Annual accumulation for Greenland updated using ice core data developed during 2000–2006 and analysis of daily coastal meteorological data. Journal of Geophysical Research, 114(D6).

Bales, R., McConnell, J., Mosley-Thompson, E. and Csatho, B. (2001). Accumulation over the Greenland ice sheet from historical and recent records. Journal of Geophysical Research: Atmospheres, 106(D24), pp.33813-33825.

Berthier, E., Raup, B. and Scambos, T. (2003). New velocity map and mass-balance estimate of Mertz Glacier, East Antarctica, derived from Landsat sequential imagery. Journal of Glaciology, 49(167), pp.503-511.

Box, J., Cressie, N., Bromwich, D., Jung, J., van den Broeke, M., van Angelen, J., Forster, R., Miège, C., Mosley-Thompson, E., Vinther, B. and McConnell, J. (2013a). Greenland Ice Sheet Mass Balance Reconstruction. Part I: Net Snow Accumulation (1600–2009). Journal of Climate, 26(11), pp.3919-3934.

Box, J. (2013b). Greenland Ice Sheet Mass Balance Reconstruction. Part II: Surface Mass Balance (1840–2010). Journal of Climate, 26(18), pp.6974-6989.

Brun, E., David, P., Sudul, M. and Brunot, G. (1992). A numerical model to simulate snow-cover stratigraphy for operational avalanche forecasting. Journal of Glaciology, 38(128), pp.13-22.

Burgess, E., Forster, R. and Larsen, C. (2013). Flow velocities of Alaskan glaciers. Nature Communications, 4.

Davies, B. (2017). Stress and Strain. [online] AntarcticGlaciers.org. Available at: http://www.antarcticglaciers.org/modern-glaciers/glacier-flow-2/glacier-flow-ii-stress-and-strain/ [Accessed 5 Jul. 2018].

Dehecq, A., Gourmelen, N. and Trouve, E. (2015). Deriving large-scale glacier velocities from a complete satellite archive: Application to the Pamir–Karakoram–Himalaya. Remote Sensing of Environment, 162, pp.55-66.

ECMWF (2008). IFS DOCUMENTATION – Cy33r1 PART IV: PHYSICAL PROCESSES. [online] Ecmwf.int. Available at: https://www.ecmwf.int/sites/default/files/elibrary/2009/9227-part-iv-physical-processes.pdf [Accessed 9 May 2018].

ENVEO (2017). ENVEO - Greenland Ice Velocity map from Sentinel-1. [online] Enveo.at. Available at: http://www.enveo.at/news/209-greenland-ice-velocity-map-from-sentinel-1 [Accessed 28 Feb. 2018].

ESA (2018). ESA - Online Dissemination - Homepage. [online] Landsat-ds.eo.esa.int. Available at: https://landsat-ds.eo.esa.int [Accessed 3 May 2018].

Ettema, J., van den Broeke, M., van Meijgaard, E., van de Berg, W., Box, J. and Steffen, K. (2010). Climate of the Greenland ice sheet using a high-resolution climate model – Part 1: Evaluation. The Cryosphere, 4(4), pp.511-527.

Fahnestock, M., Scambos, T., Moon, T., Gardner, A., Haran, T. and Klinger, M. (2016). Rapid large-area mapping of ice flow using Landsat 8. Remote Sensing of Environment, 185, pp.84-94.

Fettweis, X., Box, J., Agosta, C., Amory, C., Kittel, C., Lang, C., van As, D., Machguth, H. and Gallée, H. (2017). Reconstructions of the 1900–2015 Greenland ice sheet surface mass balance using the regional climate MAR model. The Cryosphere, 11(2), pp.1015-1033.

Fettweis, X., Franco, B., Tedesco, M., van Angelen, J., Lenaerts, J., van den Broeke, M. and Gallée, H. (2013). Estimating the Greenland ice sheet surface mass balance contribution to future sea level rise using the regional atmospheric climate model MAR. The Cryosphere, 7(2), pp.469-489.

Fitch, A., Kadyrov, A., Christmas, W. and Kittler, J. (2002). Orientation Correlation. Proceedings of the British Machine Vision Conference 2002.

Forero, L. (2013). Wilcoxon-Mann-Whitney test and a small sample size | Oxford Protein Informatics Group. [online] Blopig.com. Available at: http://www.blopig.com/blog/2013/10/wilcoxon-mann-whitney-test-and-a-small-sample-size/ [Accessed 9 May 2018].

Gallée, H. and Schayes, G. (1994). Development of a Three-Dimensional Meso-γ Primitive Equation Model: Katabatic Winds Simulation in the Area of Terra Nova Bay, Antarctica. Monthly Weather Review, 122, pp.671-685.

Gallée, H., Guyomarc'h, G. and Brun, E. (2001). Impact Of Snow Drift On The Antarctic Ice Sheet Surface Mass Balance: Possible Sensitivity To Snow-Surface Properties. Boundary-Layer Meteorology, 99(1), pp.1-19.

Glen, J. (1958). The flow law of ice: A discussion of the assumptions made in glacier theory, their experimental foundations and consequences. IASH, pp.171-183.

Gonzalez, R. and Woods, R. (2002). Digital image processing. 2nd ed. Upper Saddle River, N.J.: Prentice Hall.

Grinsted, A. (2015). templatematch.m - ImGRAFT. [online] Imgraft.glaciology.net. Available at: http://imgraft.glaciology.net/documentation/functions/templatematchm [Accessed 16 Jul. 2018].

Heid, T. and Kääb, A. (2012). Evaluation of existing image matching methods for deriving glacier surface displacements globally from optical satellite imagery. Remote Sensing of Environment, 118, pp.339-355.

Helsen, M., van de Wal, R., van den Broeke, M., van de Berg, W. and Oerlemans, J. (2012). Coupling of climate models and ice sheet models by surface mass balance gradients: application to the Greenland Ice Sheet. The Cryosphere, 6(2), pp.255-272.

Howat, I., Negrete, A. and Smith, B. (2014). The Greenland Ice Mapping Project (GIMP) land classification and surface elevation data sets. The Cryosphere, 8(4), pp.1509-1518.

IMBIE (2016). Drainage Basins. [online] Imbie.org. Available at: http://imbie.org/imbie-2016/drainage-basins/ [Accessed 9 May 2018].

Joughin, I. (2002). Ice-sheet velocity mapping: a combined interferometric and speckle-tracking approach. Annals of Glaciology, 34, pp.195-201.

Joughin, I., Smith, B., Howat, I., Scambos, T. and Moon, T. (2010). Greenland flow variability from ice-sheet-wide velocity mapping. Journal of Glaciology, 56(197), pp.415-430.

Joughin, I. 2017. MEaSUREs Greenland Annual Ice Sheet Velocity Mosaics from SAR and Landsat, Version 1. [Indicate subset used]. Boulder, Colorado USA. NASA National Snow and Ice Data Center Distributed Active Archive Center. doi: https://doi.org/10.5067/OBXCG75U7540. [Accessed 4 July 2018].

Korsgaard, N., Nuth, C., Khan, S., Kjeldsen, K., Bjørk, A., Schomacker, A. and Kjær, K. (2016). Digital elevation model and orthophotographs of Greenland based on aerial photographs from 1978–1987. Scientific Data, 3.

Laerd Statistics (2017). How to perform a one-way ANCOVA in SPSS Statistics. [online] Statistics.laerd.com. Available at: https://statistics.laerd.com/spss-tutorials/ancova-using-spss-statistics.php [Accessed 5 Jul. 2018].

LaMorte, W. (2017). Mann Whitney U Test (Wilcoxon Rank Sum Test). [online] Sphweb.bumc.bu.edu. Available at: http://sphweb.bumc.bu.edu/otlt/mph-modules/bs/bs704_nonparametric/BS704_Nonparametric4.html [Accessed 28 Feb. 2018].

Lenaerts, J., van den Broeke, M., Déry, S., van Meijgaard, E., van de Berg, W., Palm, S. and Sanz Rodrigo, J. (2012). Modeling drifting snow in Antarctica with a regional climate model: 1. Methods and model evaluation. Journal of Geophysical Research: Atmospheres, 117(D5).

Lever, J., Krzywinski, M. and Altman, N. (2017). Points of Significance: Principal component analysis. Nature Methods, 14(7), pp.641-642.

Machguth, H., Thomsen, H., Weidick, A., Ahlstrøm, A., Abermann, J., Andersen, M., Andersen, S., Bjørk, A., Box, J., Braithwaite, R., Bøggild, C., Citterio, M., Clement, P., Colgan, W., Fausto, R., Gleie, K., Gubler, S., Hasholt, B., Hynek, B., Knudsen, N., Larsen, S., MErnild, S., Oerlemans, J., Oerter, H., Olesen, O., Smeets, C., Steffen, K., Stober, M., Sugiyama, S., van As, D., van den Broeke, M. and van de Wal, R. (2016). Greenland surface mass-balance observations from the ice-sheet ablation area and local glaciers. Journal of Glaciology, 62(235), pp.861-887.

Maier, N., Parodi, F. and Verna, S. (2018). DownThemAll!. [online] Downthemall.net. Available at: https://www.downthemall.net [Accessed 3 May 2018].

McDonald, J. (2014). Handbook of Biological Statistics. 3rd ed. Baltimore: Sparky House Publishing, pp.220-228.

Messerli, A. and Grinsted, A. (2015). Image georectification and feature tracking toolbox: ImGRAFT. Geoscientific Instrumentation, Methods and Data Systems, 4(1), pp.23-34.

Minitab (2015). Choosing Between a Nonparametric Test and a Parametric Test. [online] Blog.minitab.com. Available at: http://blog.minitab.com/blog/adventures-in-statistics-2/choosing-between-a-nonparametric-test-and-a-parametric-test [Accessed 5 Jul. 2018].

Morlighem, M., Williams, C., Rignot, E., An, L., Arndt, J., Bamber, J., Catania, G., Chauché, N., Dowdeswell, J., Dorschel, B., Fenty, I., Hogan, K., Howat, I., Hubbard, A., Jakobsson, M., Jordan, T., Kjeldsen, K., Millan, R., Mayer, L., Mouginot, J., Noël, B., O'Cofaigh, C., Palmer, S., Rysgaard, S., Seroussi, H., Siegert, M., Slabon, P., Straneo, F., van den Broeke, M., Weinrebe, W., Wood, M. and Zinglersen, K. (2017). BedMachine v3: Complete Bed Topography and Ocean Bathymetry Mapping of Greenland From Multibeam Echo Sounding Combined With Mass Conservation. Geophysical Research Letters, 44(21), pp.11051-11061.

Muggeo, V. (2017). Package 'segmented'. [online] Cran.r-project.org. Available at: https://cran.r-project.org/web/packages/segmented/segmented.pdf [Accessed 19 Jul. 2018].

NASA (2018a). The Worldwide Reference System « Landsat Science. [online] Landsat.gsfc.nasa.gov. Available at: https://landsat.gsfc.nasa.gov/the-worldwide-reference-system/ [Accessed 3 May 2018].

NASA (2018b). Landsat 8. [online] Landsat.gsfc.nasa.gov. Available at: https://landsat.gsfc.nasa.gov/landsat-data-continuity-mission/ [Accessed 15 Jul. 2018].

Noël, B., van de Berg, W., Machguth, H., Lhermitte, S., Howat, I., Fettweis, X. and van den Broeke, M. (2016). A daily, 1 km resolution data set of downscaled Greenland ice sheet surface mass balance (1958–2015). The Cryosphere, 10(5), pp.2361-2377.

Noël, B., van de Berg, W., van Wessem, J., van Meijgaard, E., van As, D., Lenaerts, J., Lhermitte, S., Kuipers Munneke, P., Smeets, C., van Ulft, L., van de Wal, R. and van den

Broeke, M. (2018). Modelling the climate and surface mass balance of polar ice sheets using RACMO2 – Part 1: Greenland (1958–2016). The Cryosphere, 12(3), pp.811-831.

Ohmura, A., Calanca, P., Wild, M. and Anklin, M. (1999). Precipitation, accumulation and mass balance of the Greenland Ice sheet. Z. Gletscherkd. Glazialgeol., 35, pp.1-20.

Overly, T., Hawley, R., Helm, V., Morris, E. and Chaudhary, R. (2016). Greenland annual accumulation along the EGIG line, 1959–2004, from ASIRAS airborne radar and neutron-probe density measurements. The Cryosphere, 10(4), pp.1679-1694.

R Project (2017a). lm function | R Documentation. [online] Rdocumentation.org. Available at: https://www.rdocumentation.org/packages/stats/versions/3.5.0/topics/lm [Accessed 9 May 2018].

R Project (2017b). wilcox.test function | R Documentation. [online] Rdocumentation.org. Available at: https://www.rdocumentation.org/packages/stats/versions/3.5.0/topics/wilcox.test [Accessed 9 May 2018].

Scambos, T., Dutkiewicz, M., Wilson, J. and Bindschadler, R. (1992). Application of image cross-correlation to the measurement of glacier velocity using satellite image data. Remote Sensing of Environment, 42(3), pp.177-186.

SciPy Cookbook (2012). Savitzky Golay Filtering — SciPy Cookbook documentation. [online] Scipy-cookbook.readthedocs.io. Available at: http://scipy-cookbook.readthedocs.io/items/SavitzkyGolay.html [Accessed 14 Jul. 2018].

Sole, A., Nienow, P., Bartholomew, I., Mair, D., Cowton, T., Tedstone, A. and King, M. (2013). Winter motion mediates dynamic response of the Greenland Ice Sheet to warmer summers. Geophysical Research Letters, 40(15), pp.3940-3944.

Tedstone, A., Nienow, P., Gourmelen, N., Dehecq, A., Goldberg, D. and Hanna, E. (2015). Decadal slowdown of a land-terminating sector of the Greenland Ice Sheet despite warming. Nature, 526(7575), pp.692-695.

Tedstone, A., Nienow, P., Sole, A., Mair, D., Cowton, T., Bartholomew, I. and King, M. (2013). Greenland ice sheet motion insensitive to exceptional meltwater forcing. Proceedings of the National Academy of Sciences, 110(49), pp.19719-19724.

Thompson, R. and Emery, W. (2014). Digital Filters. In: R. Thompson and W. Emery, ed., Data Analysis Methods in Physical Oceanography, 3rd ed. [online] Elsevier, pp.593–637. Available at: https://doi.org/10.1016/B978-0-12-387782-6.00006-5 [Accessed 3 May 2018].

UCLA (2018). click2shp | browser-based shapefile creation tool. [online] Gis.ucla.edu. Available at: http://gis.ucla.edu/apps/click2shp/ [Accessed 3 May 2018].

Unden, P., Rontu, L., Järvinen, H., Lynch, P., Calvo, J., Cats, G., Cuxar, J., Eerola, K., Fortelius, C., Garcia-Moya, J., Jones, C., Geert, Lenderlink, G., Mcdonald, A., Mcgrath, R., Navascues, B., Nielsen, N., Degaard, V., Rodriguez, E., Rummukainen, M., Sattler, K., Sass, B., Savijarvi, H., Schreur, B., Sigg, R. and The, H. (2002). HIRLAM-5 Scientific Documentation.

University of Edinburgh (2017). High-performance computing. [online] The University of Edinburgh Information Services. Available at: https://www.ed.ac.uk/information-services/research-support/research-computing/ecdf/high-performance-computing [Accessed 9 May 2018].

USGS (2018a). Landsat Processing Details. [online] Landsat.usgs.gov. Available at: https://landsat.usgs.gov/landsat-processing-details [Accessed 29 Apr. 2018].

USGS (2018b). Landsat Collections. [online] Landsat.usgs.gov. Available at: https://landsat.usgs.gov/landsat-collections [Accessed 29 Apr. 2018].

USGS (2018c). Bulk Download Application 1.3.6. [online] Earthexplorer.usgs.gov. Available at: https://earthexplorer.usgs.gov/bulk/ [Accessed 3 May 2018].

USGS (2018d). SLC-off Products: Background | Landsat Missions. [online] Landsat.usgs.gov. Available at: https://landsat.usgs.gov/slc-products-background [Accessed 15 Jul. 2018].

USGS (2018e). What are the band designations for the Landsat satellites?. [online] Landsat.usgs.gov. Available at: https://landsat.usgs.gov/what-are-band-designations-landsat-satellites [Accessed 29 Apr. 2018].

USGS (2018f). Geometry | Landsat Missions. [online] Landsat.usgs.gov. Available at: https://landsat.usgs.gov/geometry [Accessed 19 Jul. 2018].

USGS (2018g). Known Issues. [online] Landsat.usgs.gov. Available at: https://landsat.usgs.gov/known-issues [Accessed 15 Jul. 2018].

Zwally, J., Giovinetto, M., Beckley, M. and Saba, J. (2012). Antarctic and Greenland Drainage Systems. [online] GSFC Cryospheric Sciences Laboratory. Available at: https://icesat4.gsfc.nasa.gov/cryo_data/ant_grn_drainage_systems.php [Accessed 9 May 2018].

5. Appendix:

5.1. Antecedent runoff regression results:

Table 4: R^2 values and associated p-values, produced when carrying out regressions between antecedent runoff production and median annual velocities.

	Including velocity year				Excluding velocity year			
	RACMO2.3p2		MAR		RACMO2.3p2		MAR	
Antecedent melt year	R^2	p value	R^2	p value	R^2	p value	R^2	p value
0	0.131	0.184	0.192	0.117	N/A	N/A	N/A	N/A
1	0.287	0.039	0.374	0.020	0.097	0.259	0.160	0.157
2	0.410	0.010	0.392	0.017	0.314	0.030	0.314	0.037
3	0.590	0.001	0.476	0.006	0.538	0.002	0.436	0.010
4	0.452	0.006	0.392	0.017	0.416	0.009	0.364	0.022
5	0.437	0.007	0.361	0.023	0.395	0.012	0.336	0.030

5.2. Velocity time series statistical test results:

5.2.1. Mann-Whitney-Wilcoxon test results:

Table 5: MWW test results produced when locating break date in velocity time series.

Year	Test statistic (W)	P value
1995.5	34	0.138
2000	36	0.207
2002	45	0.036
2006.5	50	0.009
2007.5	50	0.009
2008.5	51	0.002
2009.5	50	0.001

5.2.2. Segmented linear regression results:

Table 6: Segmented linear regression results produced when locating break date in velocity time series.

Year	Residual standard error (m yr^{-1})	R^2	p value
1998	1.705	0.467	0.065
1999	1.696	0.473	0.062
2000	1.691	0.476	0.060
2001	1.626	0.516	0.040
2002	1.554	0.557	0.025
2003	1.510	0.583	0.019
2004	1.463	0.608	0.013
2005	1.422	0.630	0.010
2006	1.398	0.642	0.008
2007	1.405	0.638	0.009
2008	1.415	0.633	0.009
2009	1.436	0.622	0.011

5.3. Runoff segmented linear regression results table:

Table 7: Residual standard error (RSE) associated with applying all possible break date combinations to MAR and RACMO2.3p2 annual data.

MAR			RACMO2.3p2		
Break date 1	Break date 2	RSE	Break date 1	Break date 2	RSE
1986	1987	474.437022	1986	1987	401.015861
1986	1988	473.289995	1986	1988	405.38299
1986	1989	468.218802	1986	1989	404.739374
1986	1990	466.702213	1986	1990	403.850581
1986	1991	462.2138	1986	1991	401.979502
1986	1992	458.532695	1986	1992	400.771966
1986	1993	462.588813	1986	1993	402.314161
1986	1994	463.959824	1986	1994	402.179551
1986	1995	465.875161	1986	1995	402.446574
1986	1996	465.397971	1986	1996	401.322787
1986	1997	467.678005	1986	1997	402.054761
1986	1998	470.093847	1986	1998	403.210707
1986	1999	470.999876	1986	1999	403.863049
1986	2000	472.222422	1986	2000	404.608021
1986	2001	473.241382	1986	2001	405.301109
1986	2002	474.182147	1986	2002	405.576349
1986	2003	474.723773	1986	2003	405.455309
1986	2004	474.763072	1986	2004	405.34722
1986	2005	474.664427	1986	2005	405.155786
1986	2006	474.410746	1986	2006	404.799897
1986	2007	473.859794	1986	2007	403.830367
1986	2008	473.626979	1986	2008	403.135047
1986	2009	473.089706	1986	2009	401.642942
1986	2010	468.871312	1986	2010	397.673265
1986	2011	467.171208	1986	2011	396.176415
1986	2012	460.679643	1986	2012	395.131431
1986	2013	472.993865	1986	2013	400.838753
1987	1987	471.889567	1986	2014	402.26348
1987	1988	475.177835	1987	1987	407.479335
1987	1989	467.913436	1987	1988	412.769548
1987	1990	468.675806	1987	1989	408.143178
1987	1991	464.023283	1987	1990	408.157408
1987	1992	460.683349	1987	1991	405.8806
1987	1993	466.886547	1987	1992	405.097965
1987	1994	469.07713	1987	1993	408.456931
1987	1995	471.587469	1987	1994	408.773016
1987	1996	471.276158	1987	1995	409.533913

1987	1997	473.867954	1987	1996	408.317937
1987	1998	476.454676	1987	1997	409.530838
1987	1999	477.403466	1987	1998	411.190982
1987	2000	478.6262	1987	1999	412.140251
1987	2001	479.605136	1987	2000	413.172803
1987	2002	480.459503	1987	2001	414.148141
1987	2003	480.87205	1987	2002	414.636676
1987	2004	480.846788	1987	2003	414.654078
1987	2005	480.688339	1987	2004	414.578186
1987	2006	480.378299	1987	2005	414.423334
1987	2007	479.762726	1987	2006	414.112353
1987	2008	479.529742	1987	2007	413.224039
1987	2009	478.978224	1987	2008	412.56082
1987	2010	474.618795	1987	2009	411.131786
1987	2011	472.95374	1987	2010	407.301075
1987	2012	466.484448	1987	2011	405.834375
1987	2013	479.024418	1987	2012	404.799991
1988	1987	475.177835	1987	2013	410.272536
1988	1988	467.543043	1987	2014	411.606424
1988	1989	464.899609	1988	1987	412.769548
1988	1990	468.289701	1988	1988	405.882282
1988	1991	463.537768	1988	1989	405.052502
1988	1992	460.338374	1988	1990	407.356683
1988	1993	466.854189	1988	1991	405.168386
1988	1994	468.793347	1988	1992	404.711781
1988	1995	470.854652	1988	1993	408.480107
1988	1996	470.41137	1988	1994	408.787755
1988	1997	472.432225	1988	1995	409.473594
1988	1998	474.317601	1988	1996	408.284606
1988	1999	474.894282	1988	1997	409.367617
1988	2000	475.63173	1988	1998	410.791302
1988	2001	476.142135	1988	1999	411.538907
1988	2002	476.440773	1988	2000	412.307706
1988	2003	476.243697	1988	2001	412.926865
1988	2004	475.983747	1988	2002	413.050551
1988	2005	475.625155	1988	2003	412.766222
1988	2006	475.13419	1988	2004	412.61659
1988	2007	474.303751	1988	2005	412.372396
1988	2008	474.10047	1988	2006	411.945108
1988	2009	473.511633	1988	2007	410.828173
1988	2010	468.53197	1988	2008	410.089316
1988	2011	466.92629	1988	2009	408.504026
1988	2012	460.237287	1988	2010	404.32815
1988	2013	474.162361	1988	2011	402.886278
1989	1987	467.913436	1988	2012	401.948691

1989	1988	464.899609	1988	2013	407.987195
1989	1989	461.241244	1988	2014	409.54144
1989	1990	469.221168	1989	1987	408.143178
1989	1991	464.222442	1989	1988	405.052502
1989	1992	460.743896	1989	1989	402.218475
1989	1993	466.120833	1989	1990	408.576067
1989	1994	467.192448	1989	1991	405.960415
1989	1995	468.294466	1989	1992	405.188266
1989	1996	467.768166	1989	1993	407.928254
1989	1997	468.864389	1989	1994	407.913282
1989	1998	469.714775	1989	1995	408.189825
1989	1999	469.868442	1989	1996	407.201019
1989	2000	470.017996	1989	1997	407.840364
1989	2001	469.983032	1989	1998	408.660047
1989	2002	469.621683	1989	1999	409.002137
1989	2003	468.702332	1989	2000	409.281505
1989	2004	468.249297	1989	2001	409.278963
1989	2005	467.737054	1989	2002	408.813694
1989	2006	467.110648	1989	2003	408.082046
1989	2007	466.092578	1989	2004	407.883818
1989	2008	466.018107	1989	2005	407.559055
1989	2009	465.460475	1989	2006	407.002981
1989	2010	459.746778	1989	2007	405.57473
1989	2011	458.285701	1989	2008	404.769159
1989	2012	451.368611	1989	2009	402.986703
1989	2013	467.134078	1989	2010	398.318264
1990	1987	468.675806	1989	2011	396.954566
1990	1988	468.289701	1989	2012	396.200044
1990	1989	469.221168	1989	2013	403.148216
1990	1990	460.466648	1989	2014	405.072405
1990	1991	460.450439	1990	1987	408.157408
1990	1992	458.473804	1990	1988	407.356683
1990	1993	466.648168	1990	1989	408.576067
1990	1994	467.749645	1990	1990	401.497248
1990	1995	468.59798	1990	1991	404.175018
1990	1996	468.159545	1990	1992	404.54518
1990	1997	468.889155	1990	1993	408.013383
1990	1998	469.235154	1990	1994	407.979474
1990	1999	469.231599	1990	1995	408.161136
1990	2000	469.103186	1990	1996	407.323605
1990	2001	468.80379	1990	1997	407.83105
1990	2002	468.09067	1990	1998	408.393207
1990	2003	466.767214	1990	1999	408.556163
1990	2004	466.260724	1990	2000	408.588879
1990	2005	465.715019	1990	2001	408.236482

1990	2006	465.06195	1990	2002	407.426426
1990	2007	463.979609	1990	2003	406.438205
1990	2008	464.040384	1990	2004	406.256065
1990	2009	463.550516	1990	2005	405.920093
1990	2010	457.434979	1990	2006	405.316383
1990	2011	456.119337	1990	2007	403.715098
1990	2012	449.140811	1990	2008	402.900239
1990	2013	465.980656	1990	2009	401.020317
1991	1987	464.023283	1990	2010	396.060093
1991	1988	463.537768	1990	2011	394.785261
1991	1989	464.222442	1990	2012	394.184631
1991	1990	460.450439	1990	2013	401.723086
1991	1991	455.874133	1990	2014	403.887911
1991	1992	458.759968	1991	1987	405.8806
1991	1993	464.557412	1991	1988	405.168386
1991	1994	464.506133	1991	1989	405.960415
1991	1995	464.281576	1991	1990	404.175018
1991	1996	464.551911	1991	1991	399.233406
1991	1997	464.337576	1991	1992	405.038781
1991	1998	463.637369	1991	1993	405.984965
1991	1999	463.533287	1991	1994	406.23378
1991	2000	463.027862	1991	1995	406.235796
1991	2001	462.390769	1991	1996	406.136795
1991	2002	461.178425	1991	1997	406.265387
1991	2003	459.274477	1991	1998	406.2521
1991	2004	458.822957	1991	1999	406.121474
1991	2005	458.347849	1991	2000	405.756713
1991	2006	457.76014	1991	2001	404.85285
1991	2007	456.664169	1991	2002	403.540196
1991	2008	457.038429	1991	2003	402.219028
1991	2009	456.733432	1991	2004	402.149099
1991	2010	449.993908	1991	2005	401.86829
1991	2011	448.965943	1991	2006	401.253114
1991	2012	441.893224	1991	2007	399.441116
1991	2013	460.633454	1991	2008	398.66317
1992	1987	460.683349	1991	2009	396.680931
1992	1988	460.338374	1991	2010	391.324387
1992	1989	460.743896	1991	2011	390.215529
1992	1990	458.473804	1991	2012	389.870425
1992	1991	458.759968	1991	2013	398.315736
1992	1992	452.40391	1991	2014	400.862417
1992	1993	450.182985	1992	1987	405.097965
1992	1994	455.535326	1992	1988	404.711781
1992	1995	456.048927	1992	1989	405.188266
1992	1996	459.112961	1992	1990	404.54518

1992	1997	458.265821	1992	1991	405.038781
1992	1998	456.727907	1992	1992	398.249667
1992	1999	456.999371	1992	1993	397.834855
1992	2000	456.405617	1992	1994	403.218388
1992	2001	455.673975	1992	1995	403.92757
1992	2002	454.139583	1992	1996	405.249894
1992	2003	451.801215	1992	1997	405.132576
1992	2004	451.613991	1992	1998	404.647529
1992	2005	451.386189	1992	1999	404.34848
1992	2006	451.013132	1992	2000	403.69502
1992	2007	450.027615	1992	2001	402.340139
1992	2008	450.836069	1992	2002	400.625794
1992	2009	450.812801	1992	2003	399.071499
1992	2010	443.529344	1992	2004	399.199084
1992	2011	442.872012	1992	2005	399.043529
1992	2012	435.787675	1992	2006	398.479508
1992	2013	456.417183	1992	2007	396.527869
1993	1987	466.886547	1992	2008	395.834474
1993	1988	466.854189	1992	2009	393.806123
1993	1989	466.120833	1992	2010	388.14098
1993	1990	466.648168	1992	2011	387.223608
1993	1991	464.557412	1992	2012	387.140568
1993	1992	450.182985	1992	2013	396.379578
1993	1993	458.231177	1992	2014	399.260567
1993	1994	464.492454	1993	1987	408.456931
1993	1995	463.411262	1993	1988	408.480107
1993	1996	466.032306	1993	1989	407.928254
1993	1997	464.893253	1993	1990	408.013383
1993	1998	463.05166	1993	1991	405.984965
1993	1999	463.237577	1993	1992	397.834855
1993	2000	462.535036	1993	1993	401.388565
1993	2001	461.720938	1993	1994	408.426045
1993	2002	460.085282	1993	1995	408.245836
1993	2003	457.635551	1993	1996	408.268326
1993	2004	457.478118	1993	1997	408.490789
1993	2005	457.279809	1993	1998	408.223287
1993	2006	456.933445	1993	1999	407.906915
1993	2007	455.965303	1993	2000	407.233414
1993	2008	456.823312	1993	2001	405.822743
1993	2009	456.830659	1993	2002	404.019673
1993	2010	449.558675	1993	2003	402.393399
1993	2011	448.963576	1993	2004	402.532756
1993	2012	441.980826	1993	2005	402.378737
1993	2013	462.450753	1993	2006	401.809104
1994	1987	469.07713	1993	2007	399.831479

1994	1988	468.793347	1993	2008	399.146511
1994	1989	467.192448	1993	2009	397.115552
1994	1990	467.749645	1993	2010	391.427271
1994	1991	464.506133	1993	2011	390.552184
1994	1992	455.535326	1993	2012	390.512068
1994	1993	464.492454	1993	2013	399.746722
1994	1994	460.839818	1993	2014	402.596822
1994	1995	463.608612	1994	1987	408.773016
1994	1996	468.645743	1994	1988	408.787755
1994	1997	466.821822	1994	1989	407.913282
1994	1998	464.281182	1994	1990	407.979474
1994	1999	464.714115	1994	1991	406.23378
1994	2000	463.962051	1994	1992	403.218388
1994	2001	463.112747	1994	1993	408.426045
1994	2002	461.324585	1994	1994	401.833734
1994	2003	458.671564	1994	1995	407.904949
1994	2004	458.703513	1994	1996	408.683668
1994	2005	458.669449	1994	1997	408.929247
1994	2006	458.459524	1994	1998	408.264058
1994	2007	457.57408	1994	1999	407.777961
1994	2008	458.642693	1994	2000	406.844605
1994	2009	458.784913	1994	2001	405.031214
1994	2010	451.357348	1994	2002	402.885288
1994	2011	450.941384	1994	2003	401.091901
1994	2012	444.034719	1994	2004	401.468594
1994	2013	464.979936	1994	2005	401.466184
1995	1987	471.587469	1994	2006	400.973931
1995	1988	470.854652	1994	2007	398.912972
1995	1989	468.294466	1994	2008	398.326382
1995	1990	468.59798	1994	2009	396.287723
1995	1991	464.281576	1994	2010	390.392784
1995	1992	456.048927	1994	2011	389.695798
1995	1993	463.411262	1994	2012	389.875078
1995	1994	463.608612	1994	2013	399.65803
1995	1995	464.146258	1994	2014	402.72158
1995	1996	472.951806	1995	1987	409.533913
1995	1997	470.783486	1995	1988	409.473594
1995	1998	467.154091	1995	1989	408.189825
1995	1999	467.699379	1995	1990	408.161136
1995	2000	466.809265	1995	1991	406.235796
1995	2001	465.87478	1995	1992	403.92757
1995	2002	463.917911	1995	1993	408.245836
1995	2003	461.067339	1995	1994	407.904949
1995	2004	461.260364	1995	1995	402.848646
1995	2005	461.358438	1995	1996	407.02527

1995	2006	461.253136	1995	1997	409.973128
1995	2007	460.428984	1995	1998	409.084901
1995	2008	461.6473	1995	1999	408.401733
1995	2009	461.879112	1995	2000	407.200245
1995	2010	454.362152	1995	2001	404.982249
1995	2011	454.071327	1995	2002	402.508898
1995	2012	447.240015	1995	2003	400.581951
1995	2013	468.353775	1995	2004	401.231703
1996	1987	471.276158	1995	2005	401.398671
1996	1988	470.41137	1995	2006	400.996346
1996	1989	467.768166	1995	2007	398.876155
1996	1990	468.159545	1995	2008	398.392415
1996	1991	464.551911	1995	2009	396.361167
1996	1992	459.112961	1995	2010	390.304412
1996	1993	466.032306	1995	2011	389.775479
1996	1994	468.645743	1995	2012	390.149133
1996	1995	472.951806	1995	2013	400.355544
1996	1996	464.247218	1995	2014	403.568485
1996	1997	461.224502	1996	1987	408.317937
1996	1998	457.175831	1996	1988	408.284606
1996	1999	461.599825	1996	1989	407.201019
1996	2000	461.648708	1996	1990	407.323605
1996	2001	461.304016	1996	1991	406.136795
1996	2002	459.40153	1996	1992	405.249894
1996	2003	456.41231	1996	1993	408.268326
1996	2004	457.37099	1996	1994	408.683668
1996	2005	458.062312	1996	1995	407.02527
1996	2006	458.414192	1996	1996	401.652055
1996	2007	457.880027	1996	1997	405.055483
1996	2008	459.63372	1996	1998	401.993324
1996	2009	460.209531	1996	1999	402.305497
1996	2010	452.374369	1996	2000	401.099491
1996	2011	452.472153	1996	2001	398.286236
1996	2012	445.749696	1996	2002	395.481096
1996	2013	468.074929	1996	2003	393.686834
1997	1987	473.867954	1996	2004	395.395787
1997	1988	472.432225	1996	2005	396.242362
1997	1989	468.864389	1996	2006	396.248466
1997	1990	468.889155	1996	2007	394.121422
1997	1991	464.337576	1996	2008	393.998695
1997	1992	458.265821	1996	2009	392.068315
1997	1993	464.893253	1996	2010	385.684369
1997	1994	466.821822	1996	2011	385.594373
1997	1995	470.783486	1996	2012	386.466647
1997	1996	461.224502	1996	2013	397.85034

1997	1997	467.968813	1996	2014	401.550777
1997	1998	457.336521	1997	1987	409.530838
1997	1999	465.539259	1997	1988	409.367617
1997	2000	465.502386	1997	1989	407.840364
1997	2001	465.083224	1997	1990	407.83105
1997	2002	462.944013	1997	1991	406.265387
1997	2003	459.712959	1997	1992	405.132576
1997	2004	460.939008	1997	1993	408.490789
1997	2005	461.798971	1997	1994	408.929247
1997	2006	462.256339	1997	1995	409.973128
1997	2007	461.771385	1997	1996	405.055483
1997	2008	463.62951	1997	1997	403.239465
1997	2009	464.247839	1997	1998	399.682647
1997	2010	456.370932	1997	1999	402.00672
1997	2011	456.538018	1997	2000	400.860819
1997	2012	449.879938	1997	2001	397.61115
1997	2013	472.039262	1997	2002	394.612007
1998	1987	476.454676	1997	2003	392.968819
1998	1988	474.317601	1997	2004	395.405624
1998	1989	469.714775	1997	2005	396.656389
1998	1990	469.235154	1997	2006	396.880652
1998	1991	463.637369	1997	2007	394.754302
1998	1992	456.727907	1997	2008	394.809525
1998	1993	463.05166	1997	2009	392.933606
1998	1994	464.281182	1997	2010	386.427607
1998	1995	467.154091	1997	2011	386.545144
1998	1996	457.175831	1997	2012	387.625865
1998	1997	457.336521	1997	2013	399.35023
1998	1998	471.972611	1997	2014	403.14039
1998	1999	475.91785	1998	1987	411.190982
1998	2000	473.14747	1998	1988	410.791302
1998	2001	471.645595	1998	1989	408.660047
1998	2002	468.800598	1998	1990	408.393207
1998	2003	465.071764	1998	1991	406.2521
1998	2004	466.295433	1998	1992	404.647529
1998	2005	467.107098	1998	1993	408.223287
1998	2006	467.498224	1998	1994	408.264058
1998	2007	466.941756	1998	1995	409.084901
1998	2008	468.733351	1998	1996	401.993324
1998	2009	469.272726	1998	1997	399.682647
1998	2010	461.416007	1998	1998	405.491328
1998	2011	461.534066	1998	1999	406.768361
1998	2012	454.900519	1998	2000	404.114726
1998	2013	476.471153	1998	2001	399.806269
1999	1987	477.403466	1998	2002	396.351458

1999	1988	474.894282	1998	2003	394.722504
1999	1989	469.868442	1998	2004	397.701111
1999	1990	469.231599	1998	2005	399.170703
1999	1991	463.533287	1998	2006	399.471398
1999	1992	456.999371	1998	2007	397.29598
1999	1993	463.237577	1998	2008	397.414509
1999	1994	464.714115	1998	2009	395.539998
1999	1995	467.699379	1998	2010	388.961683
1999	1996	461.599825	1998	2011	389.170666
1999	1997	465.539259	1998	2012	390.32324
1999	1998	475.91785	1998	2013	402.036187
1999	1999	473.833013	1998	2014	405.740763
1999	2000	471.975722	1999	1987	412.140251
1999	2001	471.001279	1999	1988	411.538907
1999	2002	467.899689	1999	1989	409.002137
1999	2003	463.899315	1999	1990	408.556163
1999	2004	466.183251	1999	1991	406.121474
1999	2005	467.608364	1999	1992	404.34848
1999	2006	468.375611	1999	1993	407.906915
1999	2007	468.01454	1999	1994	407.777961
1999	2008	470.139208	1999	1995	408.401733
1999	2009	470.84746	1999	1996	402.305497
1999	2010	462.815398	1999	1997	402.00672
1999	2011	463.132971	1999	1998	406.768361
1999	2012	456.570529	1999	1999	406.961689
1999	2013	478.412664	1999	2000	403.227141
2000	1987	478.6262	1999	2001	397.649328
2000	1988	475.63173	1999	2002	394.229083
2000	1989	470.017996	1999	2003	393.284308
2000	1990	469.103186	1999	2004	397.704763
2000	1991	463.027862	1999	2005	399.798987
2000	1992	456.405617	1999	2006	400.377683
2000	1993	462.535036	1999	2007	398.191849
2000	1994	463.962051	1999	2008	398.504271
2000	1995	466.809265	1999	2009	396.678172
2000	1996	461.648708	1999	2010	389.96768
2000	1997	465.502386	1999	2011	390.382324
2000	1998	473.14747	1999	2012	391.721162
2000	1999	471.975722	1999	2013	403.667953
2000	2000	476.18751	1999	2014	407.384053
2000	2001	473.495259	2000	1987	413.172803
2000	2002	469.126675	2000	1988	412.307706
2000	2003	464.54266	2000	1989	409.281505
2000	2004	468.023533	2000	1990	408.588879
2000	2005	469.952769	2000	1991	405.756713

2000	2006	470.949994	2000	1992	403.69502
2000	2007	470.662999	2000	1993	407.233414
2000	2008	472.948709	2000	1994	406.844605
2000	2009	473.695069	2000	1995	407.200245
2000	2010	465.548292	2000	1996	401.099491
2000	2011	465.941689	2000	1997	400.860819
2000	2012	459.410436	2000	1998	404.114726
2000	2013	481.056588	2000	1999	403.227141
2001	1987	479.605136	2000	2000	408.651711
2001	1988	476.142135	2000	2001	395.251666
2001	1989	469.983032	2000	2002	392.624016
2001	1990	468.80379	2000	2003	392.958879
2001	1991	462.390769	2000	2004	399.200163
2001	1992	455.673975	2000	2005	401.835248
2001	1993	461.720938	2000	2006	402.564262
2001	1994	463.112747	2000	2007	400.293671
2001	1995	465.87478	2000	2008	400.699883
2001	1996	461.304016	2000	2009	398.864616
2001	1997	465.083224	2000	2010	392.034497
2001	1998	471.645595	2000	2011	392.565255
2001	1999	471.001279	2000	2012	393.985863
2001	2000	473.495259	2000	2013	405.906036
2001	2001	478.291199	2000	2014	409.499582
2001	2002	468.696453	2001	1987	414.148141
2001	2003	463.653638	2001	1988	412.926865
2001	2004	469.643049	2001	1989	409.278963
2001	2005	472.321851	2001	1990	408.236482
2001	2006	473.579481	2001	1991	404.85285
2001	2007	473.341495	2001	1992	402.340139
2001	2008	475.769617	2001	1993	405.822743
2001	2009	476.518551	2001	1994	405.031214
2001	2010	468.238147	2001	1995	404.982249
2001	2011	468.684465	2001	1996	398.286236
2001	2012	462.1656	2001	1997	397.61115
2001	2013	483.506743	2001	1998	399.806269
2002	1987	480.459503	2001	1999	397.649328
2002	1988	476.440773	2001	2000	395.251666
2002	1989	469.621683	2001	2001	410.487952
2002	1990	468.09067	2001	2002	395.736823
2002	1991	461.178425	2001	2003	396.606808
2002	1992	454.139583	2001	2004	404.01107
2002	1993	460.085282	2001	2005	406.439367
2002	1994	461.324585	2001	2006	406.85139
2002	1995	463.917911	2001	2007	404.301025
2002	1996	459.40153	2001	2008	404.537382

2002	1997	462.944013	2001	2009	402.561186
2002	1998	468.800598	2001	2010	395.632375
2002	1999	467.899689	2001	2011	396.088791
2002	2000	469.126675	2001	2012	397.393606
2002	2001	468.696453	2001	2013	408.849375
2002	2002	480.453468	2001	2014	412.115406
2002	2003	464.794434	2002	1987	414.636676
2002	2004	474.373679	2002	1988	413.050551
2002	2005	477.08354	2002	1989	408.813694
2002	2006	478.068523	2002	1990	407.426426
2002	2007	477.549154	2002	1991	403.540196
2002	2008	479.77896	2002	1992	400.625794
2002	2009	480.311694	2002	1993	404.019673
2002	2010	471.963523	2002	1994	402.885288
2002	2011	472.287709	2002	1995	402.508898
2002	2012	465.716224	2002	1996	395.481096
2002	2013	486.218061	2002	1997	394.612007
2003	1987	480.87205	2002	1998	396.351458
2003	1988	476.243697	2002	1999	394.229083
2003	1989	468.702332	2002	2000	392.624016
2003	1990	466.767214	2002	2001	395.736823
2003	1991	459.274477	2002	2002	411.869793
2003	1992	451.801215	2002	2003	402.463196
2003	1993	457.635551	2002	2004	410.347385
2003	1994	458.671564	2002	2005	411.740897
2003	1995	461.067339	2002	2006	411.462097
2003	1996	456.41231	2002	2007	408.49127
2003	1997	459.712959	2002	2008	408.418465
2003	1998	465.071764	2002	2009	406.233769
2003	1999	463.899315	2002	2010	399.185894
2003	2000	464.54266	2002	2011	399.504895
2003	2001	463.653638	2002	2012	400.632562
2003	2002	464.794434	2002	2013	411.48567
2003	2003	482.301781	2002	2014	414.360869
2003	2004	485.045879	2003	1987	414.654078
2003	2005	484.700023	2003	1988	412.766222
2003	2006	484.269189	2003	1989	408.082046
2003	2007	482.961953	2003	1990	406.438205
2003	2008	484.525443	2003	1991	402.219028
2003	2009	484.600984	2003	1992	399.071499
2003	2010	476.296469	2003	1993	402.393399
2003	2011	476.315087	2003	1994	401.091901
2003	2012	469.629348	2003	1995	400.581951
2003	2013	488.772159	2003	1996	393.686834
2004	1987	480.846788	2003	1997	392.968819

2004	1988	475.983747	2003	1998	394.722504
2004	1989	468.249297	2003	1999	393.284308
2004	1990	466.260724	2003	2000	392.958879
2004	1991	458.822957	2003	2001	396.606808
2004	1992	451.613991	2003	2002	402.463196
2004	1993	457.478118	2003	2003	412.660462
2004	1994	458.703513	2003	2004	417.301152
2004	1995	461.260364	2003	2005	416.5005
2004	1996	457.37099	2003	2006	415.28783
2004	1997	460.939008	2003	2007	411.799086
2004	1998	466.295433	2003	2008	411.410786
2004	1999	466.183251	2003	2009	409.00389
2004	2000	468.023533	2003	2010	401.761088
2004	2001	469.643049	2003	2011	402.007312
2004	2002	474.373679	2003	2012	403.021163
2004	2003	485.045879	2003	2013	413.387588
2004	2004	482.998224	2003	2014	415.915539
2004	2005	486.271569	2004	1987	414.578186
2004	2006	485.599134	2004	1988	412.61659
2004	2007	484.071168	2004	1989	407.883818
2004	2008	485.896982	2004	1990	406.256065
2004	2009	485.95225	2004	1991	402.149099
2004	2010	477.256469	2004	1992	399.199084
2004	2011	477.437597	2004	1993	402.532756
2004	2012	470.741838	2004	1994	401.468594
2004	2013	489.77582	2004	1995	401.231703
2005	1987	480.688339	2004	1996	395.395787
2005	1988	475.625155	2004	1997	395.405624
2005	1989	467.737054	2004	1998	397.701111
2005	1990	465.715019	2004	1999	397.704763
2005	1991	458.347849	2004	2000	399.200163
2005	1992	451.386189	2004	2001	404.01107
2005	1993	457.279809	2004	2002	410.347385
2005	1994	458.669449	2004	2003	417.301152
2005	1995	461.358438	2004	2004	412.871114
2005	1996	458.062312	2004	2005	416.521663
2005	1997	461.798971	2004	2006	415.060537
2005	1998	467.107098	2004	2007	410.830329
2005	1999	467.608364	2004	2008	410.89938
2005	2000	469.952769	2004	2009	408.472062
2005	2001	472.321851	2004	2010	400.720834
2005	2002	477.08354	2004	2011	401.490148
2005	2003	484.700023	2004	2012	402.914326
2005	2004	486.271569	2004	2013	413.788884
2005	2005	483.488045	2004	2014	416.326331

2005	2006	486.822719	2005	1987	414.423334
2005	2007	484.834379	2005	1988	412.372396
2005	2008	487.17223	2005	1989	407.559055
2005	2009	487.188925	2005	1990	405.920093
2005	2010	477.912462	2005	1991	401.86829
2005	2011	478.345773	2005	1992	399.043529
2005	2012	471.637533	2005	1993	402.378737
2005	2013	490.597378	2005	1994	401.466184
2006	1987	480.378299	2005	1995	401.398671
2006	1988	475.13419	2005	1996	396.242362
2006	1989	467.110648	2005	1997	396.656389
2006	1990	465.06195	2005	1998	399.170703
2006	1991	457.76014	2005	1999	399.798987
2006	1992	451.013132	2005	2000	401.835248
2006	1993	456.933445	2005	2001	406.439367
2006	1994	458.459524	2005	2002	411.740897
2006	1995	461.253136	2005	2003	416.5005
2006	1996	458.414192	2005	2004	416.521663
2006	1997	462.256339	2005	2005	413.033135
2006	1998	467.498224	2005	2006	414.797692
2006	1999	468.375611	2005	2007	409.156245
2006	2000	470.949994	2005	2008	410.289056
2006	2001	473.579481	2005	2009	407.898664
2006	2002	478.068523	2005	2010	399.505553
2006	2003	484.269189	2005	2011	401.009885
2006	2004	485.599134	2005	2012	402.936542
2006	2005	486.822719	2005	2013	414.312392
2006	2006	483.782125	2005	2014	416.801174
2006	2007	485.146927	2006	1987	414.112353
2006	2008	488.631506	2006	1988	411.945108
2006	2009	488.489037	2006	1989	407.002981
2006	2010	478.321245	2006	1990	405.316383
2006	2011	479.137267	2006	1991	401.253114
2006	2012	472.408332	2006	1992	398.479508
2006	2013	491.270433	2006	1993	401.809104
2007	1987	479.762726	2006	1994	400.973931
2007	1988	474.303751	2006	1995	400.996346
2007	1989	466.092578	2006	1996	396.248466
2007	1990	463.979609	2006	1997	396.880652
2007	1991	456.664169	2006	1998	399.471398
2007	1992	450.027615	2006	1999	400.377683
2007	1993	455.965303	2006	2000	402.564262
2007	1994	457.57408	2006	2001	406.85139
2007	1995	460.428984	2006	2002	411.462097
2007	1996	457.880027	2006	2003	415.28783

2007	1997	461.771385	2006	2004	415.060537
2007	1998	466.941756	2006	2005	414.797692
2007	1999	468.01454	2006	2006	413.098038
2007	2000	470.662999	2006	2007	405.42009
2007	2001	473.341495	2006	2008	409.862379
2007	2002	477.549154	2006	2009	407.557139
2007	2003	482.961953	2006	2010	398.288945
2007	2004	484.071168	2006	2011	400.805453
2007	2005	484.834379	2006	2012	403.297486
2007	2006	485.146927	2006	2013	415.037263
2007	2007	483.838207	2006	2014	417.359359
2007	2008	491.7272	2007	1987	413.224039
2007	2009	490.580672	2007	1988	410.828173
2007	2010	479.166165	2007	1989	405.57473
2007	2011	480.350937	2007	1990	403.715098
2007	2012	473.521105	2007	1991	399.441116
2007	2013	491.834856	2007	1992	396.527869
2008	1987	479.529742	2007	1993	399.831479
2008	1988	474.10047	2007	1994	398.912972
2008	1989	466.018107	2007	1995	398.876155
2008	1990	464.040384	2007	1996	394.121422
2008	1991	457.038429	2007	1997	394.754302
2008	1992	450.836069	2007	1998	397.29598
2008	1993	456.823312	2007	1999	398.191849
2008	1994	458.642693	2007	2000	400.293671
2008	1995	461.6473	2007	2001	404.301025
2008	1996	459.63372	2007	2002	408.49127
2008	1997	463.62951	2007	2003	411.799086
2008	1998	468.733351	2007	2004	410.830329
2008	1999	470.139208	2007	2005	409.156245
2008	2000	472.948709	2007	2006	405.42009
2008	2001	475.769617	2007	2007	412.846397
2008	2002	479.77896	2007	2008	415.192357
2008	2003	484.525443	2007	2009	410.874605
2008	2004	485.896982	2007	2010	400.019064
2008	2005	487.17223	2007	2011	402.954391
2008	2006	488.631506	2007	2012	405.416653
2008	2007	491.7272	2007	2013	416.363574
2008	2008	483.755446	2007	2014	418.101774
2008	2009	490.203922	2008	1987	412.56082
2008	2010	474.093357	2008	1988	410.089316
2008	2011	478.501852	2008	1989	404.769159
2008	2012	472.055741	2008	1990	402.900239
2008	2013	491.953196	2008	1991	398.66317
2009	1987	478.978224	2008	1992	395.834474

2009	1988	473.511633	2008	1993	399.146511
2009	1989	465.460475	2008	1994	398.326382
2009	1990	463.550516	2008	1995	398.392415
2009	1991	456.733432	2008	1996	393.998695
2009	1992	450.812801	2008	1997	394.809525
2009	1993	456.830659	2008	1998	397.414509
2009	1994	458.784913	2008	1999	398.504271
2009	1995	461.879112	2008	2000	400.699883
2009	1996	460.209531	2008	2001	404.537382
2009	1997	464.247839	2008	2002	408.418465
2009	1998	469.272726	2008	2003	411.410786
2009	1999	470.84746	2008	2004	410.89938
2009	2000	473.695069	2008	2005	410.289056
2009	2001	476.518551	2008	2006	409.862379
2009	2002	480.311694	2008	2007	415.192357
2009	2003	484.600984	2008	2008	412.471511
2009	2004	485.95225	2008	2009	408.796131
2009	2005	487.188925	2008	2010	395.007266
2009	2006	488.489037	2008	2011	401.622342
2009	2007	490.580672	2008	2012	405.369853
2009	2008	490.203922	2008	2013	416.838772
2009	2009	483.485272	2008	2014	418.292433
2009	2010	458.87293	2009	1987	411.131786
2009	2011	475.851034	2009	1988	408.504026
2009	2012	470.45077	2009	1989	402.986703
2009	2013	492.052775	2009	1990	401.020317
2010	1987	474.618795	2009	1991	396.680931
2010	1988	468.53197	2009	1992	393.806123
2010	1989	459.746778	2009	1993	397.115552
2010	1990	457.434979	2009	1994	396.287723
2010	1991	449.993908	2009	1995	396.361167
2010	1992	443.529344	2009	1996	392.068315
2010	1993	449.558675	2009	1997	392.933606
2010	1994	451.357348	2009	1998	395.539998
2010	1995	454.362152	2009	1999	396.678172
2010	1996	452.374369	2009	2000	398.864616
2010	1997	456.370932	2009	2001	402.561186
2010	1998	461.416007	2009	2002	406.233769
2010	1999	462.815398	2009	2003	409.00389
2010	2000	465.548292	2009	2004	408.472062
2010	2001	468.238147	2009	2005	407.898664
2010	2002	471.963523	2009	2006	407.557139
2010	2003	476.296469	2009	2007	410.874605
2010	2004	477.256469	2009	2008	408.796131
2010	2005	477.912462	2009	2009	411.525966

2010	2006	478.321245	2009	2010	387.027658
2010	2007	479.166165	2009	2011	402.147458
2010	2008	474.093357	2009	2012	406.864206
2010	2009	458.87293	2009	2013	417.427156
2010	2010	480.710791	2009	2014	418.200608
2010	2011	486.491514	2010	1987	407.301075
2010	2012	477.61991	2010	1988	404.32815
2010	2013	489.763486	2010	1989	398.318264
2011	1987	472.95374	2010	1990	396.060093
2011	1988	466.92629	2010	1991	391.324387
2011	1989	458.285701	2010	1992	388.14098
2011	1990	456.119337	2010	1993	391.427271
2011	1991	448.965943	2010	1994	390.392784
2011	1992	442.872012	2010	1995	390.304412
2011	1993	448.963576	2010	1996	385.684369
2011	1994	450.941384	2010	1997	386.427607
2011	1995	454.071327	2010	1998	388.961683
2011	1996	452.472153	2010	1999	389.96768
2011	1997	456.538018	2010	2000	392.034497
2011	1998	461.534066	2010	2001	395.632375
2011	1999	463.132971	2010	2002	399.185894
2011	2000	465.941689	2010	2003	401.761088
2011	2001	468.684465	2010	2004	400.720834
2011	2002	472.287709	2010	2005	399.505553
2011	2003	476.315087	2010	2006	398.288945
2011	2004	477.437597	2010	2007	400.019064
2011	2005	478.345773	2010	2008	395.007266
2011	2006	479.137267	2010	2009	387.027658
2011	2007	480.350937	2010	2010	408.657495
2011	2008	478.501852	2010	2011	412.114257
2011	2009	475.851034	2010	2012	412.073289
2011	2010	486.491514	2010	2013	415.829029
2011	2011	479.136969	2010	2014	415.835576
2011	2012	474.809589	2011	1987	405.834375
2011	2013	487.052056	2011	1988	402.886278
2012	1987	466.484448	2011	1989	396.954566
2012	1988	460.237287	2011	1990	394.785261
2012	1989	451.368611	2011	1991	390.215529
2012	1990	449.140811	2011	1992	387.223608
2012	1991	441.893224	2011	1993	390.552184
2012	1992	435.787675	2011	1994	389.695798
2012	1993	441.980826	2011	1995	389.775479
2012	1994	444.034719	2011	1996	385.594373
2012	1995	447.240015	2011	1997	386.545144
2012	1996	445.749696	2011	1998	389.170666

2012	1997	449.879938	2011	1999	390.382324
2012	1998	454.900519	2011	2000	392.565255
2012	1999	456.570529	2011	2001	396.088791
2012	2000	459.410436	2011	2002	399.504895
2012	2001	462.1656	2011	2003	402.007312
2012	2002	465.716224	2011	2004	401.490148
2012	2003	469.629348	2011	2005	401.009885
2012	2004	470.741838	2011	2006	400.805453
2012	2005	471.637533	2011	2007	402.954391
2012	2006	472.408332	2011	2008	401.622342
2012	2007	473.521105	2011	2009	402.147458
2012	2008	472.055741	2011	2010	412.114257
2012	2009	470.45077	2011	2011	407.261573
2012	2010	477.61991	2011	2012	412.607145
2012	2011	474.809589	2011	2013	412.712352
2012	2012	473.451248	2011	2014	413.637642
2012	2013	466.608092	2012	1987	404.799991
2013	1987	479.024418	2012	1988	401.948691
2013	1988	474.162361	2012	1989	396.200044
2013	1989	467.134078	2012	1990	394.184631
2013	1990	465.980656	2012	1991	389.870425
2013	1991	460.633454	2012	1992	387.140568
2013	1992	456.417183	2012	1993	390.512068
2013	1993	462.450753	2012	1994	389.875078
2013	1994	464.979936	2012	1995	390.149133
2013	1995	468.353775	2012	1996	386.466647
2013	1996	468.074929	2012	1997	387.625865
2013	1997	472.039262	2012	1998	390.32324
2013	1998	476.471153	2012	1999	391.721162
2013	1999	478.412664	2012	2000	393.985863
2013	2000	481.056588	2012	2001	397.393606
2013	2001	483.506743	2012	2002	400.632562
2013	2002	486.218061	2012	2003	403.021163
2013	2003	488.772159	2012	2004	402.914326
2013	2004	489.77582	2012	2005	402.936542
2013	2005	490.597378	2012	2006	403.297486
2013	2006	491.270433	2012	2007	405.416653
2013	2007	491.834856	2012	2008	405.369853
2013	2008	491.953196	2012	2009	406.864206
2013	2009	492.052775	2012	2010	412.073289
2013	2010	489.763486	2012	2011	412.607145
2013	2011	487.052056	2012	2012	406.114781
2013	2012	466.608092	2012	2013	400.791144
2013	2013	482.855343	2012	2014	409.802916
			2013	1987	410.272536

2013	1988	407.987195
2013	1989	403.148216
2013	1990	401.723086
2013	1991	398.315736
2013	1992	396.379578
2013	1993	399.746722
2013	1994	399.65803
2013	1995	400.355544
2013	1996	397.85034
2013	1997	399.35023
2013	1998	402.036187
2013	1999	403.667953
2013	2000	405.906036
2013	2001	408.849375
2013	2002	411.48567
2013	2003	413.387588
2013	2004	413.788884
2013	2005	414.312392
2013	2006	415.037263
2013	2007	416.363574
2013	2008	416.838772
2013	2009	417.427156
2013	2010	415.829029
2013	2011	412.712352
2013	2012	400.791144
2013	2013	410.214909
2013	2014	417.160943
2014	1987	411.606424
2014	1988	409.54144
2014	1989	405.072405
2014	1990	403.887911
2014	1991	400.862417
2014	1992	399.260567
2014	1993	402.596822
2014	1994	402.72158
2014	1995	403.568485
2014	1996	401.550777
2014	1997	403.14039
2014	1998	405.740763
2014	1999	407.384053
2014	2000	409.499582
2014	2001	412.115406
2014	2002	414.360869
2014	2003	415.915539
2014	2004	416.326331

2014	2005	416.801174
2014	2006	417.359359
2014	2007	418.101774
2014	2008	418.292433
2014	2009	418.200608
2014	2010	415.835576
2014	2011	413.637642
2014	2012	409.802916
2014	2013	417.160943
2014	2014	411.052804
2015	1987	414.411554
2015	1988	412.691838
2015	1989	408.789422
2015	1990	407.944085
2015	1991	405.452444
2015	1992	404.29019
2015	1993	407.531665
2015	1994	407.901428
2015	1995	408.892774
2015	1996	407.457228
2015	1997	409.082486
2015	1998	411.483497
2015	1999	413.04389
2015	2000	414.898018
2015	2001	416.989596
2015	2002	418.625289
2015	2003	419.61636
2015	2004	419.892013
2015	2005	420.135618
2015	2006	420.297447
2015	2007	420.145841
2015	2008	419.76363
2015	2009	418.627538
2015	2010	414.622534
2015	2011	411.94408
2015	2012	408.60453
2015	2013	414.820101
2015	2014	414.142211

5.4. Pair statistics:

5.4.1. Path/row statistics:

Table 8: Final number of Landsat scenes utilised for each path/row combination and corresponding number of pairs created.

WRS2 Frame	Number of Scenes	Number of Pairs
008/011	26	46
009/011	179	330
010/011	141	249
011/011	104	161

5.4.2. Image utilisation per month:

Table 9: Number of Landsat scenes utilised overall, for each month.

Month	Number of scenes
January	0
February	0
March	0
April	70
May	86
June	63
July	60
August	75
September	67
October	29
November	0
December	0

5.5. Scripts:

5.5.1. Python scripts:

5.5.1.1. Transect plotter:

```
#!/usr/bin/env python
#coding=utf-8

"""
Plot CSV format velocity profiles using Matplotlib with Savitzky-
Golay filter.

Data in CSV file should be saved in format:
    Column 1: Distance from terminus (low to high), column header
name irrelevant
    Profile columns: Header in format STARTYEAR_ENDYEAR, e.g.
2015_2016
```

```
You should name .csv files with the desired title of the
corresponding plot.

Author : Hamish Morton
Date : 06/2018
"""

# Import libraries
import os, sys
import argparse
import numpy as np
import csv
import matplotlib.pyplot as plt
from matplotlib.pyplot import cm
from math import factorial
from scipy.signal import savgol_filter

# Setup arguments
parser = argparse.ArgumentParser(description="Plot .CSV format
velocity profiles using Matplotlib with Savitzky-Golay filter.")
parser.add_argument('CSV', type=str, help='str, path to folder
containing ".csv" files')
parser.add_argument('Window', type=int, help='int, size of moving
window for SG filter')
parser.add_argument('Poly', type=int, help='int, order of polynomial
for SG filter')
args = parser.parse_args()

# Append available CSV files to a list
CSVs = []
for file in os.listdir(args.CSV):
    if file.endswith('.csv'):
     CSVs.append(file)

# Initiate figure
fig = plt.figure()

# Open, filter and plot data from each CSV file
for vel_file in CSVs:
    data = np.genfromtxt(vel_file, delimiter=',', names=True)
    t_data = zip(*data)
    y = t_data[1:]

# Get header info for legend
    with open(vel_file) as f:
     readdata = csv.reader(f)
     vels = list(readdata)
    colhead = vels[0]

# Format the legend entries
    headers = []
    for i in colhead:
     head = i.replace('_', '-')
     headers.append(head)
```

```
    vel_headers = np.array(headers[1:])

# Apply SG filter to smooth profiles due to coarse pixel size and
potential noise
# Window size 21, polynomial 3 produces good results
    smooth_data = []
    for i in y:
     sg = savgol_filter(i, args.Window, args.Poly)
     smooth_data.append(sg)

# Set up subplot axis on which to plot profiles
    ax =
fig.add_subplot(int(1+(len(CSVs)/2)),2,CSVs.index(vel_file))

# Iterate through colours so that each profile is plotted as a
different colour along GnBu gradient
    color=iter(cm.GnBu(np.linspace(0,1,len(smooth_data))))

# Plot profiles in each csv file to subplot unique to each csv
    for i, label in zip(smooth_data, vel_headers):
     c=next(color)
     ax.plot(t_data[0], i, c=c, label=label, linewidth=3, alpha=1)
     ax.set_xlim((0) , max(t_data[0]))
     ax.set_ylim(0, np.nanmax(t_data[1:])+5)

# Format labels, titles, legend, etc...
    title = vel_file.replace('_', ' ')
    plt.title(title[:-4])
# if statement to ensure only one legend is plotted and only first
axis is labelled
    if vel_file == CSVs[0]:
     plt.ylabel('Velocity (m yr$^{-1}$)')
     plt.xlabel('Distance from transect origin (m)')
     leg = ax.legend(handlelength=0, handletextpad=0, frameon=True,
     bbox_to_anchor=(0.45, 0.3),
bbox_transform=plt.gcf().transFigure, ncol=3)
     leg.get_frame().set_facecolor('grey')
     for line,text in zip(leg.get_lines(), leg.get_texts()):
          text.set_color(line.get_color())
          line.set_visible(False)

plt.show()
```

5.5.1.2. Sensitivity analysis:

```
#!/usr/bin/env python
#coding=utf-8

"""
Description : Sensitivity analysis to estimate the effects of pair
temporal characteristics

Authors : Amaury Dehecq (section 1), Hamish Morton (all other
sections)
```

```
Date : July 2018
"""

# Import libraries
import numpy as np
import os, sys
import matplotlib.pyplot as plt
import pandas as pd
import SupportFunctions as sf

########################################################################
# Section 1 - Amaury Dehecq
# Read arguments
if len(sys.argv)!=2:
    Usage()
    sys.exit(1)
pairfile = sys.argv[1]

# Read pairlist information
pairs = sf.read_pairs(pairfile)
masters = [pair[0] for pair in pairs]
slaves = [pair[1] for pair in pairs]
images = np.unique(np.hstack((masters,slaves)))

########################################################################
# Section 2 - Hamish Morton
# Setup lists for appending data to
year = []
daystart = []
baseline = []
summer_perc = []
annual_vel = []

# Define start and end of summer
summer_start = 121
summer_end = 243

# Read pair information
for pair in pairs:
    master, slave = pair
    master_ID = os.path.basename(master)
    slave_ID = os.path.basename(slave)
    days = float(master_ID[13:16])
    daye = float(slave_ID[13:16])
    year1 = int(master_ID[9:13])

# Calculate number of days attributable to summer and winter motion
    end_stat = float(summer_end - days)
    start_stat = float(daye - summer_start)
    base = daye - days + 365
    comb_stat = ((end_stat + start_stat)/base)*100
    summer_days = end_stat + start_stat
    winter_days = base - summer_days
```

```
# Predict effects of temporal separation characteristics on ice
motion using data from Leverett glacier
    winter_vel = 81.6 * winter_days
    summer_vel = 127.6 * summer_days
    average_ann = (winter_vel + summer_vel)/base

# Append to lists for plotting
    annual_vel.append(average_ann)
    summer_perc.append(comb_stat)
    year.append(year1)
    baseline.append(base)
    daystart.append(days)

# Setup Pandas dataframes for plotting (must reset index to ensure
columns aligned)
# Average start day dataframe
sdoy_df = pd.DataFrame({'year':year,'daystart':daystart})
sdoy_gdf = sdoy_df.groupby('year').mean()
sdoy_fdf = sdoy_gdf.reset_index()

# Average baseline duration dataframe
df = pd.DataFrame({'year':year,'baseline':baseline})
basedf = df.groupby('year').mean()
finaldf = basedf.reset_index()

# % of baseline attributable to summer motion dataframe
summerdf = pd.DataFrame({'year':year,'summer_perc':summer_perc})
summer_groupdf = summerdf.groupby('year').mean()
final_summerdf = summer_groupdf.reset_index()

# Predicted velocity dataframe
veldf = pd.DataFrame({'year':year,'annual_vel':annual_vel})
vel_groupdf = veldf.groupby('year').mean()
final_veldf = vel_groupdf.reset_index()


# Setup subplots and axes
fig, axes = plt.subplots(nrows=4, ncols=1)
ax1 = axes[0]
ax2 = axes[1]
ax3 = axes[2]
ax4 = axes[3]

# Plot all dataframes with formatting
# Average start day plot
sdoy_fdf.plot(x='year',y='daystart',legend=False, ax=ax1,
color='black', marker='o', markersize=7, linewidth=2)
x_axis = ax1.axes.get_xaxis()
x_axis.set_visible(False)
y_axis = ax1.axes.get_yaxis()
y_axis.set_ticks_position('left')
ax1.set_ylabel('Average start DOY')

# Get y axis limits
sdoy_ymax = max(daystart)
```

```
sdoy_ymin = min(daystart)
ax1.set_ylim((sdoy_ymin, sdoy_ymax))

ax1.spines['right'].set_visible(False)
ax1.spines['top'].set_visible(False)
ax1.spines['bottom'].set_visible(False)

# Average temporal baseline plot
finaldf.plot(x='year',y='baseline',legend=False, ax=ax2,
color='black', marker='o', markersize=7, linewidth=2)
x_axis = ax2.axes.get_xaxis()
x_axis.set_visible(False)
y_axis = ax2.axes.get_yaxis()
y_axis.set_ticks_position('left')
ax2.set_ylabel('Average baseline duration (days)')

# Get y axis limits
base_ymax = max(baseline)
base_ymin = min(baseline)
ax2.set_ylim((base_ymin, base_ymax))

ax2.spines['right'].set_visible(False)
ax2.spines['top'].set_visible(False)
ax2.spines['bottom'].set_visible(False)

# % summer plot
final_summerdf.plot(x='year',y='summer_perc' ,legend=False, ax=ax3,
color='black', marker='o', markersize=7, linewidth=2)
ax3.set_ylabel('% Summer')

x_axis = ax3.axes.get_xaxis()
x_axis.set_visible(False)
y_axis = ax3.axes.get_yaxis()
y_axis.set_ticks_position('left')

# Get y axis limits
summer_ymax = max(summer_perc)
summer_ymin = min(summer_perc)
ax3.set_ylim((summer_ymin, summer_ymax))

ax3.spines['right'].set_visible(False)
ax3.spines['top'].set_visible(False)
ax3.spines['bottom'].set_visible(False)

# Predicted velocity plot
final_veldf.plot(x='year',y='annual_vel',legend=False, ax=ax4,
color='black', marker='o', markersize=7, linewidth=2)
ax4.set_xlabel('Year')
ax4.set_ylabel('Velocity (m yr$^{-1}$)')

x_axis = ax4.axes.get_xaxis()
x_axis.set_ticks_position('bottom')
y_axis = ax4.axes.get_yaxis()
y_axis.set_ticks_position('left')
```

```
# Get y axis limits
vel_ymax = max(annual_vel)-1
vel_ymin = min(annual_vel)+1
ax4.set_ylim((vel_ymin, vel_ymax))

ax4.spines['right'].set_visible(False)
ax4.spines['top'].set_visible(False)
plt.show()
```

5.5.2. R scripts:

5.5.2.1. Segmented linear regressions, runoff regressions and Mann-Whitney-Wilcoxon tests:

```
# Author: Hamish Morton
# Date: 17/05/2018
# Title: R Data Analysis

# Script to carry out stats tests (linear regressions, segmented
linear regressions and MWW tests) on velocity and runoff data

setwd('M:/dissi_UNIX/MISC')

#####################################################################
# Section 1 - Install and initialise required packages and read in
CSV files
install.packages(c("segmented", "zoo"))
library(segmented)
library(zoo)

medianVels <- read.csv('MEDVELS.csv', header = TRUE, sep = ",", dec
= ".")
MARdata <- read.csv('MAR.csv', header = TRUE, sep = ",", dec = ".")
RACMO2data <- read.csv('RACMO2.csv', header = TRUE, sep = ",", dec =
".")

colnames(medianVels)[1:2] <- c("Year", "MedVels")
colnames(MARdata)[1:9] <- c("Year", "MeanMelt", "MedMelt", "MedSMB",
"MeanSMB", "MedRun", "MeanRun", "MedELA", "MeanELA")
colnames(RACMO2data)[1:5] <- c("Year", "MedRun", "MeanRun",
"MedMelt", "MeanMelt")

#####################################################################
# Section 2 - Velocity regressions and MWW
# Linear regression, velocity with time
lin.mod1 <- lm(MedVels ~ Year, medianVels)
summary(lin.mod1)

# Carry out MWW tests to predict breakpoint for segmented linear
regression
for (i in 4:10){
  cat("Break date =", medianVels$Year[i])
  print(wilcox.test(medianVels$MedVels[1:i],
medianVels$MedVels[i+1:15], paired=FALSE))}
```

```
# Segmented linear regression with forced break dates 1998-2004
X=medianVels$Year
for (i in 1998:2009){
  cat("Year =", i)
  seg.mod1 <- segmented(lin.mod1, seg.Z = ~X, psi = list(X = c(i)),
control=seg.control(it.max = 0))
  print(summary(seg.mod1))}

#####################################################################
# Section 3 - Antecedent runoff regression with RACMO2 and MAR data,
including and excluding velocity year
# Rounds .5 dates down
integer.dates <- as.integer(X)

# Create dataframe with velocities and integer dates
int.df <- data.frame(integer.dates, medianVels$MedVels)
colnames(int.df)[1:2] <- c("Year", "MedVels")

# Function to carry out regressions
Runoff_func <- function(dataframe, velyear){
  if(velyear){
    for (i in 1:6){
      # Calculate antecedent runoff
      inc.df <- data.frame(dataframe$Year,
rollapplyr(dataframe$MeanRun, i, sum, fill = NA))
      colnames(inc.df)[1:2] <- c("Year", "RollSum")

      # Merge runoff and velocity dataframes
      velRun.df <- merge.data.frame(inc.df, int.df, by = "Year")

      # Apply a linear test
      linMean <- lm(MedVels ~ RollSum, velRun.df)

      # Report results
      cat("(Including vel year) Mean Test stat for:",
          i-1, "ant years", '\n')
      cat("R Squared:", summary(linMean)$r.squared, '\n')
      cat("P Value:", summary(linMean)$coefficients[8], '\n\n')}}

  else{
    for (i in 1:5){
      exc.df <-  data.frame(dataframe$Year,
rollapplyr(dataframe$MeanRun, list(-(i:1)), sum, fill=NA))
      colnames(exc.df)[1:2] <- c("Year", "RollSum")

      exvelyr_Run.df <- merge.data.frame(exc.df, int.df, by =
"Year")

      exvelyr_linMean <- lm(MedVels ~ RollSum, exvelyr_Run.df)

      cat("(Excluding vel year) Mean Test stat for:",
          i, "ant years", '\n')
      cat("R Squared:", summary(exvelyr_linMean)$r.squared, '\n')
```

```
      cat("P Value:", summary(exvelyr_linMean)$coefficients[8],
'\n\n')}}}

Runoff_func(RACMO2data, TRUE)
Runoff_func(RACMO2data, FALSE)
Runoff_func(MARdata, TRUE)
Runoff_func(MARdata, FALSE)

#####################################################################
# Section 4 - MWW tests/simple and segmented linear regressions for
runoff data
# MAR
Mar.df <- data.frame(MARdata$Year[7:36], MARdata$MedRun[7:36],
MARdata$MeanRun[7:36])
colnames(Mar.df)[1:3] <- c("Year", "RunoffMed", "RunoffMean")

# Linear regression
MARmod.Mean <- lm(RunoffMean ~ Year, Mar.df)
summary(MARmod.Mean)

# Segmented linear regressions with all available break dates
MARresults.df=NULL
MarYr=Mar.df$Year
for (i in 1986:2014){
  for (j in 1987:2013){
    seg.MarMean <- segmented(MARmod.Mean, seg.Z = ~MarYr, psi =
list(MarYr = c(i,j)), control=seg.control(it.max = 0))
    RSE <- sqrt(deviance(seg.MarMean)/df.residual(seg.MarMean))
    MARresults.df = rbind(MARresults.df, data.frame(i, j, RSE))}}
bestMAR <- which.min(apply(MARresults.df,MARGIN=1,min))
varMAR <- data.frame(MARresults.df[bestMAR,])
seg.MarMean <- segmented(MARmod.Mean, seg.Z = ~MarYr, psi =
list(MarYr = c(varMAR[1],varMAR[2])), control=seg.control(it.max =
0))
varMAR
summary(seg.MarMean)

# MWW test on samples from regression
# 1985:1992 with 1993:2012, insufficient sample sizes for the rest
wilcox.test(Mar.df$RunoffMean[1:8], Mar.df$RunoffMean[9:28],
paired=FALSE)

# Mean runoff from each period
mean(Mar.df$RunoffMean[1:8])
mean(Mar.df$RunoffMean[9:28])
mean(Mar.df$RunoffMean[29:30])


# RACMO
RACMO.df <- data.frame(RACMO2data$Year[6:37],
RACMO2data$MedRun[6:37], RACMO2data$MeanRun[6:37])
colnames(RACMO.df)[1:3] <- c("Year", "RunoffMed", "RunoffMean")

# Linear regression
RACMOmod.Mean <- lm(RunoffMean ~ Year, RACMO.df)
```

```
summary(RACMOmod.Mean)

# Segmented linear regressions with all available break dates
RACMOresults.df=NULL
RACMOYr=RACMO.df$Year
for (i in 1986:2015){
  for (j in 1987:2014){
    seg.RACMOMean <- segmented(RACMOmod.Mean, seg.Z = ~RACMOYr, psi
= list(RACMOYr = c(i, j)), control=seg.control(it.max = 0))
    RSE <- sqrt(deviance(seg.RACMOMean)/df.residual(seg.RACMOMean))
    RACMOresults.df = rbind(RACMOresults.df, data.frame(i, j,
RSE))}}

bestRACMO <- which.min(apply(RACMOresults.df,MARGIN=1,min))
varRACMO <- data.frame(RACMOresults.df[bestRACMO,])
seg.RACMOMean <- segmented(RACMOmod.Mean, seg.Z = ~RACMOYr, psi =
list(RACMOYr = c(varRACMO[1], varRACMO[2])),
control=seg.control(it.max = 0))
varRACMO
summary(seg.RACMOMean)

# MWW test on samples from regression
# 1985:1997 with 1998:2012, rest are insignificant likely due to
population sample sizes
wilcox.test(RACMO.df$RunoffMean[1:13], RACMO.df$RunoffMean[14:28],
paired=FALSE)

# Mean runoff from each period
mean(RACMO.df$RunoffMean[1:12])
mean(RACMO.df$RunoffMean[13:27])
mean(RACMO.df$RunoffMean[18:32])
```

5.5.2.2. Analysis of covariance tests:

```
# Author: Hamish Morton
# Date: 05/07/2018
# Title: R ANCOVA

# Script to carry out ANCOVA test on ice surface and ice thickness
profiles

setwd('M:/dissi_UNIX/Elev/New_csvs/')

# ANCOVA for slope
# Read in data
slopes <- read.csv('Surface_profilesR.csv', header = TRUE, sep =
",", dec = ".")
colnames(slopes)[1:3] <- c("Distance", "Source", "Elev")

# Script to calculate statistical difference in regression slope
mod.slope <- aov(Elev~Distance*Source, data = slopes)
summary(mod.slope)
```

```
# ANCOVA for ice thickness
# Read in data
thickness2 <- read.csv('Thickness_profilesR.csv', header = TRUE, sep
= ",", dec = ".")
colnames(thickness2)[1:3] <- c("Distance", "Source", "Thickness")

# Script to calculate statistical difference in regression slope
mod.thickness <- aov(Thickness~Distance*Source, data = thickness2)
summary(mod.thickness)

# Script to calculate statistical difference in intercept
mod.thickness2 <- aov(Thickness~Distance+Source, data = thickness2)
summary(mod.thickness2)
```

5.6. Data index:

Table 10: Data index showing locations of digital data used in this study. Each folder contains 'README.txt' with information on files. For further information on how to use these data, visit: https://www.geos.ed.ac.uk/~ngourme2/geos_EO_howTo/Edi_cryo_rs_docs.html#_optical_offset_tracking_amaury_josh_stijn

Data	Format	Purpose	Location	Date of most recent update
Landsat scenes	.TIF	Used for feature tracking	/exports/csce/datastore/groups/geos_EO/L0data/Landsat/	N/A
Final merged annual velocity maps and error maps	.TIF	Used to derive final time series median velocities and error bars (includes pair info files)	/home/s1791566/dissfinal/GeoTIFFs/Vel_time_series/Final/	28/06/2018
Initial merged annual velocity maps and error maps	.TIF	Used to derive initial erroneous time series median velocities and error bars (includes pair info files)	/home/s1791566/dissfinal/GeoTIFFs/Vel_time_series/Initial/	03/08/2018
Final merged annual velocity maps and error maps (for MeASUREs comparison)	.TIF	Final merges in polar stereographic projection for comparison with MeASUREs data	/home/s1791566/dissfinal/GeoTIFFs/Vel_time_series/Polar_stereo/	25/07/2018
Final baseline	.TIF	Used to understand	/home/s1791566/dissfin	24/07/2018

difference maps		spatial pattern of velocity change (under final parameter choices)	al/GeoTIFFs /Baseline_diff/Final_params/	
Initial baseline difference maps	.TIF	Used to understand spatial pattern of velocity change (under initial parameter choices)	/home/s1791566/dissfinal/GeoTIFFs/Baseline_diff/Initial_params/	25/06/2018
Performance indicators	.TIF	Used to illustrate the quality of feature tracking results. Includes 'Coherence', 'Median Absolute Deviation' and 'Number of Points' maps/	/home/s1791566/dissfinal/GeoTIFFs/Performance_indicators/	02/07/2018
Ice mask, clipped to study region	.TIF	Used to locate on ice areas for calculation of median velocities	/home/s1791566/dissfinal/GeoTIFFs/Study_area_masks/gimp_mask.TIF	24/05/2018
GIMP DEM, clipped to study region	.TIF	Used to calculate common points at altitudinal intervals	/home/s1791566/dissfinal/GeoTIFFs/Study_area_masks/dem_mask.TIF	24/05/2018
Surface elevation, ice thickness and bed data	.TIF	Used to derive ice sheet surface elevation and thickness profiles for ANCOVA tests	/home/s1791566/dissfinal/GeoTIFFs/Geom_data/	04/07/2018
Coregistration accuracy difference data (under final parameters)	.TIF	Final outputs showing difference in coregistration accuracy of different time periods under final parameter choices	/home/s1791566/dissfinal/GeoTIFFs/Coreg_data/Final_params_diff/	24/07/2018
Coregistration accuracy difference data (under initial parameters)	.TIF	Initial outputs showing difference in coregistration accuracy of different time periods under	/home/s1791566/dissfinal/GeoTIFFs/Coreg_data/Initial_params_diff/	07/06/2018

		incorrect parameter choices		
Merges for coregistration accuracy maps (under final parameters)	.TIF	Merges used to calculate difference in coregistration accuracy of different time periods (under final parameters)	/home/s1791566/dissfinal/GeoTIFFs/Coreg_data/Final_merges/	28/06/2018
Merges for coregistration accuracy maps (under initial parameters)	.TIF	Merges used to calculate difference in coregistration accuracy of different time periods (under initial parameters)	/home/s1791566/dissfinal/GeoTIFFs/Coreg_data/Initial_merges/	24/06/2018
Study site mask	.TIF	Mask version of study site shapefile. Used in MATLAB scripts to mark study site	/home/s1791566/dissfinal/GeoTIFFs/Study_area_masks/triangle2.TIF	26/05/2018
X and Y velocity components	.TIF	Directional flow components used to create vector field to delineate study site	/home/s1791566/dissfinal/GeoTIFFs/Flow_direction/	26/05/2018
Tier 2 image generated velocity map		Velocity map generated using tier 2 Landsat imagery to show effects	/home/s1791566/dissfinal/GeoTIFFs/Tier2/merge_lc8_1617_snr7_lon50.vel.TIF	02/08/2018
IMBIE basins	.tif	Basins from which runoff data were extracted	/home/s1791566/dissfinal/IMBIE/71_72_imbiemerge.tif	03/05/2018
MeASUREs velocity data	.tif	MeASUREs velocity data used to ratify findings of this study	/exports/csce/datastore/groups/geos_EO/L0data/Measures/Measures_Annual_Velocity_Mosaics_V2/*	04/07/2018
Original ice mask	.tif	Clipped to locate areas for median coregistration, estimation of	/exports/csce/datastore/groups/geos_EO/DEMS/	06/11/2015

		uncertainty and extraction of on-ice velocities	GIMP/GimpIceMask_90m.tif	
Runoff data	.nc	Initial runoff data files	/home/s1791566/dissfinal/Runoff/	03/05/2018
Velocity transect shapefiles	.SHP	Shapefiles along which velocity transects were extracted. Includes initial polylines as well as final point shapefiles	/home/s1791566/dissfinal/shapefiles/Velocity_transects/	04/07/2018
Geometry transect shapefiles		Shapefiles along which geometry transects were extracted. Includes initial polylines as well as final point shapefiles	/home/s1791566/dissfinal/shapefiles/Geometry_transects/	04/07/2018
Study area shapefile	.SHP	Shapefile of study area, derived using flow direction map	/home/s1791566/dissfinal/shapefiles/Study_site/Triangle_w_peri.shp	04/07/2018
Path/row locator shapefile	.SHP	Shapefile used to find path/row combinations intersecting the study area	/home/s1791566/dissfinal/shapefiles/WRS2_site/Study_area_poly.shp	20/01/2018
Median annual velocities and associated error	.CSV	Outputs from MATLAB script of velocity and error time series data, for use in R	/home/s1791566/dissfinal/CSVs/Vel_time_series/	30/06/2018
Runoff data	.CSV	Outputs from MATLAB script of runoff time series data, for use in R	/home/s1791566/dissfinal/CSVs/Runoff/	17/05/2018
Surface elevation/ice thickness profiles	.CSV	Outputs from geometry transect shapefile attribute tables, for plotting in Python and analysis in R	/home/s1791566/dissfinal/CSVs/Geom_transects/	05/07/2018
Velocity transects (initial and	.CSV	Outputs from velocity transect shapefile	/home/s1791566/dissfinal/CSVs/Vel	06/07/2018

final parameters)		attribute tables, for plotting in Python	_transects/ *_params/	
Python scripts (author – Hamish Morton)	.py	Shown in appendix. Used to plot transects and for sensitivity analysis	/home/s1791566/dissfinal/Python_scripts/	29/07/2018
Python Scripts (all other authors)	.py	Python scripts used as part of automated feature tracking process	/exports/csce/datastore/groups/geos_EO/development/s1791566/Cryosphere/opticProc/	26/06/2018
R scripts	.R	Shown in appendix. Used to carry out statistical analysis	/home/s1791566/dissfinal/R_scripts/	29/07/2018
MATLAB scripts	.m	Used to create velocity/runoff time series figures and WRS2 map	/home/s1791566/dissfinal/MATLAB_scripts/	25/07/2018
Pair list of all utilised pairs	.txt	Pair list of all image pairs used in this study	/home/s1791566/dissfinal/txt/pairlist/pairlistPCA.txt	19/07/2018
WRS2 coordinate file	.txt	File containing WRS2 coordinates of scenes covering the study region	/home/s1791566/dissfinal/txt/wrs2/_wr2coords.txt	20/01/2018
Template files	.template	Used to define parameters for feature tracking, pre- and post-processing	/home/s1791566/dissfinal/txt/templates/	22/07/2018